



# UNIVERSITA' DEGLI STUDI DI PADOVA

## TESI DI DOTTORATO

Sede Amministrativa: Università degli Studi di Padova

Sede Consorziate:

Dipartimento di      Astronomia

---

SCUOLA DI DOTTORATO DI RICERCA IN :    Astronomia

INDIRIZZO:

CICLO            XXI

### **PHYSICS OF THE BROAD EMISSION LINE REGIONS IN ACTIVE GALACTIC NUCLEI AND THE SPECTRAL PROPERTIES OF THE BALMER SERIES**

**Direttore della Scuola :** Ch.mo Prof. Giampaolo Piotto

**Supervisore :** Ch.mo Prof. Piero Rafanelli

**Dottorando :** Giovanni La Mura



# Acknowledgements

This work summarizes the results achieved in three years of study at the PhD. Research School of Astronomy in Padua, but, above all, it represents a fundamental score after more than ten years of personal interest in Astrophysics. I certainly owe a huge thank to every people who, during these years, provided their help, support, suggestions, and encouragement, giving me the chance to explore the world of Astronomy.

At first, I shall mention my parents and my family, who raised my interest towards the scientific approach to nature and sky, eventually supporting my wish to pursue these topics in the course of my studies. Then I thank Prof. P. Rafanelli, for his supervision in the development of this work, Dr. S. Ciroi and Dr. F. Di Mille, for the fundamental discussions, which originated most of the solutions, that I adopted for the problems I dealt with in this work, and Prof. W. Kollatschny, for review and comments. I thank Prof. L. Č. Popović and Dr. D. Ilić, for their precious collaboration and their friendly hospitality, during my first experiences abroad. I should also remember, here, that this work has only been possible thanks to the commitment of many other people, the Sloan Digital Sky Survey team, above all, many of whom I will hardly be able to know, but I think they should be properly acknowledged here. A special thanks goes to Dr. C.-W. Yip, who provided help in my access to the data I needed to develop my own procedures.

Finally, there are several people, whom I met both in my Department, as well as outside the University, that largely helped me every time I needed. Let me remember: P. T., who introduced me to the study of Astronomy; F. C., always a good host, when I felt the distance to my homeland; A. C., the best laboratory partner I could ever ask for; P. T. (yes, the characters are the same, but the person is different), THE colleague; M. P., G. G., L. P., and L. P., who kept my personal interests alive, when I used to spend most of my time at work; F. “S.” M. and N. “T.” ?, since they are simply themselves. At last, I particularly thank Pino, for putting me on saddle again, after six years, and, of course, for training Top Gun. Because. . .

*sometimes, I like to forget all the other things  
and to realize, for a while, that horses have wings!*

# Abstract

The spectrum of the electromagnetic radiation coming from Active Galactic Nuclei (AGN) is often characterized by the presence of a continuous emission, covering a wide range of frequencies, which spans from the X and  $\gamma$  rays down to the radio waves, as well as by the existence of a large number of emission lines. The properties of these lines suggest an origin connected with the recombination processes, which follow the gas photo-ionization due to the most energetic fraction of the continuum irradiated by the source. Moreover, looking at the recombination line profiles, it is possible to distinguish among broad emission lines, exclusively associated to permitted atomic transitions, and narrow emission lines, which, instead, are commonly identified from forbidden transitions, as well.

The distinction between profiles, based on the transition probabilities of the corresponding lines, tells us that the two types of emission have a different origin. In particular, the broad lines come from a region filled by a high particle density plasma, that lies extremely close to the central source of ionizing radiation, the *Broad Line Region* (BLR). Because of its limited extent and of the density of its material, the properties of the BLR are not directly observable, neither they can be appropriately handled by means of the spectroscopic techniques that are exploited in other conditions, where a balance among photo-ionization and recombination processes is carried out.

The aim of this PhD. thesis is to study the kinematical and the thermodynamical properties of the gas, within the BLR, developing an analysis of the spectral lines emitted by hydrogen in the Balmer series. After discussing some fundamental features, which allow us an interpretation of the AGN nature, we describe the relationship among the thermodynamical conditions of the BLR plasma and the processes which take place in the central source. Our investigation exploits the application of *Boltzmann Plots* and that of a technique, based on line profile cross-correlation, on two object samples, collected at the *Sloan Digital Sky Survey* (SDSS) database, to gather information from all the observed lines. The results obtained in this way improve our understanding of the BLR structure, as well as of the influence played by the central source in controlling the physical conditions of the gas located therein.

# Estratto

Lo spettro della radiazione elettromagnetica dei Nuclei Galattici Attivi (AGN) viene spesso contraddistinto dalla presenza di un continuo di emissione, esteso su di un vasto intervallo di frequenze, che vanno dai raggi X e  $\gamma$  fino alle onde radio, come pure da quella di un gran numero di righe di emissione. Le proprietà di queste righe suggeriscono un'origine legata ai processi di ricombinazione, che seguono alla foto-ionizzazione del gas da parte della porzione più energetica del continuo irradiato dalla sorgente. Osservando i profili delle righe di ricombinazione, inoltre, è possibile operare una distinzione tra righe di emissione larghe, esclusivamente associate a transizioni atomiche permesse, e righe di emissione strette, che, invece, vengono comunemente identificate anche in corrispondenza di transizioni proibite.

La suddivisione dei profili, in base alla probabilità di transizione delle righe corrispondenti, indica che i due tipi di emissione hanno una diversa origine. In particolare, le righe larghe provengono da una regione occupata da un plasma ad alta densità particellare, che si trova nelle immediate vicinanze della sorgente centrale di radiazione ionizzante, la *Broad Line Region* (BLR). A causa della sua limitata estensione e della densità del materiale che la costituisce, le proprietà della BLR non sono direttamente osservabili, né possono essere gestite adeguatamente per mezzo dei metodi spettroscopici che vengono impiegati in altre situazioni, ove sussiste un bilancio tra processi di foto-ionizzazione e ricombinazione.

Lo scopo di questa tesi di dottorato è quello di studiare le proprietà cinematiche e termodinamiche del gas, all'interno della BLR, sviluppando un'analisi delle righe spettrali emesse dall'idrogeno nella serie di Balmer. Dopo aver discusso alcune fondamentali caratteristiche, che permettono di interpretare la natura degli AGN, descriviamo la relazione tra lo stato termodinamico del plasma nella BLR ed i fenomeni che avvengono nella sorgente centrale. La nostra indagine sfrutta l'applicazione dei *Diagrammi di Boltzmann* e di una tecnica basata sulla cross-correlazione dei profili su due campioni di oggetti, selezionati presso l'archivio della *Sloan Digital Sky Survey* (SDSS), per estrarre informazioni da tutte le righe osservate. I risultati così ottenuti migliorano la nostra comprensione della struttura della BLR, nonché dell'influenza giocata dalla sorgente centrale nel determinare lo stato fisico del gas al suo interno.



# Contents

<b>1</b>	<b>Introduction to Active Galactic Nuclei</b>	<b>11</b>
1.1	The concept of Active Galactic Nucleus . . . . .	11
1.2	AGN Classification . . . . .	12
1.3	AGN Spectral Properties . . . . .	15
1.3.1	Spectral Energy Distribution . . . . .	15
1.3.2	Emission Lines . . . . .	19
1.3.3	AGN variability properties . . . . .	22
1.4	The Super Massive Black Hole Model . . . . .	24
1.5	Unification Theories for AGN . . . . .	28
<b>2</b>	<b>Astrophysical Plasma Spectroscopy</b>	<b>35</b>
2.1	Introduction . . . . .	35
2.2	Thermodynamical Equilibrium in Plasmas . . . . .	36
2.3	Radiation Transfer . . . . .	37
2.4	Photo-Ionization Equilibrium . . . . .	41
2.4.1	Photo-Ionization of a Pure Hydrogen Plasma . . . . .	41
2.4.2	Photo-Ionization of Chemically Complex Gas . . . . .	46
2.5	Thermal Equilibrium . . . . .	47
2.5.1	Photo-ionization and Recombination . . . . .	48
2.5.2	Thermal Bremsstrahlung . . . . .	49
2.5.3	Cooling by Collisionally Excited Radiation Emission . . . . .	50
2.6	Physical Properties from Emission Lines . . . . .	53

<b>3</b>	<b>Physical Processes in the BLR</b>	<b>57</b>
3.1	Introduction . . . . .	57
3.2	The Standard Cloud Model . . . . .	58
3.2.1	Cloud Stability . . . . .	59
3.2.2	The BLR Structure with Clouds . . . . .	63
3.3	BLR Kinematics from the Emission Line Profiles . . . . .	65
3.4	Dust Obscuration and Reddening . . . . .	70
3.5	BLR Observational Properties . . . . .	73
3.5.1	Theory and Observations . . . . .	73
3.5.2	Correlations among the Emission Lines . . . . .	75
3.5.3	Correlations among Lines and Continuum . . . . .	77
3.6	Probing the BLR . . . . .	79
<b>4</b>	<b>Sample Collection and Data Reduction</b>	<b>81</b>
4.1	Introduction . . . . .	81
4.2	The SDSS Program . . . . .	82
4.2.1	Telescope and Instrumentation . . . . .	82
4.2.2	Spectroscopic Data Products . . . . .	84
4.2.3	The SDSS Online Data Archive . . . . .	86
4.3	Sample Collection . . . . .	87
4.4	Preliminary Spectral Reduction . . . . .	89
4.4.1	Host galaxy correction . . . . .	90
4.4.2	Identification of the BLR Spectral Component . . . . .	93
4.5	Programming Language Implementation . . . . .	96
4.5.1	Dynamic Memory Access . . . . .	97
4.5.2	Data Format Control . . . . .	98
4.5.3	Object Oriented Programming . . . . .	99
<b>5</b>	<b>Thermodynamical Properties of the BLR</b>	<b>107</b>
5.1	Introduction . . . . .	107
5.2	Boltzmann Plots for Plasma Diagnostics . . . . .	108
5.3	Spectral Analysis . . . . .	111

5.4	Results . . . . .	113
5.4.1	The Continuum Source and Emission Line Properties . . . . .	117
5.4.2	Global Baldwin Effect . . . . .	120
5.4.3	Line Profiles and Boltzmann Plots . . . . .	122
5.4.4	Line Profiles and AGN Accretion Rates . . . . .	125
5.5	Discussion . . . . .	127
<b>6</b>	<b>BLR Gas Kinematics</b>	<b>139</b>
6.1	Introduction . . . . .	139
6.2	Theoretical Line Profiles . . . . .	140
6.2.1	Emission Line Broadening from Cross-Correlation . . . . .	141
6.2.2	Analytical expressions for the broadening functions . . . . .	143
6.3	Spectral Analysis . . . . .	144
6.3.1	The Balmer Line Broadening Functions . . . . .	144
6.3.2	Emission Line Widths and Continuum Luminosity . . . . .	147
6.4	The BLR Structural Models . . . . .	148
6.4.1	Inclination and line profile broadening . . . . .	149
6.4.2	Mass and accretion rate estimates . . . . .	153
6.5	Discussion . . . . .	156
<b>7</b>	<b>Conclusions</b>	<b>167</b>



# Chapter 1

## Introduction to Active Galactic Nuclei

### 1.1 The concept of Active Galactic Nucleus

In the course of centuries, the human kind gradually realized that a huge world, hosting a large variety of fascinating mysteries, surrounds its life. The development of science and technology, in our effort to understand the Universe, brought several answers to our minds, together with more and more challenging questions. Of course, the sky and its nature soon raised our interest, as an apparently endless source of knowledge and wonder. While systematic studies of celestial bodies have their roots deep in the past of ancient civilizations, the birth of Astrophysics is commonly identified with Galilei's first attempt to build and exploit a scientific instrument to investigate their nature: the telescope.

Since then, we realized that most of the light collected by our eyes in the world comes from stars, with the fundamental contribution of our Sun and the sparkling beauty of the night sky. Our modern telescopes revealed that stars are the most common sources of optical light, from the Milky Way to the faraway galaxies. They burn chemical elements in a fairly well understood sequence of thermo-nuclear reactions, driven by the balance of gravity and

pressure gradients in their cores. However, they are neither the only, nor the most powerful sources of energy.

Today we know that the optical light is only the fraction caught by human eyes of the spectrum of electro-magnetic radiations, in which some of the energy produced by astrophysical sources travels across the Universe. In order to look at the properties of other regions in the electro-magnetic spectrum, we need more instruments, which are able to deal with the various energies characterizing the radiation. By means of such instruments, we find that the same landscape in the sky may look very different, according to the energy of the signal we are seeking for. Actually, while stars appear to dominate the light emission in near ultraviolet and optical radiation, their contribution to other spectral ranges, such as X-rays or radio, quickly drops towards a negligible amount. Here, our observations of the sky led to the identification of some extremely compact radiation sources, having, in some cases, similar properties to those recorded in the central regions of particular galaxies, that show an exceptionally bright core. Comparing the energetic output of these objects with the available constraints about their dimensions, it is clear that their energy production efficiency is much larger than the yield of the thermo-nuclear reactions, which are characteristic of stellar activity. The increasing evidence that most of these point-like objects can be associated with the central regions of extended galaxies led to the definition of Active Galactic Nuclei, commonly shortened into AGN.

## **1.2 AGN Classification**

There are several properties that may be used to distinguish among different classes of AGN, according to some specific classification schemes. However, at present, we believe that many of the observational differences are induced by our line of sight towards the object, although some details do not fit in this simple interpretation. For this reason, many of the distinctions still applied have more an historical rather than a physical meaning and provide

a quick summary of the main features characterizing the nuclear activity. Chronologically speaking, the first objects, that were actually identified as special galactic nuclei, were Seyfert galaxies (see Fath 1908, Slipher 1917, and Seyfert 1943). Whereas a class of strong, compact radio sources, associated with star-like objects and, henceforth, dubbed *quasi stellar radio sources* or *quasars*, was also introduced, its explanation in terms of exceptionally bright cores of distant galaxies was not yet known. Although these objects shared many features, which supported the idea of a common nature, a few important arguments, concerning observational differences in variability, luminosity and spectral line strengths, had to be solved (see Burbidge & Burbidge 1967). Only more recently it was realized that much of the observational gap could be explained in terms of the selection criteria in the first AGN surveys, which enhanced the collection of extreme and opposite cases. More advanced tests show that the original distinction of quasars from Seyferts reflects a magnitude scale in activity. Moreover, the concept of quasar lost a large fraction of its original meaning when broad band photometric observations, carried out by Sandage (1965) and Lynds et al. (1965), demonstrated the existence of several sources, in the range of 10 up to 20 times the known number of radio objects, sharing the same properties, but without a detectable radio emission.

At present, when an AGN cannot be associated with a resolved host, it is usually referred to as a *Quasi Stellar Object* (QSO). If, on the contrary, the host is detected, the object may enter one of the following general classes:

**Seyfert Galaxy**, a galaxy featuring a bright unresolved radiation source in its core, whose spectrum is characterized by the presence of several emission lines;

**Blazar**, a class of objects with an extended spectral energy distribution, striking time variability properties, and a significant degree of polarization in the radiation;

**Radio Galaxy**, a galaxy surrounded by an extended source of radio emis-

sion, which is interpreted as the final result of energetic processes ejecting matter from the nucleus.

These classes are further subdivided into other families, according to the observed spectral properties. When some of the emission lines in the spectrum of an AGN have a broad profile, the object is classified as a Type 1 source, otherwise it belongs to Type 2. Looking at Seyfert galaxies, Osterbrock (1981) introduced a notation for intermediate cases, based on the relative strength of the broad emission line component with respect to the total flux, naming Seyfert 1.9 galaxies the objects where the broad emission can be detected only in the  $H\alpha$  emission line, Seyfert 1.8 those where a weak broad component is found also in  $H\beta$ , and Seyfert 1.5 those objects where the strengths of the broad and narrow components is comparable. Again the prominence of the emission lines tracks the distinction of blazars in Optically Violent Variables (OVV), with prominent lines, and BL Lacertae objects, having weak or absent lines. On the other hand, the power of radio emission, with respect to the global amount of energy irradiated by the source, is used to distinguish among *radio loud* and *radio quiet* objects, for example by introducing a specific flux ratio at radio and optical frequencies and choosing a radio loudness threshold, such as, for instance, in Kellerman et al. (1989).

A lot of other classes have been drawn, such as the Low Ionization Nuclear Emission Regions (LINER), actually considered half the way between a true active galaxy and a star forming one, or the Broad and Narrow Line Radio Galaxies (BLRG and NLRG), essentially the radio loud counterparts of Seyfert 1 and 2 classes, but they are often mentioned only to stress some specific observational property and they are not considered in many of the commonly adopted AGN classification schemes.

## 1.3 AGN Spectral Properties

It has often been noted that, in the case of AGN, spectroscopic observations are much more useful than direct imaging. The resolution of our instruments, up to now, only allowed to place severe constraints about the size of the central energy source, but very little has been understood concerning its actual structure.

A thorough analysis of AGN spectra, instead, reveals much more details about the processes that cannot yet be directly detected. AGN spectra have several properties, such as broad band continuum radiation and line emission, whose characteristics depend on the physical processes that provide the large power of their radiation. These features are often found to be variable in time and there is strong evidence for interaction among them. The time scales corresponding to variations and interactions can be measured and, in the assumption of a logical relationship of cause and effect, where a signal cannot travel faster than the speed of light  $c$ , they provide an upper limit to the size of the object. Moreover, the global variability behaviour depends on the structure which is responsible of radiation emission, thus it is a strong constraint on the physics which explains the nature of AGN.

### 1.3.1 Spectral Energy Distribution

One of the most striking features of AGN is the peculiar Spectral Energy Distribution (SED) of their light. In spite of their quasi stellar appearance, AGN irradiate their energy over a much broader frequency range than stars do. As it is shown in Fig. 1.1, the spectrum of a star can be reproduced with reasonable approximation by the Planck's law of the black body thermal emission corresponding to an effective temperature  $T_{eff}$ :

$$B_{\nu}(T_{eff}) = \frac{2h\nu^3}{c^2} \frac{1}{e^{h\nu/k_B T_{eff}} - 1}, \quad (1.1)$$

where we denote with  $\nu$  the emission frequency and with  $h$ ,  $k_B$ , and  $c$  the fundamental constants of Planck, Boltzmann, and the speed of light, respec-

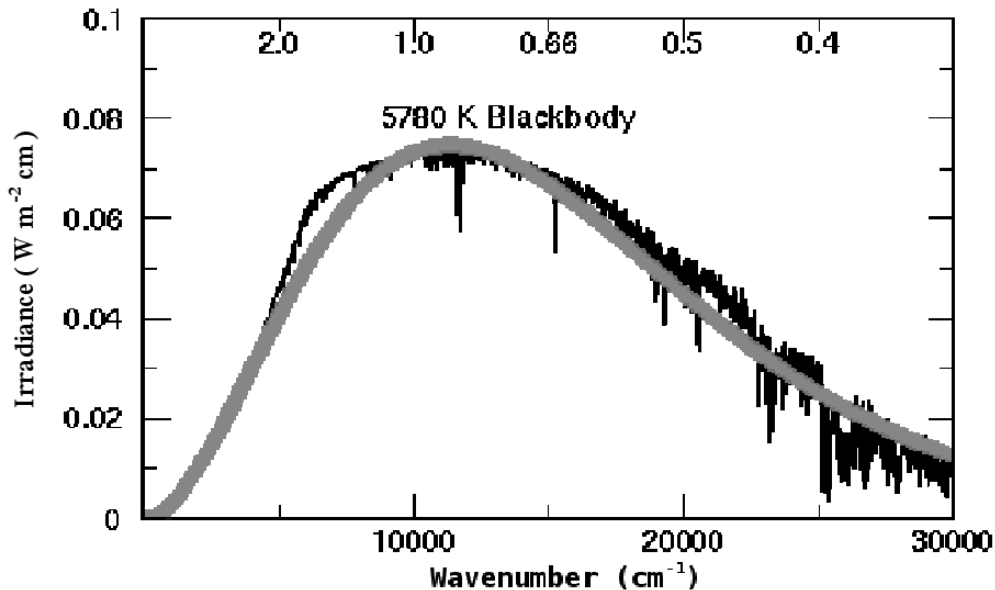


Figure 1.1: The spectrum of our Sun, here shown as a thin black line, like that of many other stars, follows with quite good approximation the thermal emission of a black body of appropriate temperature (thick gray line).

tively. Early investigations on the typical SED of AGN, instead, revealed a power-law spectrum, in the form of  $F_\nu \propto \nu^{-\alpha}$ , with  $F_\nu$  being the specific flux and  $\alpha$  the spectral index, typically in the range from 0.5 and 1, which raised problematic issues concerning its origin.

A common interpretation for the power-law continua of AGN spectra assumed that photons were irradiated as the synchrotron emission of a relativistic electron plasma, in the magnetic field of the source, and then inverse-Compton scattered, by the same electrons, toward high energies, in the so called Synchrotron Self-Compton (SSC) mechanism. On the basis of this model, it was suggested that AGN continuum has a non-thermal origin, in the sense that the emitting particles do not attain a Maxwell-Boltzmann velocity distribution driven by collisions. The predictions of the SSC scenario, however, do not achieve complete agreement with observations, since the high degree of expected polarization is generally found only in blazars.

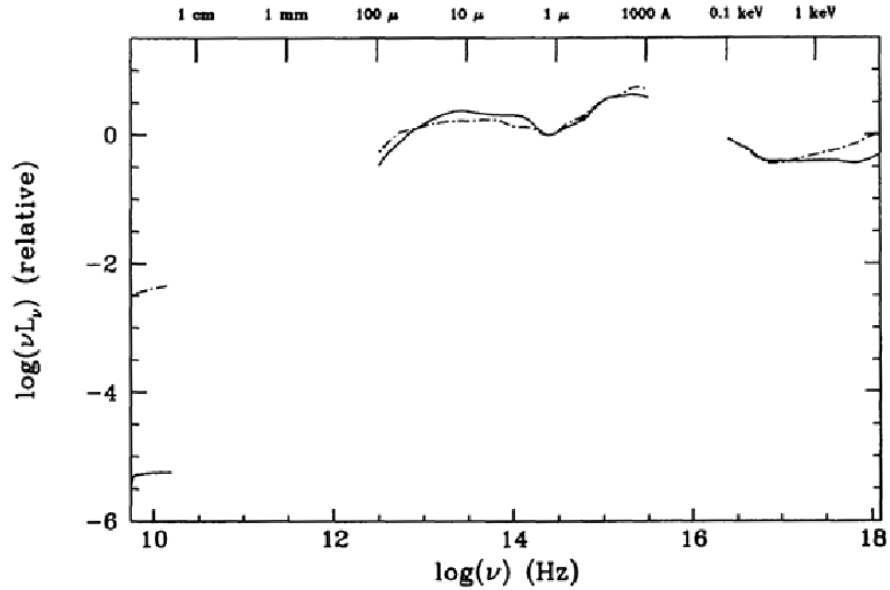


Figure 1.2: Average continuum Spectral Energy Distributions (SED) for radio quiet (thin continuous line) and radio loud (dashed line) QSO. The spectra, which have been normalized to the commonly observed minimum at  $\lambda = 1 \mu\text{m}$ , show multiple components, probably originated by different processes. From Elvis et al. (1994).

It became quickly clear that a single process might never be able to explain the complex nature of AGN spectra and that even a single power-law fit to the continuum was an over-simplification. Studying the typical shape of AGN spectra, in the available frequency ranges, Elvis et al. (1994) found the results reported in Fig. 1.2. They argued that the continuum emission looks different from an essentially featureless power-law, suggesting a combination of both thermal and non-thermal contributions to the global solution. The problem of understanding the actual source of the various components is fundamental in our interpretation of the underlying physics, because while thermal emission is typically isotropic, a non-thermal component might be highly collimated and, thus, undermine most of the energetic considerations based on our observations.

Looking at the spectra of Fig. 1.2, it is possible to identify some general signatures of AGN. One of the most interesting features is the large energy excess, which, starting at a wavelength  $\lambda \approx 4000 \text{ \AA}$ , extends deep in the far ultra-violet (FUV), perhaps connecting with the sharp rise of the low X-ray energy tail. It is usually referred to as the *Big Blue Bump* and there is some agreement about the possibility that it could be originated by thermal emission in a mixture of optically thin (free - free) and optically thick (black body) hot plasma, with temperature in the range  $10^4 \text{ K} \leq T \leq 10^6 \text{ K}$ .

Thermal processes are also the most likely explanation of the infrared (IR) excess, long ward of the spectral minimum corresponding to  $\lambda = 1 \mu\text{m}$ , although some contributions from a high energy tail of the synchrotron radio emission cannot be ruled out. The required temperature for this feature is  $T \approx 2000 \text{ K}$ , which is consistent with the presence of dust grains. At higher temperatures, dust is destroyed by sublimation, introducing a physical limit to the emission, which corresponds the characteristic spectral depression.

A large influence of non-thermal processes, on the other hand, is expected in the limiting regions of the electro-magnetic spectrum, both at low and high energy. Radio emission connected to a radio-loud AGN can sometimes be observed up to very large scales ( $R \sim 1 \text{ Mpc}$ ), but the physics in the extended radio sources, such as lobes and jets, is different from the compact source located in the nuclear region. Compact radio sources often have a nearly flat spectrum, with a low frequency cut off attributed to synchrotron self absorptions in a stratified plasma. The presence of interactions among the synchrotron radiation and the relativistic electrons places an upper limit to the radio brightness of the source, since if the radiation energy density  $U_{rad}$  exceeds the average energy density of the magnetic field, photons begin to be inverse-Compton scattered, with high efficiency, to the X-ray and  $\gamma$ -ray domains. Observations at such large energies are much more difficult and require either dedicated space-born instruments or indirect techniques, looking for secondary products of possible interactions of the high frequency photons with matter. The actual origin of AGN X-ray and  $\gamma$ -ray emission is

not completely understood. Some models (e. g. Haardt & Maraschi 1993) invoke inverse-Compton scattering of optical and UV photons in an extremely hot plasma, whereas indications of thermal contributions, at least in the X-rays, cannot be excluded. It has also been observed (see, for instance, Elvis et al. 1990; Wilson et al. 1992) that, while most of the X-ray emission takes origin in the unresolved core, some AGN, especially Seyfert galaxies, show an extended halo, surrounding the nucleus. This is an indication of radiation re-processing by matter at various distances from the source, in a complex balance of processes involving photon scattering, absorption and electron-positron pair production.

### 1.3.2 Emission Lines

As it is illustrated in Fig. 1.2, we are not able to observe AGN emission throughout the whole spectrum of electro-magnetic radiation. On the contrary, we can only explore some specific spectral windows, where radiation is allowed to travel across the intervening medium in the path from the source to our instruments. Out of this range, all the information of continuum emission is lost, because of the opacity of the Earth's atmosphere at millimetric wavelengths and of the large gas column densities absorbing the ionizing UV continuum in our own Galaxy. In any case, the spectra of AGN are often observed with a large number of prominent lines, too, accounting for selective energy emissions and, sometimes, absorptions within the source. The wide range of frequencies covered by these lines is a strong argument in favour of photo-ionization, followed by recombination cascade, as the origin of line emission. Therefore, a careful study of AGN spectral lines is a valuable way to investigate the properties of a poorly known ionizing continuum, as well.

While the absorption lines are usually weak, to the extent that they can often be completely covered by the corresponding emissions, or they are at most detected only in the UV wavelength range of some particular objects, several strong emission lines, distributed in almost every spectral range, are a common property of many types of AGN. As it was anticipated in § 1.2,

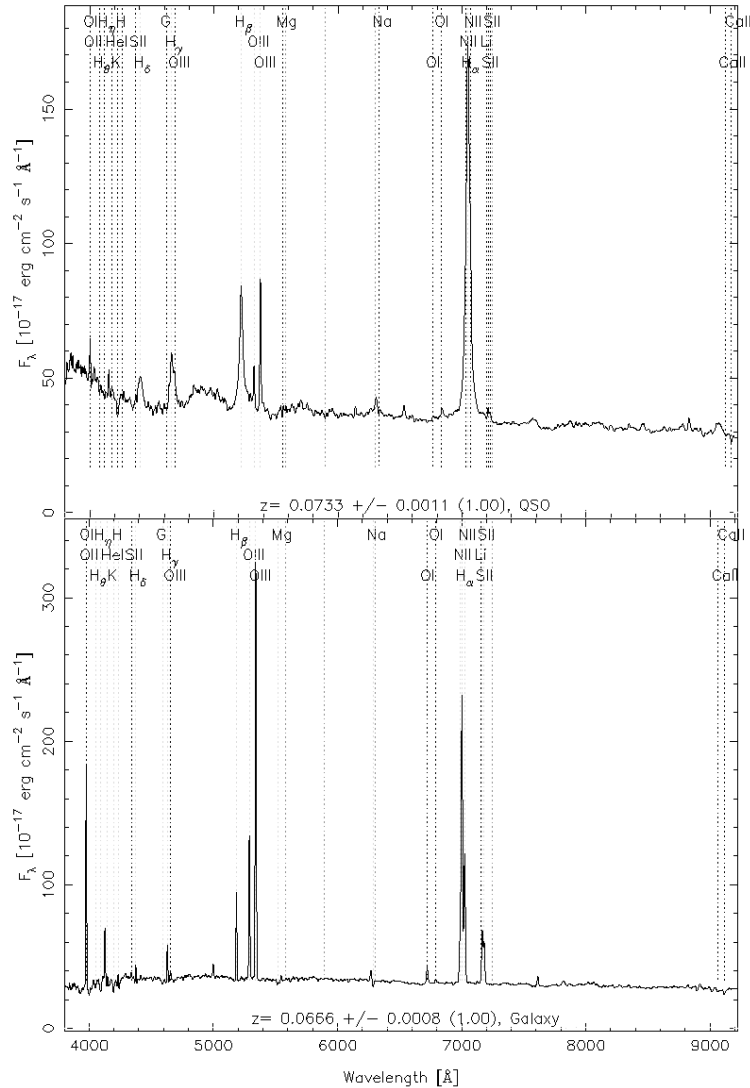


Figure 1.3: Optical spectra of the Seyfert 1 galaxy RX J1307.1+3945 (top) and of the Seyfert 2 IRAS F1515112+1108 (bottom). We note the presence of several identified emission lines. The permitted lines have a prominent broad component in the Seyfert 1 spectrum, which is not detected in the case of forbidden lines and in the Seyfert 2 spectrum. The spectral continuum of Seyfert 1s, moreover, is often found to be relatively stronger at short wavelengths than the corresponding region of Seyfert 2s. The spectra were taken from the Sloan Digital Sky Survey database.

the shape and the strength of the emission lines play an important role in distinguishing among different classes of AGN, but, above all, they place some fundamental constraints on the physics and the structure of the line emitting regions.

Fig. 1.3 illustrates a comparison of the optical spectra of two Seyfert galaxies, belonging to Type 1 and 2, respectively. The spectra are remarkably different and, according to the definition, we observe broad emission lines only in the Seyfert 1 galaxy. However it is clear that only a fraction of the emission lines have a broad component, while the other lines keep their narrow profile in both spectra. The distinction among broad and narrow emission lines is fundamental, because they are originated in different physical conditions, within two regions of the nucleus. Since we detect narrow lines corresponding both to forbidden and permitted transitions, we infer that the narrow line emission must take place in a low density medium, with an electron density  $N_e \leq 10^6 \text{ cm}^{-3}$ . At such low densities, collisions among an excited ion and another particle are rare and the excited level may survive until a spontaneous radiative decay occurs, even if it takes a relatively long time. Otherwise, when the density is higher and collisions among particles are more frequent, ions are removed from the excited stages where the spontaneous radiative decay is slow before the process can occur. In this case, the forbidden transitions become collisionally suppressed.

High resolution observations of nearby sources show that the origin of narrow lines may be attributed to an extended structure, named the Narrow Line Region (NLR), with a typical size in the range  $1 \text{ pc} \leq R_{NLR} \leq 10 \text{ pc}$ , perhaps becoming as large as  $\sim 1 \text{ kpc}$  in the brightest objects. The Broad Line Region (BLR), on the other hand, has a commonly estimated radius of order  $0.01 \text{ pc} \leq R_{BLR} \leq 0.1 \text{ pc}$  and appears as a spatially unresolved spot. It hosts a high density medium, in which only the permitted and some intercombination transitions can take place. Most of the structural properties of the BLR, such as its geometry and the gas distribution and kinematics, still have to be clarified and some of them will be matter of investigation in

this work.

### 1.3.3 AGN variability properties

Most of the observational properties, related to the compact power source of AGN, show a variable behaviour, both in long time scales, of the order of years or months, as well as in short ones, from days down to a few hours. In general, the variability of AGN is not associated with a systematic or periodic trend, but it rather appears to be a random feature. We can usually detect remarkable and quite rapid changes in the high energy spectral range, but the largest variations appear to occur more commonly on long time scales. Some objects, such as the blazar class, are characterized by variations in the form of outbursts. Others, like the Seyfert 1 galaxies, can evolve in time to the extent that their spectral classification may pass through different sub-classes.

A correct interpretation of AGN variability constrains the nature of the processes emitting the various spectral components, unveiling their role in the structure of the source. Given that the most appropriate explanation of the several emission lines, detected in the spectra of many AGN, is photo-ionization induced by the continuum (Osterbrock 1989), we may expect the existence of a relationship among line and continuum variability. This principle is the starting point of the so called *Reverberation Mapping* (RM) technique (see e. g. Blandford & McKee 1982; Wandel 1999; Peterson & Wandel 2000; etc.), which exploits the time elapsed from a significant variation in the ionizing continuum to the corresponding response of the emission lines. The concept is summarized in Fig. 1.4, where the time lag, measured among the continuum and the involved emission line, is interpreted as the delay introduced by light travel time from the continuum source to the photo-ionized medium. By means of RM observations it has been possible to estimate the dimensions of the unresolved BLR of some AGN. It has also been found evidence that the BLR has a stratified structure, with more energetic lines responding slightly sooner than the others. There are no detections of sig-

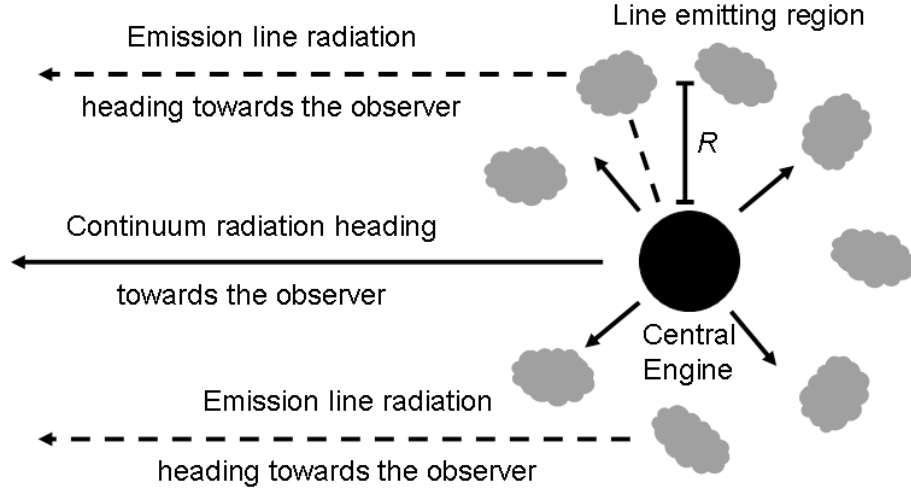


Figure 1.4: Simplified scheme illustrating the concept of Reverberation Mapping. The Central Engine is responsible for the emission of the ionizing continuous radiation, here represented by the solid arrows. Some of the continuous radiation escapes the surrounding environment, eventually falling in the direction of observation, while another fraction interacts with matter close to the source, stimulating line emission (short dashed paths). If  $R$  is the average distance of interaction, a significant variation in the ionizing continuum will produce a corresponding change in the emission lines with a time delay of the order  $\delta t \approx R/c$ , due to the light travel time required to affect the line emitting region with radiation coming from the central engine.

nificant changes in the strength of narrow lines, because the large size of the NLR and its greater distance from the continuum source smooth and delay any possible response well below the observational thresholds of current instrumentation.

The continuum itself, being presumably the result of different processes, should exhibit particular variability properties, according to whether such processes are related or not. For example, one of the major difficulties in the SSC model is that it predicts the high energy spectrum to be produced by interactions of matter with lower frequency radiation, therefore we should

expect high energy variations to follow those at lower frequency. This point has not been definitively worked out, since the relations among high and low energy continuum variations are not simple. In general it is observed that the UV and optical continua vary in phase, with larger amplitude in the UV than in optical radiation, while small scale variations in UV are smoothed out at longer wavelengths. The nearly simultaneous changes in luminosity at different wavelengths complicate the problem of drawing a structural model for AGN, because they should not occur if the source has a radial temperature gradient with local emission efficiency.

## 1.4 The Super Massive Black Hole Model

In the previous sections, we often mentioned the problem of the large amount of energy that is radiated per unit time by a source which is smaller than  $1 \text{ pc}^3$ . Upon considering that the bolometric luminosity of an AGN can easily exceed  $L_{bol} \sim 10^{44} \text{ erg s}^{-1}$ , which is comparable to the power of a galaxy like the Milky Way, the central engine must be much more efficient than stars. The most widespread explanation for such an energetic activity identifies the central engine with matter accretion into the gravitational field of a Super Massive Black Hole (SMBH), located in the centre of the host galaxy. This process involves a large amount of gravitational binding energy, which is transformed into energetic radiation by viscous torques in a dissipative accretion disk.

The black hole model, which is consistent with the common idea that massive black holes should actually be expected in the central regions of every galaxy, either active or quiescent (see for example Ferrarese et al. 2000 and references therein), can be properly tested in a restricted number of cases only. However there are some valuable arguments which support this interpretation by means of very simple order of magnitude considerations.

Assuming that the AGN radiation is isotropic in the inner regions, a lower estimate to the mass of the central source is provided by the Edding-

ton limit. In order to survive disintegration, indeed, the balance between the gravitational force, pulling matter inwards, and the radiation pressure, pushing outwards, has to follow the condition:

$$|F_{rad}| \leq |F_{grav}|. \quad (1.2)$$

Since the momentum carried by a photon with energy  $E = h\nu$  is  $p = E/c$ , at any radius  $r$  there is an outward momentum flux, or pressure, given by:

$$P_{rad} = \frac{L}{4\pi r^2 c}. \quad (1.3)$$

In a completely ionized hydrogen plasma, the net resulting outward force is obtained by the product of Eq. (1.3) with the interaction cross-section of an electron-proton pair, corresponding to the Thomson cross-section:

$$\sigma_e = \frac{8\pi}{3} \left( \frac{e^2}{m_e c^2} \right)^2 = 6.65 \cdot 10^{-25} \text{ cm}^2. \quad (1.4)$$

Given the usual expression for the gravitational force, in the approximation that the electron mass may be neglected, with respect to that of the proton, the condition expressed by Eq. (1.2) becomes:

$$\frac{\sigma_e L}{4\pi c r^2} \leq \frac{GMm_p}{r^2}, \quad (1.5)$$

with  $G$  representing the gravitational constant,  $M$  the central mass, and  $m_p$  the mass of a proton. Eq. (1.5) can be solved for luminosity, yielding the Eddington luminosity limit:

$$L_{Edd} \leq \frac{4\pi G c m_p}{\sigma_e} M \approx 1.26 \cdot 10^{38} (M/M_\odot) \text{ erg s}^{-1}, \quad (1.6)$$

which is the maximum luminosity that a spherical infall of a fully ionized hydrogen plasma may produce, with the central mass expressed in solar units. Alternatively, it can be solved for the mass:

$$M_{Edd} \approx 8 \cdot 10^5 L_{44} M_\odot, \quad (1.7)$$

yielding the minimum mass, again in solar units, required to power the accretion of a source whose luminosity is expressed in units of  $10^{44} \text{ erg s}^{-1}$ .

Therefore, with only simple assumptions, Eq. (1.7) can easily predict central masses  $M \sim 10^8 M_\odot$  in AGN with luminosities  $L \sim 10^{46} \text{ erg s}^{-1}$  (Peterson 1995).

Similar order of magnitude calculations may bring to the prediction of the accretion process efficiency and of the emitted spectrum, as well. The energy radiated by an AGN, indeed, corresponds to some fraction of the rest energy of the inflowing material:

$$L = \eta \dot{M} c^2, \quad (1.8)$$

with  $\dot{M} = dM/dt$  being the amount of mass accreted per unit time. Since energy is extracted from the gravitational potential, we expect:

$$L \approx \frac{GM\dot{M}}{r}, \quad (1.9)$$

for any material flow approaching a distance  $r$  towards the central source. In the case of black holes, we introduce the characteristic *Schwarzschild radius*:

$$R_S = \frac{2GM}{c^2}, \quad (1.10)$$

defining the surface where the escape velocity is equal to the speed of light. Approaching this limit, the gravitational attraction becomes so strong that matter falls into the black hole before it can radiate its energy. A large fraction of the continuum emission is expected to be produced at a distance of  $\sim 5R_S$ , thus the available energy for a particle of mass  $m$  falling towards this distance is:

$$U = \frac{GMm}{5R_S} = \frac{GMm}{10GM/c^2} = 0.1mc^2. \quad (1.11)$$

Therefore, we can expect radiative efficiencies of the order of  $\eta \sim 0.1$ , much larger than the output of thermonuclear reactions turning hydrogen into helium, which yield  $\eta \approx 0.007$ .

A more realistic picture for the central engine of AGN has to consider the loss of angular momentum, which is required to carry material towards the black hole and eventually fuel the nucleus. It is likely that this happens

in an accretion disk. The properties of such systems have been dealt with in many theoretical works (Lynden-Bell 1969; Shakura & Sunyaev 1973; Shields 1978 etc.) and an exhaustive summary is given by Frank, King, and Raine (1992). Given the rate at which gravitational energy is extracted from the infalling material, the virial theorem states that half will heat the gas, while the remainder is radiated away. If energy is dissipated locally in an optically thick medium, we may approximate the emission from the two opposite faces of the disk as a black body:

$$L = \frac{GM\dot{M}}{2r} \approx 2\pi r^2 \sigma T^4, \quad (1.12)$$

where  $\sigma$  is the Stefan-Boltzmann constant. Eq. (1.12) can be rearranged to show that we expect the disk temperature  $T$  to be a function of the radial coordinate in the disk:

$$T(r) = \left( \frac{GM\dot{M}}{4\pi\sigma r^3} \right)^{1/4}. \quad (1.13)$$

Introducing a more detailed treatment of energy dissipation in viscous disks leads to:

$$T(r) = \left\{ \frac{3GM\dot{M}}{8\pi\sigma r^3} \left[ 1 - \left( \frac{R_{in}}{r} \right)^{1/2} \right] \right\}^{1/4}, \quad (1.14)$$

where  $R_{in}$  defines the inner boundary of the disk. Eq. (1.14) can be put in terms of the Schwarzschild radius  $R_S$  and, for  $r \gg R_{in}$ , it can be simplified to the form:

$$T(r) \approx \left[ \frac{3GM\dot{M}}{8\pi\sigma R_S^3} \right]^{1/4} \left( \frac{r}{R_S} \right)^{-3/4}. \quad (1.15)$$

Using the definition of  $R_S$  given in Eq. (1.10), we get to:

$$T(r) \approx \left[ \frac{3c^6}{64\pi\sigma G^2} \right] \dot{M}^{1/4} M^{-1/2} \left( \frac{r}{R_S} \right)^{-3/4}. \quad (1.16)$$

It is possible to express Eq. (1.16) with appropriate units for AGN, so we find that the temperature of an accretion disk may be written as:

$$T(r) \approx 6.3 \cdot 10^5 \left( \frac{\dot{M}}{\dot{M}_{Edd}} \right)^{1/4} M_8^{-1/4} \left( \frac{r}{R_S} \right)^{-3/4} \text{ K}, \quad (1.17)$$

where we introduced the Eddington accretion rate  $\dot{M}_{Edd} = L_{Edd}/\eta c^2$ , required by the source to radiate exactly at its Eddington limit. Eq. (1.17) allows to estimate the temperature of the disk and, consequently, the frequency where most of the radiation is emitted. This is simply done by fixing the condition  $dB_\nu(T)/d\nu = 0$  in the black body emission function of Eq. (1.1).

A very simple prediction of the viscous disk model is that the expected peak temperature in the accretion disk decreases for increasing black hole masses. With typical AGN parameters the emission peak falls in the UV spectral range, whereas black holes with smaller masses should be responsible for strong X-ray emission, as it is actually the case for stellar-size black hole candidates in Galactic binary X-ray sources.

## 1.5 Unification Theories for AGN

In the wide range of sometimes very different objects, that we call AGN, there is only one property shared by all the sources. It is the large amount of energy produced in the extremely compact core region, which makes the SMBH interpretation so attractive. Beyond this fundamental argument, we are left to deal with the problem of explaining how the purported accreting black hole might be responsible for such a heterogeneous family of observational effects as the one summarized in § 1.2. According to the general feeling that the fewer assumptions are required to build a theory, the better is the result, significant efforts were spent in order to draw a self-consistent interpretation of the huge variety of phenomena connected to AGN. This is the basic idea of the *Unified models* for AGN.

Unification theories represent a useful reference frame for our global understanding of AGN physics, since we must be able to develop a comprehensive interpretation of our limited observations, which has to be compared with the severe constraints induced by the actual AGN properties at different scales and epochs in the Universe. The unified models, that try to achieve this result, are subdivided into weak and strong theories, according to the

number of free parameters that are left to account for observational differences in terms of the intrinsic source physical properties. As it was discussed in § 1.3, some fraction of the processes working in the formation of AGN spectral continuum are related to non-thermal emission and, consequently, are likely to be responsible for a high degree of anisotropic emission. Therefore, we can expect the same object to look even very different, according to the line of sight we have towards the source. The strongest possible unification scheme invokes the observational differences we might expect, upon changing the relative orientation of the source with respect to our point of view, as the only free parameter. Although this might succeed in providing an explanation to some particular effects, there are important properties which require more degrees of freedom in the range of the involved physical effects. Typical weak unification models allow for differences in other properties such as the source luminosity, either bolometric or in specific frequency ranges, the strength of magnetic fields, or the properties of the central black hole, essentially its mass, spin, and accretion rate. In this last section, we address the general guidelines and the most valuable features of AGN unified models.

The idea that Type 1 and 2 sources were intrinsically the same kind of object was proposed very soon. It first appeared as the hypothesis that Seyfert 2 galaxies might be Seyfert 1 objects where the BLR is hidden by some amount of obscuring material. In the assumption that the width of the emission lines is controlled by gas kinematics in the gravitational field of the central engine, this explanation agrees with the expectation that the BLR could be more easily obscured than the NLR, since it is smaller and closer to the nucleus. Further considerations on the evidence that Seyfert 2 galaxies are generally fainter than Seyfert 1s and that this appears not to depend on wavelength led to the identification of dust extinction as a likely origin for the observational dichotomy. Looking at the global population of Seyfert galaxies, it was found that approximately 3/4 of the total amount have Seyfert 2 properties, while the remainder are Seyfert 1s. It was inferred that the obscuring structure had to cover a similar fraction of sky, as seen

from the source. The most viable way to carry out this kind of obscuration is to assume that the source is surrounded by an optically and geometrically thick toroidal distribution of dust and molecular gas. Since this structure would hide both the broad lines and the ionizing continuum, which, instead, can actually be observed, a further component, in the form of a scattering medium located above the torus equatorial plane, was invoked. The basilar geometry is illustrated in Fig. 1.5, with some of the possible observational configurations.

A fundamental contribution to the onset of the torus model, as a realistic interpretation of Seyfert galaxies, came from some observations of Seyfert 2 galaxies in polarized light (e. g. Antonucci & Miller 1985; Miller et al. 1991). As a matter of fact, linear polarization is a strong indication of photon scattering in the source. It was found that some Seyfert 2 galaxies have a polarized component, whose spectrum looks very similar to that of Seyfert 1s, largely supporting the deduction that a directly hidden Seyfert 1 nucleus emits its signal in a highly beamed fashion, but some of its light is subsequently scattered off the original beam, eventually falling into our line of sight. The high degree of light polarization in the continuous spectrum of NGC 1068 is an emblematic case, suggesting that this interpretation is very likely to be correct, at least for some Seyfert 2 galaxies.

There are some problems with the torus model, however, suggesting that it may not be the complete picture. The high degree of linear polarization, which we should expect in the case of single scattering above the equatorial plane, is not particularly common, then multiple photon scatterings and Faraday rotation are likely to be at work. Moreover, since we consider Seyfert galaxies as the faint tail of the QSO sequence and QSO generally exhibit Type 1 spectra, we should be able to identify a class of Type 2 QSO, as well. It was argued, for example in Jannuzi et al. (1994), that such objects exist in the form of bright far-infrared (FIR) galaxies, but it is also possible that the more energetic emission of QSO can prevent the formation of a thick, dusty torus at all. The situation of radio-loud objects is further complicated by

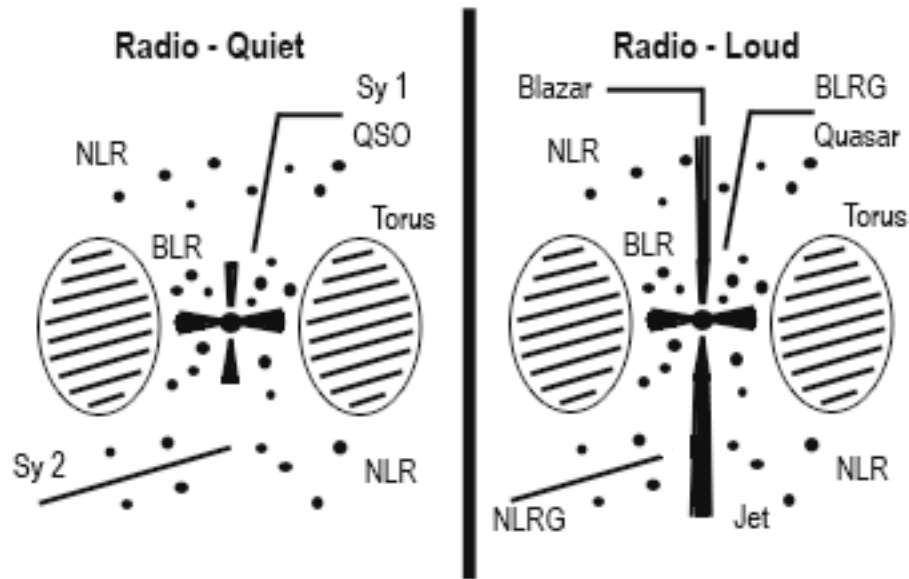


Figure 1.5: Schematic representation of the dusty torus unification models. The central engine, represented by the black hole and accretion disk, is surrounded by a dusty molecular torus (the shaded region), which prevents observation of the BLR and continuum source from view points located at small inclinations above the torus equatorial plane. At higher inclinations the central regions become visible. A scattering medium surrounding the source may be responsible for deflecting photons of the continuum and broad emission lines onto the torus equatorial plane. In these models the exact classification of the source depends on its orientation and on the ability of the matter accretion process to power a jet.

the distinction among the compact and the extended components. Although we can expect the emission from the compact source to be considerably beamed and aspect dependent, this is clearly not the case for the extended component. High resolution observations of compact sources have been able, in some cases, to reveal a jet, or generally linear structure, aligned with the axis of the larger scale extended emission. In apparent contradiction with the symmetric appearance of the extended emitting region, with respect to

the compact one, jets are often one-sided. We observe, in any case, that relativistic motions are a common feature of jets, thus relativistic beaming of radiation largely enhances the brightness of the approaching side of the jet, hiding the receding counterpart. Spectropolarimetry of the extended emission regions strongly supports this idea, because linear polarization in the direction of the hidden jet is clearly smaller than what we measure in the opposite direction, indicating that radiation from the former region travels a longer path in depolarizing medium than the emission of the latter, which we infer to be the nearest (Garrington et al. 1988, Laing 1988).

A basilar issue for AGN unification models is to assess whether it is possible to provide a realistic explanation for the distinction among radio-loud and radio-quiet objects. On simple numerical grounds, we know that radio-loud sources represent a small minority of the entire range of possible configurations, although the fraction of luminous radio sources may rise up to  $\sim 50\%$ , if we restrict to the brightest objects. Comparisons of the two populations in other frequency ranges revealed more important details. Wilkes & Elvis (1987) found that the soft X-ray spectra of radio-loud objects is flatter than it is in radio-quiet, while the UV portion appears to be almost indistinguishable (Steidel & Sargent 1991). Stronger optical Fe II is usually characteristic of radio quiet AGN (Boroson & Green 1992). These features can hardly be fitted in a radio-quiet / radio-loud unification scheme, so the most common feeling is that radio-loudness should be regarded as an intrinsic physical property.

Wilson & Colbert (1995) carried out a model where they explain the radio-loudness of AGN in terms of the central black hole spin rate. They assume that the continuum emission in the spectrum, from X-ray down to the IR emission, has a thermal origin, raising from matter which accretes onto the SMBH. The radio jets, on the contrary, come from mechanical energy extracted in the vicinity of the black hole, a process which can be shown to increase in efficiency if the SMBH is spinning rapidly. The origin of a radio-loudness dichotomy would, then, be related to the spin rate distribution of

the black holes. Such distribution, in the case of SMBH, is not particularly affected by accretion processes, but it rather depends on the black hole growth history through the occurrence of important mergers. Indeed, the outcome of a merger depends on the relative sizes of the merging black holes, which is, in its turn, related to the sizes of the host galaxies. Since high spin rates can be achieved by mergers of black holes having comparable masses and, moreover, objects with very large masses are relatively fewer, the model predicts that:

1. the most frequent situation involves merging of quite common, although different in size, black holes, which would result in a moderate mass, slowly spinning black hole, i. e. a radio-quiet AGN;
2. if the black hole masses are comparable, the resulting object would have a high spin rate and produce a radio-loud AGN;
3. the rarest event would be the interaction of two black holes of comparable and large mass, whose result would be a bright radio-loud AGN.

The predictions of this model appear to be in fairly good agreement with the empirical scenario, eventually providing a viable solution to the problem of describing the complex AGN phenomenology in the framework of the accreting black hole interpretation.



# Chapter 2

## Astrophysical Plasma Spectroscopy

### 2.1 Introduction

The physics of interactions between radiation and diffuse gaseous matter is of great interest in many astrophysical sources. Photons with an energy above the threshold value of  $E = h\nu = 13.6\text{ eV}$  are able to ionize hydrogen atoms in their ground configuration and to provide free electrons and ions. The exceeding energy of the photons is carried in the medium as kinetic energy of the electrons extracted from ions. Subsequent inter-particle collisions may either exchange the kinetic energy, approaching a Maxwell-Boltzmann distribution, or they can transform it into other kinds of energy, such as ion excitation energy or free-free and free-bound radiation, due to electron accelerations in the collisions and to the possible recombinations.

Given the large abundance of hydrogen in the Universe, it is very likely that high energy photons will be absorbed by matter close to their origin, the exact distance depending on the gas density and on the radiation frequency. For this reason, astrophysical sources of ionizing radiation are often surrounded by a photo-ionized plasma, which we usually detect by means of characteristic emission line spectra. Physical conditions in these *nebular en-*

*vironments* are controlled by the balance of photo-ionization processes, which heat the gas, because they transfer energy from the ionizing radiation field to electrons and ions, and of the energy losses due to the emissions, which, on the contrary, cool down the material.

In this chapter we review some fundamental aspects of the energy exchange between matter and radiation in plasmas. We conclude with a description of how the resulting physical conditions affect the properties of some emission lines.

## 2.2 Thermodynamical Equilibrium in Plasmas

Most of the physical processes, which we commonly observe in the world, involve energy exchanges among different systems. The spontaneous evolution of systems is towards a configuration of maximum probability, where energy is equally distributed, in its various manifestations, between the connected parts of a system. In this situation, the system reaches a dynamical stability, in the sense that each process affecting a certain amount of energy is balanced by an opposite phenomenon, so that no net variations are observed.

The situation described above is referred to as a condition of *Thermodynamical Equilibrium* (TDE). If the physical system in TDE is a plasma of free electrons and ions, the energy distribution of particles, their excitation status, and their ionization ratios are bounded to some specific conditions.

Kinetic energy is distributed among the particles, until their velocities settle down to the Maxwell-Boltzmann distribution:

$$f(v)dv = 4\pi \left( \frac{m}{2\pi k_B T} \right)^{3/2} v^2 \exp \left( -\frac{mv^2}{2k_B T} \right) dv. \quad (2.1)$$

Deviations from this configuration are quickly erased by elastic collisions.

The thermal excitation of ions follows the Boltzmann formula:

$$\frac{N_{im}}{N_{i1}} = \frac{g_{im}}{g_{i1}} \exp \left( -\frac{\chi_{im}}{k_B T} \right), \quad (2.2)$$

expressing the population of the  $m^{\text{th}}$  excited level, with respect to the ground configuration, in the  $i^{\text{th}}$  ion species. Here, the factor  $g_{im}$  ( $m \geq 1$ ) expresses

the statistical weight of the  $m^{\text{th}}$  level, while  $\chi_{im}$  represents the excitation energy required to bring an electron from the fundamental level to the excited one.

Finally, the ionization ratios of a given element are expressed by the Saha equation:

$$\frac{N_{i+1}}{N_i} P_e = 2 \frac{u_{i+1}(T)}{u_i(T)} \frac{(2\pi m_e)^{3/2} (k_B T)^{5/2}}{h^3} \exp\left(-\frac{\chi_i}{k_B T}\right), \quad (2.3)$$

which describes the ratios among the  $i+1$  times ionized species and the  $i$  times ionized one ( $i \geq 0$ ). In Eq. (2.3) we represent with  $P_e$  the electron pressure and with  $\chi_i$  the energy threshold required to extract a further electron from an  $i$  times ionized species. The function  $u_i(T)$  is called *partition function*. It is defined as:

$$u_i(T) = \sum_m g_{im} \exp\left(-\frac{\chi_{im}}{k_B T}\right), \quad (2.4)$$

and it takes into account the statistical weights of all the excited levels of the  $i^{\text{th}}$  ion species.

If the plasma is in condition of TDE, all the processes, that establish the previous relations, are driven by inter-particle collisions and the temperatures, which are referred to in equations (2.1), (2.2), and (2.3) agree to the same value. This situation is approximately met in systems with very high particle densities, where collisions are likely to dominate over the other kinds of processes. However, this is not the most common case for astrophysical conditions. Many environments, instead, are characterized by the presence of a low density plasma, interacting with a radiation field, where the importance of interactions among matter and radiation grows with respect to collisions, introducing deviations from TDE.

## 2.3 Radiation Transfer

Light propagation across a material medium is controlled by the effects of interactions among matter and radiation. In general, we expect the outcoming

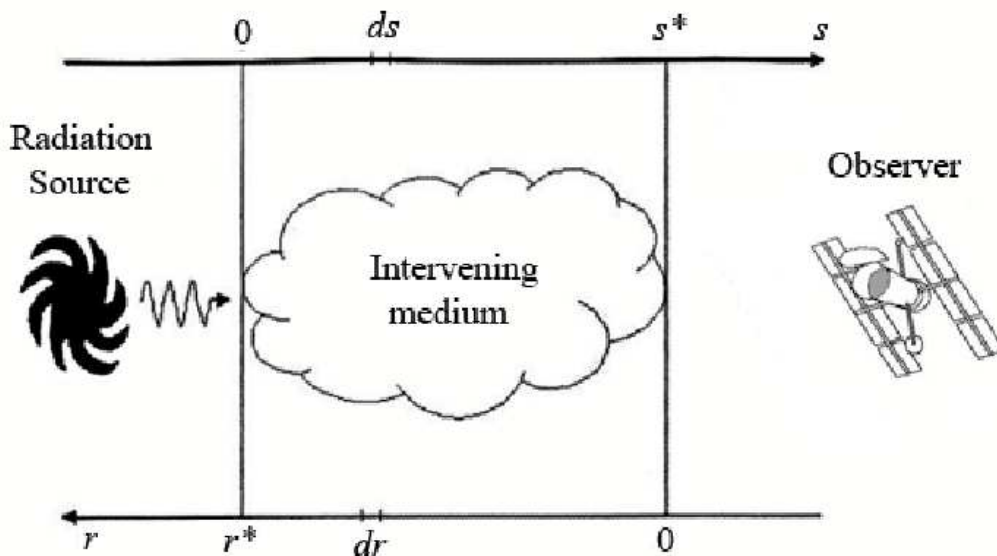


Figure 2.1: Geometry of the radiation transfer problem: light from an astrophysical source travels a path, from  $s = 0$  to  $s = s^*$ , across the intervening material, which is located in the direction towards the observer. The observer, instead, measures the distance from the near side of the path to the source, along the coordinate  $r$ .

radiation beam to be quite different from the original one, both in its direction and energy. The processes which affect the light beam are summarized in the concept of *radiation transfer*, ruled by the so called *transfer equation*.

Let's consider, for example, the simple situation illustrated in Fig. 2.1, where a light beam, emitted from some kind of distant source, passes through an intervening medium, before getting to the observer. In order to describe what happens to the radiation, we need the definition of some physical entities:

**Specific Intensity**  $I_\nu = dE_\nu / (dA \cos \theta d\omega dt d\nu)$ , defined as the amount of energy crossing the surface element  $dA$  with an inclination  $\theta$ , with respect to the surface normal, in a beam covering the solid angle  $d\omega$ , during the time lag  $dt$ , in the frequency interval  $d\nu$ , and measured in

units of  $\text{erg cm}^{-2} \text{s}^{-1} \text{Hz}^{-1} \text{sterad}^{-1}$ ;

**Emission Coefficient**  $j_\nu = dE_\nu / (ds dA \cos \theta d\omega dt d\nu)$ , corresponding to the amount of energy emitted by the volume element covered by the surface  $dA \cos \theta$  in a path of length  $ds$ , with the same inclination  $\theta$  on the surface normal direction, in the beam of solid angle  $d\omega$ , during the time lag  $dt$ , in the frequency interval  $d\nu$ , and measured in units of  $\text{erg cm}^{-3} \text{s}^{-1} \text{Hz}^{-1} \text{sterad}^{-1}$ ;

**Absorption Coefficient** defined by  $k_\nu I_\nu = -dE_\nu / (ds dA \cos \theta d\omega dt d\nu)$ , which measures the amount of energy subtracted from the radiation field in the same conditions and it is measured in units of  $\text{cm}^{-1}$ .

The change in the specific intensity of radiation, after travelling a path  $ds$  in the medium, might be generally expressed in the form:

$$dI_\nu = j_\nu ds - k_\nu I_\nu ds, \quad (2.5)$$

which, after dividing by the length element  $ds$ , gives the differential form of the transfer equation:

$$\frac{dI_\nu}{ds} = -k_\nu I_\nu + j_\nu. \quad (2.6)$$

In order to estimate the specific intensity of the radiation field across the material, we have to solve Eq. (2.6). If we turn to the observer's point of view, measuring distances along the coordinate  $r$ , with  $dr = -ds$ , we can introduce the *optical depth* of the medium according to:

$$\tau_\nu^* = \int_0^{r^*} k_\nu dr = - \int_{s^*}^0 k_\nu ds, \quad (2.7)$$

resulting in the differential relations  $d\tau_\nu = k_\nu dr = -k_\nu ds$ . These can be used in Eq. (2.6), upon dividing both members by  $-k_\nu$ , to get:

$$\frac{dI_\nu}{d\tau_\nu} = I_\nu - \frac{j_\nu}{k_\nu}. \quad (2.8)$$

It is of common use to define the *source function* as the ratio:

$$S_\nu = \frac{j_\nu}{k_\nu}$$

among the emission and absorption coefficients in Eq. (2.8). Now, to integrate Eq. (2.8), we multiply both members by  $\exp(-\tau_\nu)$ :

$$\begin{aligned} \frac{dI_\nu}{d\tau_\nu} \exp(-\tau_\nu) &= I_\nu \exp(-\tau_\nu) - S_\nu \exp(-\tau_\nu) \\ \frac{d}{d\tau_\nu} [I_\nu \exp(-\tau_\nu)] &= -S_\nu \exp(-\tau_\nu). \end{aligned} \quad (2.9)$$

Referring to the geometry of Fig. 2.1, we may call  $I_{\nu 0}$  the specific intensity of radiation hitting the material on the side of the source, i. e.  $I_{\nu 0} = I_\nu(\tau_\nu^*)$ , then we can integrate along the radiation path to the opposite boundary of the medium, to obtain the emergent radiation intensity:

$$\begin{aligned} I_\nu(\tau_\nu^*) \exp(-\tau_\nu^*) - I_\nu(0) &= - \int_0^{\tau_\nu^*} S_\nu \exp(-\tau_\nu) d\tau_\nu \\ I_\nu(0) &= I_{\nu 0} \exp(-\tau_\nu^*) + \int_0^{\tau_\nu^*} S_\nu \exp(-\tau_\nu) d\tau_\nu. \end{aligned} \quad (2.10)$$

Clearly, the result of Eq. (2.10) depends on what is actually known about the source function of the intervening material. Its physical interpretation, however, is particularly interesting, since it states that the emergent radiation on the near side of the medium (where  $\tau_\nu = 0$ ) results from the sum of the incident radiation field, attenuated by the whole amount of intervening material, and of any contribution arising within this matter, attenuated by the path corresponding to its depth in the medium.

A simple example of the meaning of Eq. (2.10) arises if  $S_\nu$  can be considered as a spatially constant function. In this case, the emergent radiation field specific intensity becomes:

$$I_\nu(0) = S_\nu [1 - \exp(-\tau_\nu^*)] + I_{\nu 0} \exp(-\tau_\nu^*), \quad (2.11)$$

which can be shown to predict either  $I_\nu(0) \approx S_\nu$ , if  $\tau_\nu^* \gg 1$ , or, alternatively,  $I_\nu(0) = \tau_\nu^*(S_\nu - I_{\nu 0}) + I_{\nu 0} \approx I_{\nu 0}$ , if  $\tau_\nu^* \ll 1$ . Put in other words, if the medium is optically thick, it may hide the radiation source to our sight, while if it is optically thin, light from the original source is only weakly affected.

## 2.4 Photo-Ionization Equilibrium

When a beam of ionizing radiation travels across a gaseous medium, it produces a series of interactions, which affect the ionization structure of matter. The details of the resulting configuration depend both on the characteristics of the radiation field and on the properties of the intervening medium, such as its density and chemical composition. The global balance of photo-ionizations and recombinations control the physical conditions of the plasma, which we may eventually be able to see in the resulting spectrum. A detailed treatment of photo-ionization equilibrium requires to take into account a complex set of processes, each one involving different ion species, with their characteristic interaction cross-sections. The typical energies of various reactions, moreover, can overlap and affect each other. In order to explain the fundamental mechanisms which are influencing the global balance, we shall start our analysis from a simple situation and then introduce the complicated effects of a more realistic scenario.

### 2.4.1 Photo-Ionization of a Pure Hydrogen Plasma

In the case of a pure hydrogen gas, the ionization equilibrium is obtained by the balance of photo-ionizations and subsequent recombinations:

$$N_{HI} \int_{\nu_0}^{\infty} \frac{4\pi J_{\nu}}{h\nu} a_{\nu}(\text{H I}) d\nu = N_e N_p \alpha(\text{H I}, T), \quad (2.12)$$

with  $J_{\nu}$  being the mean intensity of radiation, measured in *cgs* units as  $\text{erg cm}^{-2} \text{s}^{-1} \text{Hz}^{-1} \text{sterad}^{-1}$ , while  $N_{HI}$ ,  $N_e$ , and  $N_p$  are, respectively, neutral hydrogen, free electron, and ionized hydrogen particle densities, given as particles in inverse  $\text{cm}^3$ . Here we also represent with  $a_{\nu}(\text{H I})$  the ionization cross section of a H I atom, with respect to a photon with energy  $h\nu$ , and with  $\alpha(\text{H I}, T)$  the recombination coefficient of the electron and ion to a neutral atom, which is a function of temperature. To a good approximation, we may express the radiation field mean intensity as the emission of the source

reduced by the inverse square dilution effect upon distance:

$$4\pi J_\nu = \frac{R^2 F_\nu(R)}{r^2} = \frac{L_\nu}{4\pi r^2}, \quad (2.13)$$

where  $R$  is the radius of the source,  $F_\nu(R)$  the radiation flux at its surface, and  $L_\nu$  the source luminosity per unit frequency.

The ionization equilibrium of a pure hydrogen gas, in a given radiation field, can be calculated if we know the ionization and recombination cross sections. If we consider the hydrogen atom as a multiple level system, indicating each level with the conventional notation  $n^{2s+1}L$ , where  $n$  is the principal quantum number,  $L$  is the angular momentum quantum number, expressed as  $S, P, D, F, \dots$  for  $L = 0, 1, 2, 3, \dots$  ( $L < n$ ), and  $s$  is the spin quantum number, permitted transitions occur among levels with  $\Delta L = \pm 1$  and  $\Delta s = 0$ . The probabilities of permitted transitions are in the range from  $10^4 \text{ s}^{-1}$  to  $10^8 \text{ s}^{-1}$  and, thus, the corresponding lifetimes of the excited levels vary from  $10^{-4} \text{ s}$  to  $10^{-8} \text{ s}$ . Although a direct transition of the form  $2^2S \rightarrow 1^2S$  is forbidden, it can occur by formation of a virtual intermediate level, with the emission of two continuum photons in a typical timescale of order 0.12 s. It is estimated that the mean lifetime of an atom, against photo-ionization, is much longer in any common astrophysical scenario, then we can conclude that all H I atoms are ionized from their ground level, while recombinations can occur to any excited level, with a following sequence of downward transitions, leading the system back to its fundamental stage.

As a consequence, our only concern about photo-ionization is the cross section of the process in the fundamental level, which, for an hydrogenic ion with nuclear charge  $Z$ , is known to be:

$$a_\nu(Z) = \frac{A_0}{Z^2} \left(\frac{\nu_1}{\nu}\right)^4 \frac{\exp\{4 - [(4 \arctan \epsilon)/\epsilon]\}}{1 - \exp(-2\pi/\epsilon)}, \quad (2.14)$$

where  $\nu \geq \nu_1$  and:

$$A_0 \approx 6.30 \cdot 10^{-18} \text{ cm}^2, \quad (2.15)$$

$$\epsilon = \sqrt{\frac{\nu}{\nu_1} - 1}, \quad (2.16)$$

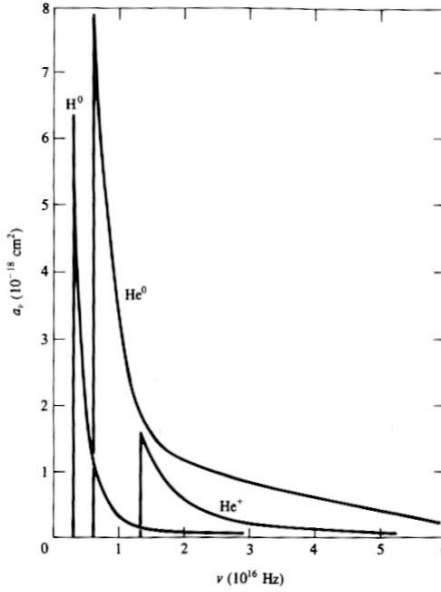


Figure 2.2: Photo-ionization cross section of H I, He I, and He II as a function of the ionizing radiation frequency. The cross section is null below the threshold frequency, it has a maximum at the threshold, which is characteristic of the ion, then it quickly decreases at higher frequencies, so that more energetic radiation penetrates deeper into the ionized material. From Osterbrock (1989).

with the threshold energy fixed by the relation:

$$h\nu_1 = Z^2 h\nu_0 = 13.60 Z^2 \text{ eV}. \quad (2.17)$$

The photo-ionization cross section of Eq. (2.14) is plotted in Fig. 2.2 for some fundamental ions. It drops approximately as  $\nu^{-3}$ , so that more energetic photons are likely to penetrate deeper in the gas.

The energy distribution of the free electrons initially depends on the properties of the ionizing radiation field, but it tends to settle in the Maxwell-Boltzmann form, because the cross section for elastic collisions among particles is considerably larger than for other processes, that transform the kinetic energy of electrons to other forms of energy. The rate of collisions, then, is

controlled by the local temperature and the recombination coefficient to the level  $n^2L$  becomes:

$$\alpha_{n^2L}(\text{H I}, T) = \int_0^\infty v \sigma_{n^2L}(\text{H I}, v) f(v) dv, \quad (2.18)$$

where  $\sigma_{n^2L}(\text{H I}, v)$  is the recombination cross section of electrons with velocity  $v$  in H I to the term  $n^2L$ , which is found to vary as  $v^{-2}$ . In nebular conditions, any recombination quickly brings ions to their ground level and it is convenient to adopt the global recombination coefficient:

$$\alpha_A = \sum_{n,L} \alpha_{n^2L}(\text{H I}, T), \quad (2.19)$$

which, for pure hydrogen at  $T = 10^4$  K, is  $\alpha_A \approx 4.18 \cdot 10^{-13} \text{ s}^{-1}$ , corresponding to a typical recombination time  $\tau_r \approx 2.4 \cdot 10^{12} / N_e$  s.

The transfer equation for ionizing radiation takes the form of:

$$\frac{dI_\nu}{ds} = -N_{\text{H I}} a_\nu I_\nu + j_\nu. \quad (2.20)$$

A common way to handle the problem is to subdivide the radiation field in a *source* component, coming directly from the central object, and a *diffuse* one, generated within the medium, so that:

$$I_\nu = I_{\nu s} + I_{\nu d}. \quad (2.21)$$

The source radiation is attenuated by the effects of geometrical dilution and absorption and it can be expressed as:

$$4\pi I_{\nu s} = F_{\nu s}(R) \frac{R^2 e^{-\tau_\nu}}{r^2}, \quad (2.22)$$

with  $\tau_\nu$ , the optical depth at frequency  $\nu$ , given by:

$$\tau_\nu(r) = \int_0^r N_{\text{H I}}(s) a_\nu ds. \quad (2.23)$$

In the case of the diffuse radiation field, the transfer equation becomes:

$$\frac{dI_{\nu d}}{ds} = -N_{\text{H I}} a_\nu I_{\nu d} + j_\nu. \quad (2.24)$$

Provided that  $k_B T \ll h\nu_0$ , the only source of diffuse ionizing radiation is the direct recombination of free electrons to the ground level, whose emission coefficient can be written in the form:

$$j_\nu(T) = \frac{2h\nu^3}{c^2} \left( \frac{h^2}{2\pi m_e k_B T} \right)^{3/2} a_\nu \exp \frac{-h(\nu - \nu_0)}{k_B T} N_p N_e, \quad (2.25)$$

and it is strongly peaked near  $\nu = \nu_0$ . The total number of photons generated by such recombinations is controlled by the ground level recombination coefficient:

$$4\pi \int_0^\infty \frac{j_\nu}{h\nu} d\nu = N_p N_e \alpha_{1^2S}(\text{H I}, T) \quad (2.26)$$

and it results that the mean intensity of the diffuse radiation component is averagely smaller than the source component. In the case of an optically thin nebula, it is possible to assume that  $I_{\nu d} \approx 0$ , while, for optically thick gas, a commonly adopted assumption is the *on the spot* approximation, stating that every ionizing photon resulting from a diffuse radiation field is re-absorbed next to its origin, eventually giving no net contribution to the ionization balance.

Making the *on the spot* approximation and using Eq. (2.22) into the ionization equation (2.12), we get:

$$\frac{N_{\text{HI}} R^2}{r^2} \int_0^\infty \frac{F_\nu(R)}{h\nu} a_\nu e^{-\tau_\nu} d\nu = N_p N_e \alpha_B(\text{H I}, T), \quad (2.27)$$

where we introduced  $\alpha_B(\text{H I}, T) = \alpha_A(\text{H I}, T) - \alpha_{1^2S}(\text{H I}, T)$ .

For any given input spectrum, Eq. (2.27) can be computed to estimate the gas ionization fraction as a function of  $r$ , the distance from the source. What is commonly observed is that, in the presence of an ionizing radiation field, hydrogen is kept nearly fully ionized within a critical radius  $r_1$ , sometimes called the *Strömgen radius*, which can be estimated in Eq. (2.27) if we make the substitution:

$$\frac{d\tau_\nu}{dr} = N_{\text{HI}} a_\nu, \quad (2.28)$$

from Eq. (2.23), and we integrate over  $r$ :

$$R^2 \int_{\nu_0}^\infty \frac{F_\nu(R)}{h\nu} d\nu \int_0^\infty d(-e^{-\tau_\nu}) = \int_0^\infty N_p N_e \alpha_B r^2 dr. \quad (2.29)$$

Since the ionization is nearly complete within  $r_1$  and it sharply drops towards zero outside this radius, Eq. (2.29) takes the form of:

$$R^2 \int_0^\infty \frac{F_\nu(R)}{h\nu} d\nu = \frac{1}{3} r_1^3 N_{\text{H}}^2 \alpha_B, \quad (2.30)$$

in which  $N_{\text{H}}$  is the total hydrogen density. Recalling that the source luminosity at frequency  $\nu$  is  $L_\nu = 4\pi R^2 F_\nu(R)$ , we get:

$$\int_{\nu_0}^\infty \frac{L_\nu}{h\nu} d\nu = Q(\text{H I}) = \frac{4\pi}{3} r_1^3 N_{\text{H}}^2 \alpha_B, \quad (2.31)$$

where we introduced the number of ionizing photons emitted by the source  $Q(\text{H I})$ . Eq. (2.31) tells us that the number of ionizing photons produced by the source is balanced by the total number of recombinations to any excited level within a sphere of radius  $r_1$ .

### 2.4.2 Photo-Ionization of Chemically Complex Gas

In a realistic astrophysical environment, the gas is a chemical mixture of elements, with different electron configurations and ionization potentials. Helium (He) is the most abundant species, after hydrogen, with a typical numerical abundance of order  $\sim 10\%$ . It is a two-electron system with a first ionization energy threshold of  $h\nu_2 = 24.6 \text{ eV}$  and a value of  $h\nu_3 = 54.4 \text{ eV}$  for its complete ionization. Clearly, photons above these energy thresholds are able to ionize H, as well, but, because of the strong dependence of the photo-ionization cross section on radiation frequency, illustrated in Fig. 2.2, they are much more likely to be absorbed by He.

On the other hand, the presence of He does not remove ionizing radiation from the field, because recombinations of electrons into He leads to the emission of various photons that can still ionize H. The result involves the formulation of more equations in the form of Eq. (2.23), where the number of photo-ionizations must be corrected for the fraction of He recombinations, leading to the emission of an ionizing photon, while the electron density is modified by the presence of electrons coming from He. The presence of heavier elements gives rise to conceptually similar, but much more complicated coupling effects.

The actual ionization structure of the medium depends on the energy distribution of the ionizing radiation field. If there is a large number of high energy photons, they dominate the ionization process of all the available species as far as they penetrate the medium. In this case, the fraction of ionized gas extends almost uniformly out to a cut-off radius, where the ionizing radiation is completely absorbed. On the other hand, as soon as the number of high energy photons becomes smaller, the ionization structure of the medium assumes a stratified appearance, with the species having a higher ionization threshold exhibiting the radial cut-off closer to the source.

## 2.5 Thermal Equilibrium

It was mentioned, in the first sections of this chapter, that TDE is not a correct description for nebular environments. Astrophysical plasmas are constantly exchanging their energy with the surrounding space, mainly by means of interactions with radiation. Although photo-ionizations are numerically balanced by recombinations, the net result of the process is gas heating. This happens because the free electrons, extracted by radiation, carry an energy excess, given by the difference between the energy of the ionizing photon and the ionization threshold, which is commonly above the average kinetic energy of the other particles. Since these electrons are fast, their recombination cross section is small, until they are slowed down, after redistributing their kinetic energy excess within the medium. When they finally recombine, some of their energy is radiated away in the recombination and subsequent transition cascade, but a certain fraction of the original ionizing photon energy is left in the gas, increasing its temperature.

The temperature of the plasma, however, cannot rise indefinitely, because the plasma itself becomes an emitting source, which radiates away some of the energy excess, allowing it to cool down. Simple recombinations cannot balance heating by photo-ionization, but a number of other processes, such as thermal *bremstrahlung*, which is emitted by electrons that are slowed down

in close encounters with ions, and, mainly, the collisional excitation of low energy levels in some abundant ions, which is followed by radiative decay to the ground configuration, may transfer energy from the electrons to photons that are eventually able to leave the system.

Summing up together all the processes which contribute to the heating and cooling of the gas, it is possible to evaluate their total balance and, therefore, to estimate the temperature where these processes have the same efficiency. This is a condition of *Thermal Equilibrium* (TE) and it is written in the form of an equation between energetic gains and losses:

$$G(T) - L_R(T) = L_{FF}(T) + L_C(T), \quad (2.32)$$

where  $G(T)$  is the energy input by photo-ionization, while  $L_R(T)$ ,  $L_{FF}(T)$ , and  $L_C(T)$  are the losses due to recombinations, free-free radiation, and de-excitation of collisionally charged levels, respectively. The reason for putting  $L_R(T)$  together with the energy gain  $G(T)$  is to stress that photo-ionization and recombination are strongly coupled in the ionization equilibrium.

### 2.5.1 Photo-ionization and Recombination

The amount of energy injected in a plasma by photo-ionization can be thought of as the average energy excess of an ionizing photon, with respect to the ionization threshold of the involved species, multiplied by the number of photo-ionizations. In the case of photo-ionization of hydrogen, the rate of heating can be expressed as:

$$G_H(T) = N_{\text{HI}} \int_{\nu_0}^{\infty} \frac{4\pi J_{\nu s}}{h\nu} h(\nu - \nu_0) a_{\nu}(\text{HI}) d\nu. \quad (2.33)$$

Substituting Eq. (2.12), we can remove  $N_{\text{HI}}$  and, in the on the spot approximation, re-write Eq. (2.33):

$$G_H(T) = N_e N_p \alpha_B(\text{HI}, T) \frac{\int_{\nu_0}^{\infty} \frac{4\pi J_{\nu s}}{h\nu} h(\nu - \nu_0) a_{\nu}(\text{HI}) d\nu}{\int_{\nu_0}^{\infty} \frac{4\pi J_{\nu s}}{h\nu} a_{\nu}(\text{HI}) d\nu}. \quad (2.34)$$

The energy loss, due to recombinations, is given by:

$$L_H(T) = N_e N_p k_B T \beta_B(\text{HI}, T), \quad (2.35)$$

with:

$$\beta_B(\text{HI}, T) = \sum_{n=2}^{\infty} \sum_{L=0}^{n-1} \beta_{nL}(\text{HI}, T), \quad (2.36)$$

being the global effective recombination coefficient in the on the spot approximation, which is built by summing up together the coefficients of the single terms:

$$\beta_{nL} = \frac{1}{k_B T} \int_0^{\infty} v \sigma_{nL}(\text{HI}, T) \frac{1}{2} m v^2 f(v) dv. \quad (2.37)$$

An exact description of the role played by photo-ionizations and recombinations involves more contributions in the form of equations (2.34) and (2.35), accounting for ionization and recombination of He and heavier elements, computed with the appropriate ionization and recombination coefficients. A sum of the available contributions fixes the heating and cooling rates of these processes.

### 2.5.2 Thermal Bremsstrahlung

The Coulomb interaction in a close encounter between two charged particles in a plasma leads to charge acceleration. According to the principles of electro-magnetism, this means that some kind of radiation must be emitted. The largest contribution to this process comes from encounters among electrons and ions, because the significant mass difference implies that electrons are strongly deflected. The subsequently emitted radiation takes its energy away from the kinetic energy of electrons, which are slowed down, thus cooling the gas.

Since electrons are not captured in the encounter, this phenomenon is called either free - free radiation, or thermal bremsstrahlung (i. e. braking radiation), and it results in the emission of a continuous spectrum from the plasma. The corresponding cooling rate depends on the average speed of electrons, the most common ion species, and the density of the plasma. It can be put in the form:

$$L_{FF}(Z) = 1.42 \cdot 10^{-27} Z^2 T^{1/2} g_{ff} N_e N_{ion} \text{ erg cm}^{-3} \text{ s}^{-1}, \quad (2.38)$$

where  $Z$  is the net ion charge,  $N_{ion}$  the ion number density, and  $g_{ff}$  is the *Gaunt factor* for free - free emission, a weak function of  $T$  and  $N_e$ , that is generally in the range  $1.0 \leq g_{ff} \leq 1.5$  for nebular environments.

Most of the free - free radiation involves abundant ions, like H II and He II, which are both well represented by Eq. (2.38), because they have the same net charge. However, thermal bremsstrahlung is not the dominant cooling process, unless the plasma becomes really hot.

### 2.5.3 Cooling by Collisionally Excited Radiation Emission

One of the most important cooling processes, in astrophysical plasmas, is the energy loss by spontaneous radiative decay of collisionally excited levels of ions. Since the energy of a level, that is going to be excited by a collision, cannot exceed the average energy carried by free electrons, which is of order  $k_B T$ , heavy ions are more effective coolers than H or He. Although they are relatively rare, their complex electronic configuration produces a large number of possible transitions, whose energy thresholds have the same order of magnitude of the average kinetic energy in free electrons. The low abundance of these ions, together with the circumstance that many of the involved levels decay to the ground configuration by means of a forbidden radiative transition, give the photon a large chance to escape the medium and, thus, to take energy away from the gas.

The collisional excitation of a level can only occur if the energy of the colliding particles is at least equal to the excitation energy  $\chi$  of the upper level in the transition. The cross section for the process is found to vary as  $v^{-2}$ , so that it is expressed in the form of:

$$\sigma_{12}(v) = \frac{\pi \hbar^2}{m^2 v^2} \frac{\Omega(1, 2)}{g_1}, \quad (2.39)$$

where  $mv^2/2 > \chi$  and  $\Omega(1, 2)$  is called the *collision strength*, a function of the electron energy.

In conditions of TDE, each collisional excitation by an electron, within a specific velocity range, would be followed by a collisional de-excitation producing an electron in the same velocity range. The cross sections for excitation and de-excitation can be shown to follow:

$$g_1 v_1^2 \sigma_{12}(v_1) = g_2 v_2^2 \sigma_{21}(v_2), \quad (2.40)$$

with:

$$\frac{1}{2} m v_1^2 = \frac{1}{2} m v_2^2 + \chi. \quad (2.41)$$

Using Eq. (2.40) in Eq. (2.39), we are able to express the de-excitation cross section in terms of the collision strength:

$$\sigma_{21}(v_2) = \frac{\pi \hbar^2}{m^2 v_2^2} \frac{\Omega(1, 2)}{g_2}, \quad (2.42)$$

meaning that the collision strength is symmetric, no matter whether the transition is an excitation or a de-excitation.

It is possible to write down the number of collisional de-excitations occurring in the plasma as:

$$N_e N_2 Q_{21} = N_e N_2 \int_0^\infty v \sigma_{21} f(v) dv, \quad (2.43)$$

where  $Q_{21}$  is the collisional transition rate coefficient, representing the number of transitions occurring by collisions per unit time in a medium of unit density (measured in  $\text{cm}^3 \text{s}^{-1}$ ). An analogous coefficient expresses the collisional excitation rate as  $N_e N_1 Q_{12}$ . The relationship between  $Q_{12}$  and  $Q_{21}$  can be evaluated in condition of TDE, when the number of collisional excitations is the same as that of de-excitations:

$$N_e N_1 Q_{12} = N_e N_2 Q_{21} \quad (2.43)$$

and, using the Boltzmann equation (2.2), it turns out that:

$$Q_{12} = \frac{g_2}{g_1} Q_{21} \exp\left(-\frac{\chi_{21}}{k_B T}\right). \quad (2.44)$$

If the levels are in statistical equilibrium, meaning that the number of excitations is equal to the number of de-excitations, so that the total amount of ions in a level does not change in time, we can write the balance equation:

$$N_e N_1 Q_{12} = N_e N_2 Q_{21} + N_2 A_{21}, \quad (2.45)$$

where  $A_{21}$  is the probability of a spontaneous radiative decay and, therefore,  $N_2 A_{21}$  gives the number of radiative transitions. Eq. (2.45) gives the population ratio in presence of collisional transitions and radiative decays as:

$$\frac{N_2}{N_1} = \frac{N_e Q_{12}}{A_{21}} \left[ 1 + \frac{N_e Q_{21}}{A_{21}} \right]^{-1}. \quad (2.46)$$

Cooling of the gas can actually occur when the excited levels fall back to the ground configuration by a radiative decay. This means that:

$$L_C = N_2 A_{21} h \nu_{21}. \quad (2.47)$$

Substituting  $N_2$  in Eq. (2.47) by means of Eq. (2.46), we find that:

$$L_C = N_e N_1 Q_{12} h \nu_{21} \left[ 1 + \frac{N_e Q_{21}}{A_{21}} \right]^{-1}. \quad (2.48)$$

It can be easily shown that, in the limit of very low densities, as  $N_e \rightarrow 0$ , Eq. (2.48) takes the form of:

$$L_C = N_e N_1 Q_{12} h \nu_{21}, \quad (2.49)$$

meaning that every collisionally excited level eventually leads to a radiative decay. On the other hand, if  $N_e \rightarrow \infty$ , the population ratio in Eq. (2.46) reduces to:

$$\frac{N_2}{N_1} = \frac{Q_{12}}{Q_{21}} = \frac{g_2}{g_1} \exp\left(-\frac{\chi_{21}}{k_B T}\right), \quad (2.50)$$

i. e. the Boltzmann distribution of Eq. (2.2), expected when collisions dominate above the other processes.

On the basis of these considerations, we infer the existence of a critical density, defining a threshold above which the line emission is no longer able to cool the gas. The value of the critical density depends on the probability that

an excited level may fall back to the fundamental status through a radiative decay, before the electron is removed from the level by further collisions. For the transition among an excited level 2 to the fundamental one, it is defined as:

$$N_c = \frac{A_{21}}{Q_{21}}. \quad (2.51)$$

Eq. (2.51) clearly shows that spontaneous transitions having low transition probabilities, like the forbidden ones, are associated to very low critical densities, therefore we do not detect the corresponding emission lines from regions with a high density plasma.

The complete description of collisional cooling can involve more complex statistical equations, describing the population of a large number of levels connected by collisional transitions and subsequent decays. The exact nature of the resulting system depends on the particular ion species in the plasma.

## 2.6 Physical Properties from Emission Lines

In the previous sections of this chapter, we discussed how the physical conditions of an astrophysical source are affected by interactions among matter and radiation. The population of excited stages of atoms, which are eventually allowed to return to their ground level by radiative decays, produces an emission line spectrum. Studying the properties of different emission lines, we may be able to understand under which conditions the gas is emitting and, possibly, even to perform a chemical analysis of the medium.

The electron temperature of plasmas can be fairly well estimated, if we are able to identify emission lines coming from collisionally excited levels of a specific ion, with different energies. In a plasma of ions and free electrons, the electron temperature determines the velocity distribution of these light particles and, therefore, the energies they can exchange with ions during collisions. As soon as the temperature is higher, electron - ion collisions are able to populate more energetic levels. Some particular ions, such as [O III] and [N II], have energy structures that can give raise to a system

of transitions, with different upper level excitation energies, corresponding to easily observed optical frequencies. In the low density limit, the line emissivity ratios of these ions mainly depend on the collision strengths and the transition probabilities of the excited levels. However, when the number of free electrons approaches the critical density of a transition, collisional depopulation of the level becomes important, too, and the ratio is consequently affected. Among the most commonly exploited temperature indicators, the emissivity ratio of [O III]  $\lambda 4363$  Å with respect to the [O III]  $\lambda 4959, 5007$  Å doublet behaves as:

$$\frac{j_{4959} + j_{5007}}{j_{4363}} \simeq \frac{7.73 \exp(3.29 \cdot 10^4/T)}{1 + 4.5 \cdot 10^{-4}(N_e/T^{1/2})}, \quad (2.52)$$

while that of [N II]  $\lambda 5755$  Å with respect to the [N II]  $\lambda 6548, 6583$  Å doublet follows:

$$\frac{j_{6548} + j_{6584}}{j_{5755}} \simeq \frac{6.91 \exp(2.50 \cdot 10^4/T)}{1 + 2.5 \cdot 10^{-3}(N_e/T^{1/2})}, \quad (2.53)$$

in remarkable analogy with the previous. The difference in ionization potential of these species implies that equations (2.52) and (2.53) should be used to investigate the temperature of regions filled by plasmas with different degrees of ionization.

Using lines from such ions has a number of practical advantages, with respect to other available choices, but it is limited to low density systems, where the line emission can actually occur. The forbidden nature of the involved transitions, indeed, makes the nebula optically thin to the emission line photons, that emerge from the plasma in the same ratio at which they were created. Furthermore, even the effect of interstellar differential absorption does not dramatically influence their ratio, because the involved wavelength ranges are not particularly extended, and it can be easily accounted for. These conditions are generally not satisfied by recombination lines, whose strengths can be significantly affected by resonance scattering and differential extinction. Moreover, the relative intensities of many recombination lines are controlled by the recombination coefficients in the different excited levels, which have a very similar dependence on temperature among

themselves.

Excited levels with very similar energies, instead, provide a good indicator of the electron density. If two levels of nearly identical excitation energy have different radiative transition probabilities or collisional de-excitation rates, the relative intensities of the corresponding lines will depend on electron density. The upper levels of these transitions are similarly filled by collisions, so the resulting line intensity ratio is affected by the critical densities of the transitions. Emission lines from ions such as [O II], at  $\lambda = 3726, 3729 \text{ \AA}$ , or [S II], at  $\lambda = 6716, 6731 \text{ \AA}$ , are commonly exploited, but many others, due, for example, to [N I], [Cl III], [Ar IV], [K V], [Ne IV] might be available to probe different ionization regions.

When these fundamental parameters have been estimated, considerations on the strength of different emission lines can lead to infer the abundance of the detected ions.



# Chapter 3

## Physical Processes in the BLR

### 3.1 Introduction

Many AGN have broad emission lines in their spectra. These are originated very close to the central source of ionizing radiation, in a compact volume which is called Broad Line Region (BLR - see, for example, Osterbrock 1989; Krolik 1999; Peterson 2003). As it was mentioned in Chapter 1, the BLR is so small that it cannot be probed by direct observations with our instruments, even in the nearest AGN. Because of this difficulty, we are not yet able to trace a complete and self-consistent picture of the physics in the BLR. Although we were able to identify some of its fundamental properties, by means of careful investigations of spectroscopic data, many details about its structure, its dynamics, and the effects of interactions with the intense AGN radiation field still have to be clarified.

Typically the only emission lines, that are associated with a prominent broad component in a type 1 AGN spectrum, come from radiative decays with a quite high transition probability. As a consequence of Eq. (2.51), they have a correspondingly large critical density and they can be emitted even in a relatively high density plasma. On the other hand, the forbidden emission lines, that have a much smaller probability of spontaneous radiative decay, are collisionally weakened by a factor of order  $\sim N_c/N_e$ , which

becomes more constraining as soon as the line critical density is lower. Forbidden emission lines, such as those emitted by [O III] at  $\lambda = 4959, 5007 \text{ \AA}$  are usually observed to have extremely weak broadening, if any, suggesting that the gas must be denser than the critical value of these transitions, which is  $N_c([\text{O III}]) \approx 10^6 \text{ cm}^{-3}$ . For the same reason, the presence of clearly detectable broad components in some intercombination lines, like the UV emission of C III] at  $\lambda = 1909 \text{ \AA}$ , whose critical density is  $N_c(\text{C III]}) \approx 10^{10} \text{ cm}^{-3}$ , fixes an upper limit to the actual density in the plasma. An intermediate guess of  $N_e \approx 10^9 \text{ cm}^{-3}$  is usually assumed to represent the average value of electron density in the BLR, although even large intrinsic variations may take place within the plasma.

Because of its high density and strong interaction with the ionizing radiation field, the BLR plasma of AGN is very different from the nebular environment that is found in other astrophysical sources. In this chapter we discuss some implications of these differences and we describe the physical picture which is developing on the basis of our current understanding of the BLR properties. We report about the progress in techniques and observations, that will be exploited in our study, introducing the main open questions, which we are going to examine in our work.

## 3.2 The Standard Cloud Model

There are several arguments supporting the idea that photo-ionization must be the most important process in the production of the broad emission lines. At the typical densities, estimated for the BLR environment, a reliable guess to the plasma temperature can be drawn, for example, from the C III]  $\lambda 977 / \text{C III] } \lambda 1909$  line ratio, yielding upper temperature limits of  $T \approx 25000 \text{ K}$ . This is far too low to achieve double collisional ionization of C and consistent with the expected temperature of a photo-ionized plasma. Furthermore, since the BLR is located at a small distance from the central engine, it certainly interacts with the intense ionizing radiation coming from the continuum source

(Bahcall et al. 1972; Blandford & McKee 1982), as it is demonstrated by correlated evolution of the continuum and broad line emission.

The presence of several lines, emitted by low ionization species, such as Mg II and Fe II, implies that the broad line emitting gas must be optically thick for the ionizing radiation. Moreover, it must fill a small fraction of the volume surrounding the continuum source, or, otherwise, it would prevent the ionizing radiation to be detected at all. Evidence coming from the emission line profiles, which are fairly similar even for transitions involving species with very different ionization potentials, suggests that line emission takes place in a large number of independent kinematical units, where all the observed transitions occur at similar rates. Combining these clues together led to the formulation of the Standard Cloud Model for the BLR, which assumes that the line emitting entities are clouds of dense gas, moving under the dynamical influence of the central engine (Bahcall & Kozlovsky 1969a, b; Davidson 1972; MacAlpine 1972; etc.). The aim of this model is to predict the spectrum of a single cloud, by means of photo-ionization calculations, once some important parameters are given, such as the ionizing radiation SED, the shape of the cloud, the gas pressure, its column density, its chemical composition, and the corresponding ionization structure.

The Standard Cloud Model has some important difficulties, for example in the interpretation of the mechanical equilibrium of the clouds and the surrounding environment, furthermore it gives no physical explanation to the origin of clouds and their nature. Actually, there are no direct indications concerning the geometry of the clouds and, since this is an important parameter, different assumptions, in this sense, provide the basis for several variants of the fundamental model.

### 3.2.1 Cloud Stability

The physical interpretation of the BLR properties in terms of clouds, though attractive, is problematic. Combining some order of magnitude estimates about the gas density and cloud dimensions, it results that the line emitting

entities are well below the Jeans limit for self-gravitating gas structures. Thus, it is required that some external factor prevents cloud disintegration before the broad line spectrum can be emitted.

The study of the BLR properties is more conveniently handled by introducing some appropriate indicators of the physical conditions in the gas. The time scale required to reach ionization equilibrium in the radiation field is called the *recombination time* and it is defined as:

$$t_{rec} = \frac{1}{\alpha N_e} \simeq 10^{-5} N_{10}^{-1} \text{ years}, \quad (3.1)$$

where  $\alpha$  is an average recombination coefficient and  $N_{10}$  is the particle density, given in units of  $10^{10} \text{ cm}^{-3}$ . It controls the change in physical conditions within the gas, as a consequence of variability in the ionizing photon flux. The *dynamical time* measures how long it takes for a cloud to travel across the BLR at its typical velocity  $v_{avg}$ , so that<sup>1</sup>:

$$t_{dyn} = \frac{R_{BLR}}{v_{avg}} \simeq 30 L_{46}^{1/2} \text{ years}, \quad (3.2)$$

in which  $R_{BLR}$  is an estimate to the size of the BLR and  $L_{46}$  is the source luminosity in units of  $10^{46} \text{ erg s}^{-1}$ . Dynamical equilibrium within a single cloud is controlled by the *sound crossing time*:

$$t_{sc} = \frac{R_c}{c_s} \simeq 2 \cdot 10^{-12} T_e^{-1/2} R_c \text{ years}, \quad (3.3)$$

where  $R_c$  is the typical cloud size in cm and the sound speed in the gas is represented by  $c_s = \sqrt{2k_B T_e / m_p}$ . Eq. (3.3) gives the estimated life-time of a cloud, when it is not in equilibrium.

It is also very useful to introduce the so called *ionization parameter*:

$$U = \frac{\int_{\nu_0}^{\infty} L_{\nu} d\nu}{4\pi r^2 c N_e}, \quad (3.4)$$

expressing the ratio among the ionizing photon number density and the electron density at a distance  $r$  from the source, and its ratio with respect to the

---

<sup>1</sup>To estimate the dynamical time we assume a relationship between the size of the BLR and the luminosity of the AGN central source. This topic will be further discussed in § 3.3.

electron temperature:

$$\Xi = \frac{\int_{\nu_0}^{\infty} L_{\nu} d\nu}{4\pi r^2 T_e c N_e} = \frac{U}{T_e}, \quad (3.5)$$

which is essentially proportional to the ratio among radiation pressure and gas pressure and we shall call it the *pressure parameter*. Although the ionization parameter  $U$  would be correctly expressed by Eq. (3.4) only in the case of a pure hydrogen gas, it is still a precious indicator of the ionization structure in a chemically complex gas. A large ionization parameter, indicating that many ionizing photons are present, corresponds to sharp transitions in the ionization structure of the gas, while a small value of  $U$  predicts extended regions of gradual transition in the ionization of matter.

Studying the interactions among matter and radiation in the AGN environment revealed the possibility that high and low energy ionizing radiations actually affect matter through distinct processes. Over a limited range of ionization the thermal balance of these two phases would produce different equilibrium temperatures. Krolik et al. (1981) argued that the dynamical stability of clouds could, then, be explained in terms of a pressure equilibrium between a cold ( $T_e \sim 10^4$  K), dense gas phase, in the clouds, and a *hot intercloud medium* (HIM) with a temperature mainly controlled by Compton scattering processes:

$$T_{HIM} = \frac{h\bar{\nu}}{4k_B} \sim 10^8 \text{ K}, \quad (3.6)$$

where  $\bar{\nu}$  represents some average photon frequency, which is a characteristic of the ionizing radiation field. This model, illustrated in Fig. 3.1, predicts the existence of stable gas configurations over the ranges where the condition:

$$\frac{d \ln T}{d \ln \Xi} > 0 \quad (3.7)$$

is satisfied. When the condition, expressed in Eq. (3.7), is not met, the system becomes thermodynamically unstable, breaking the gas in a two-phase configuration, which eventually moves toward the stable branches of the diagram at high and low temperatures. The assumption of theoretical ionizing radiation fields, represented by broken power law distributions in frequency, provided a fair possibility to achieve the pressure equilibrium among the hot

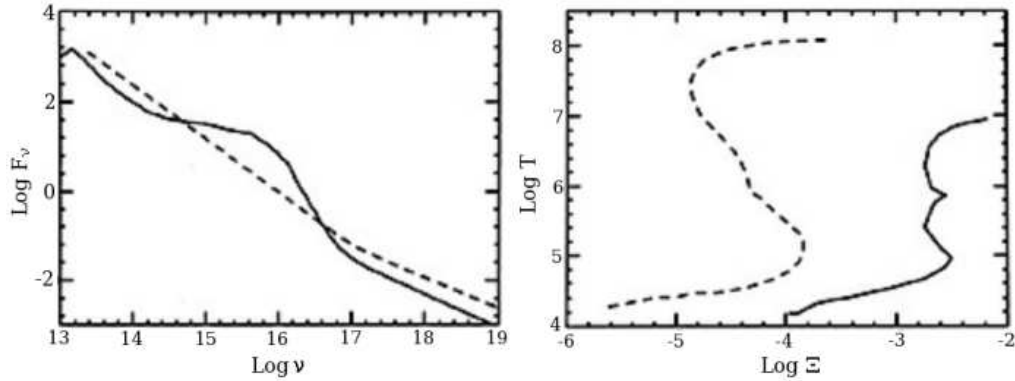


Figure 3.1: Two-phase gas equilibrium in the BLR of AGN for different choices of the ionizing continuum SED. In the left panel we show the adopted continuous spectra, which are a broken power law (dashed line) and an empirical standard SED (continuous line). The corresponding gas configurations are illustrated in the right panel, where we see that the assumption of the empirical SED cannot account for the existence of a two-phase equilibrium with appropriate gas temperatures. Plots are from Netzer (1990).

and the cold gas phases at the desired temperatures and in a range of pressure parameter values, which was in good agreement with early observations (Lepp et al. 1985; Kallman & Mushotzky 1985; Krolik 1988). Unfortunately, as soon as more detailed information about the actual SED of AGN ionizing radiation became available, the range of pressure parameter values, allowing the two-phase system to achieve pressure equilibrium, was significantly reduced, and the predicted temperature of the HIM dropped to such low values, that it should give raise to undetected scattering and absorption signatures in the spectra (Fabian et al. 1986; Mathews & Ferland 1987).

The difficulties in the formulation of a realistic solution for the two-phase configuration, together with the lack of any certain signature of the HIM in spectra, took to the investigation of several possible alternatives. It was suggested that cloud confinement could be provided by magnetic forces (see, for instance, Rees 1987). In other models, clouds are formed in radiatively accelerated winds (e. g. Smith & Raine 1985; Perry & Dyson 1985), or they

are originated from the surface of accretion disks (Shlosman et al. 1985; Collin-Souffrin et al. 1988; Dumont & Collin-Souffrin 1990). Other authors, instead, suggest that the clouds could be related to the bloated atmospheres of stars in interaction with the AGN radiation field (Voit & Shull 1988; Penston 1988; Scoville & Norman 1988; Kazanas 1989), or even that they do not need to be preserved, since they can radiate while dissipating (Kwan & Carroll 1982; Carroll & Kwan 1985; Carroll 1985).

### 3.2.2 The BLR Structure with Clouds

As far as the emission line intensities are concerned, an appropriate choice of the model parameters may produce photo-ionization predictions in reasonable agreement with the observations, but for a single cloud. The calculation of the composite spectrum requires a definition of how the contribution of several clouds are combined together. This problem can be solved by specifying some physical properties of the clouds, such as their number density  $n_c$ , the cloud particle density  $N$ , the emissivity  $j_c$ , the velocity  $v$ , and their geometrical cross section  $A_c$ , as measured from the point of view of the central source. If the clouds are optically thick, energy conservation implies that the total emergent luminosity is equal to the amount of energy absorbed by the gas. The cloud emissivity, in a specific line, is then related to the flux emitted in the line per unit projected surface element  $\varepsilon_l$  (measured in  $\text{erg s}^{-1} \text{cm}^{-2}$ ) and to the cloud's cross section, according to:

$$j_c(r) = A_c(r)\varepsilon_l(r). \quad (3.8)$$

Assuming that the dependence of these parameters on  $r$  may be expressed in the form of:

$$\left\{ \begin{array}{l} \varepsilon_l(r) \propto r^{-m} \\ n_c(r) \propto r^{-p} \\ A_c(r) \propto r^{-q} \\ N(r) \propto r^{-s} \\ v(r) \propto r^{-t} \end{array} \right. \quad \begin{array}{l} (3.9a) \\ (3.9b) \\ (3.9c) \\ (3.9d) \\ (3.9e) \end{array}$$

it is possible to integrate over various BLR structural models, to predict the cumulative spectrum. Introducing the concept of *covering factor*  $C(r)$ , as the fraction of sky covered by one cloud at a distance  $r$  from the source, we have:

$$C(r) = \frac{A_c(r)}{4\pi r^2}, \quad (3.10)$$

which, for a thin spherical shell of clouds with thickness  $dr$ , becomes:

$$dC(r) = A_c(r)n_c(r) dr \propto r^{-(p+q)} dr. \quad (3.11)$$

In this simple geometry, the total flux emitted in a line can be expressed as:

$$E_l \propto 4\pi \int_{r_{in}}^{r_{out}} A_c(r)n_c(r)\varepsilon_l(r)r^2 dr, \quad (3.12)$$

resulting in:

$$E_l(r) \propto \begin{cases} \frac{1}{3-(p+q+m)} \left[ \left(\frac{r_{out}}{r_{in}}\right)^{3-(p+q+m)} - 1 \right] & \text{if } (p+q+m \neq 3) \\ \ln\left(\frac{r_{out}}{r_{in}}\right) & \text{if } (p+q+m = 3) \end{cases} \quad (3.13a)$$

$$(3.13b)$$

If we consider the case of a system of spherical clouds, having radius  $R_c(r)$ , with a virial motion distribution, and in pressure equilibrium with an environment medium, the number of parameters depending on distance can be reduced. Since the dependence of the kinetic temperature on the ionization structure of a photo-ionized gas is weak, the pressure  $P$  scales with distance  $r$  approximately in the same way as the density  $N$  ( $\propto r^{-s}$ ). In these conditions, the product  $R_c^3 N$  is constant, and the cloud cross section becomes:

$$A_c(r) \propto R_c^2 \propto N^{-2/3} \propto r^{2s/3}, \quad (3.14)$$

which, compared with Eq. (3.9c), results in  $q = -2s/3$ . Applying mass conservation to the distribution of clouds in virial motion, it results that the product  $n_c(r)v(r)r^2$  must be constant and, since  $t = 1/2$ , we get  $p = 3/2$ . Bringing these results into Eq. (3.11), we get, for the covering factor:

$$dC(r) \propto r^{2s/3-3/2} dr. \quad (3.15)$$

In a system of optically thick clouds, the total amount of radiation emitted is proportional to the covering factor, therefore, integrating Eq. (3.15) across the BLR, we find:

$$E_l(r) \propto \frac{1}{2s/3 - 1/2} \left[ \left( \frac{r_{in}}{r_{out}} \right)^{2s/3 - 1/2} - 1 \right], \quad (3.16)$$

provided that  $s \neq 3/4$ . Comparing the result of Eq. (3.16) with the general expression of Eq. (3.13a) (where we introduce the constraints  $q = -2s/3$  and  $p = 3/2$ , deduced in this simplified treatment), we find, for the flux emitted in a line  $\varepsilon_l(r)$ , that  $m = 2$ . This conclusion is a good approximation for many observed lines, although a dependence of the properties of the line emitting material on the ionization parameter  $U$  might be important and, thus, change the balance of interactions among matter and radiation at different radii.

### 3.3 BLR Kinematics from the Emission Line Profiles

The distribution of the broad line emitting gas and its motion pattern affect the profiles of the emission lines. Since the gas moves under the dynamical influence of the central engine, the characteristic wavelengths of the several observed transitions are modified by the Doppler effect:

$$\lambda_{obs} = \lambda_0 \sqrt{\frac{1 + v/c}{1 - v/c}}, \quad (3.17)$$

where we denote with  $\lambda_{obs}$  and  $\lambda_0$ , respectively, the measured and the intrinsic wavelength of a spectral line, while  $v$  represents the projection of the gas velocity onto the direction of our line of sight. If the velocity field is such that  $v \ll c$ , then Eq. (3.17) simplifies to:

$$\lambda_{obs} \simeq \lambda_0 \left( 1 + \frac{v}{c} \right), \quad (3.18)$$

therefore a range of radial velocities  $\Delta v$  in the emitting gas produces spectral features that are broadened in wavelength according to:

$$\Delta\lambda = \lambda_0 \frac{\Delta v}{c}. \quad (3.19)$$

The velocity fields inferred from the profiles of the spectral lines in many type 1 AGN commonly exceed  $10^3 \text{ km s}^{-1}$  or even  $10^4 \text{ km s}^{-1}$ , with a large variety of shapes. The resulting line profiles can be regarded as the cumulative contributions of a system of clouds, moving along specific trajectories across the BLR.

At present, very little is known about the actual distribution of clouds and the nature of the dynamical influence which is driving their motion. However, extensive Reverberation Mapping campaigns are providing more and more useful suggestions in this sense. As we mentioned in Chapter 1, RM exploits the time lag elapsed from a change in the ionizing continuum to the corresponding answer of the emission lines to estimate the size of the line emitting region. This is done by observing a specific source for several times, at regular intervals, and recording the brightness of the spectral continuum and that of one or more emission lines. The time covered by the observational campaign must be considerably longer than the typical variability time scale of the object under investigation, while the gap between the single observations must be shorter. It is also important that the variability time scale is large with respect to the recombination time,  $t_{rec}$  in Eq. (3.1), and small with respect to the dynamical time,  $t_{dyn}$  in Eq. (3.2), because, otherwise, the line emitting region would not be able to answer coherently. Assuming that the SED of the ionizing continuum does not change significantly during variations and that it is the only source of ionization for the line emitting medium, it is possible to reconstruct the light curves of the continuum and of the emission lines as a function of time. The two functions can be subsequently cross-correlated, evaluating a *cross-correlation function* (CCF), which is essentially a set of correlation coefficients of the curves shifted by different amounts of time. The peak of this function is named the *cross-correlation time*  $\tau_{XC}$  and it is considered as the time lag to be spent before the ionizing radiation can reach the line emitting region and force a response of the line. The cross-correlation radius of the BLR is, then, simply computed as:

$$R_{BLR} = c \tau_{XC}. \quad (3.20)$$

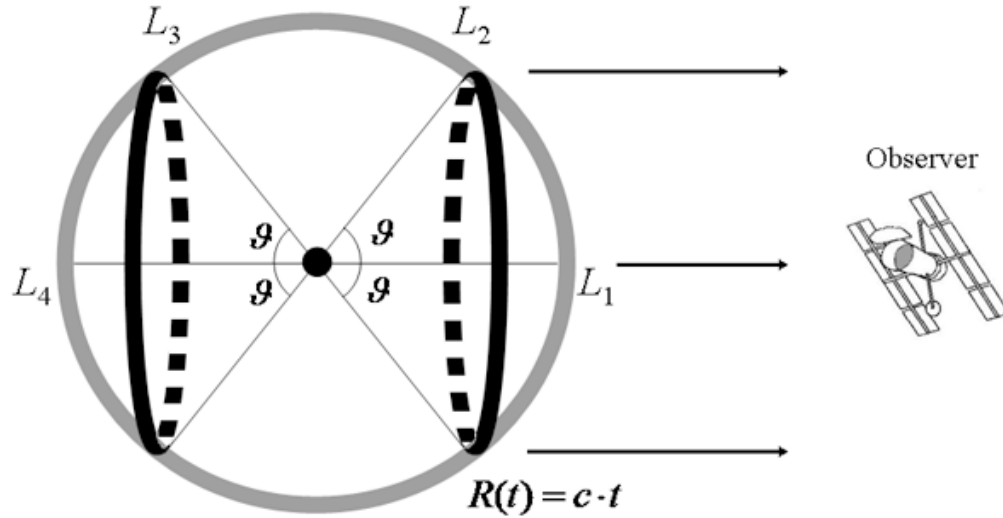


Figure 3.2: Geometry of the emission line reverberation corresponding to an isotropic pulse of ionizing radiation (gray shaded region). All the points located on the spherical surface with  $R(t) = ct$  are illuminated simultaneously, but the following line emission reaches the observer with a delay, depending on the different path of the line photons.  $L_1$  answers almost immediately, while  $L_2$ ,  $L_3$ , and  $L_4$  react later and later. Therefore, if an emission line is originated in these points, its profile must change in time, according to the velocity field therein.

More detailed calculations predict that the emission lines will not respond uniformly to a change in the ionizing radiation field, since different parts of the line profile are originated in different places within the broad line emitting medium. Let's consider, for example, the situation illustrated in Fig. 3.2: we assume that a pulse of continuum radiation is emitted isotropically by the central engine, then it propagates radiatively outwards. As soon as the ionizing photons reach the gas located in the BLR, they interact with clouds driving line emission. In the assumed geometry, it is obvious that the line emission signal will reach the observer with a delay, which depends on the location where the interaction took place. A measurement of the delay, which characterizes a specific component of the emission line profile, constrains the

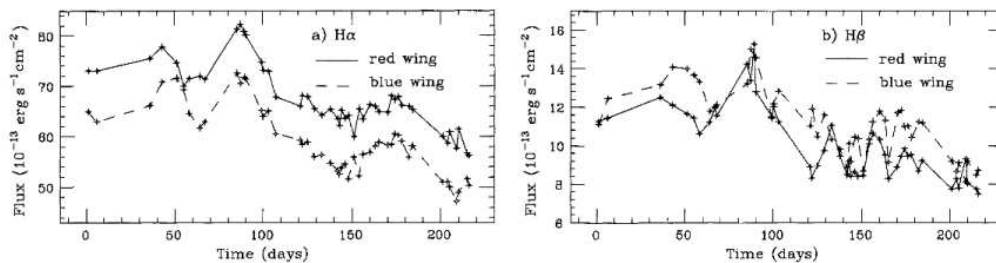


Figure 3.3: Emission line light curves for the broad components of  $H\alpha$  (panel *a*) and  $H\beta$  (panel *b*) in NGC 4151. The fluxes of the blue and red line wings are measured separately as a function of time. There are no significant differences in the light curves of the opposite wings, indicating that the BLR kinematical structure cannot be represented by an isotropic radial flow of gas. Data are from Maoz et al. (1991).

structure of the velocity field being responsible for that component (see, for instance, Peterson 1987; Stirpe et al. 1988; Zheng et al. 1995; Wanders & Peterson 1996; Kollatschny & Dietrich 1996, 1997).

A specific example concerns the case of radial gas flows in the BLR, where the blue and red line wings would be produced by the approaching and receding gas streams. If the gas were moving outwards, the approaching gaseous stream would be also the nearest (located in  $L_1$  in Fig. 3.2) and a variation of the ionizing continuum should be followed much more quickly by the blue wing of an emission line than it should be recorded for the red one. The opposite, instead, would apply if the gas were radially falling towards the centre. Indeed, neither of these situations is clearly detected in the light curves of the most well studied AGN, as it is shown in Fig. 3.3 for NGC 4151 (Maoz et al. 1991), suggesting that radial flows are not a dominant kinematical component. Peterson & Wandel (1999) found that, in the well sampled nucleus of NGC 5548, RM data are, instead, consistent with a Keplerian motion distribution within the BLR. They show that the emission line profiles are related to the time lags in their responses, in such

a way that the inferred velocity field is:

$$\Delta v \propto \tau_{XC}^{-1/2}, \quad (3.21)$$

as it would be expected under the gravitational influence of a massive object, lying in the source of ionizing radiation. However, there are also cases, such as the nucleus of Mkn 110, with a detected difference in the lags of the blue and red line wings of the emission lines (see e. g. Kollatschny & Bischoff 2002; Kollatschny 2003), which can be interpreted as the result of a complex BLR structure, that involves an accretion disk, extending far from the central SMBH and originating a wind of line emitting plasma.

Notwithstanding the importance of the previous results, the RM method has several drawbacks, which certainly do not encourage its application. First of all, it is very expensive, in terms of time, since it requires a large number of observations, with good sampling and careful data analysis. On the other hand, its assumptions concerning the variability time scales and the effect of a constant ionizing SED are probably a simplified interpretation of a much more complex situation and there are objects where they certainly do not apply. The line response to a change in the ionizing continuum could be affected by other factors, too, and consequently it would not allow to correctly estimate the size of the BLR by a simple linear relation, like the one in Eq. (3.20). More complex definitions of the BLR radius, based on the emission line responsivity, are possible to account for this effect (e. g. Koratkar & Gaskell 1991; Melnikov & Shevchenko 2008). Finally, it has also been pointed out that the uncertainties related to measurements based on this technique might be very complex to estimate (see, for instance, Gaskell & Peterson 1987; Maoz & Netzer 1989; Edelson & Krolik 1989).

In spite of the difficulties associated to the application of extensive RM campaigns, in more recent years it has been possible to group together the available RM observations, in order to investigate any possible existing relationships of the BLR size with other properties of the source. The comparison of the inferred BLR dimensions with the continuum source luminosity took several authors to conclude that a relation among the BLR size and the

source luminosity could be given in the form of  $R_{BLR} \propto L_{\lambda}^{\alpha}$  (Wandel et al. 1999; Kaspi et al. 2000; Vestergaard 2002, 2004; McLure & Jarvis 2002; Wu et al. 2004; Vestergaard & Peterson 2006), although the exact value of the power law exponent and the actual spectral ranges, where such a relation may hold, are still matter of debate (Kaspi et al. 2005; Bentz et al. 2006; Kaspi et al. 2007; Kelly et al. 2007; Laor 2007; McGill et al. 2008). A simple guess to the dependence of the BLR radius on the luminosity of the ionizing continuum, which appears to be in fairly good agreement with the observations, can be extracted on the basis of some photo-ionization predictions and it provides  $\alpha \simeq 0.5$ . The photo-ionization results are easier to implement for several objects, but they are prone to potentially large uncertainties, due to the need of simplified assumptions, concerning the unknown distribution of the line emitting medium in the BLR. The comparison of this technique with the available RM results, however, may provide the required calibration to handle the problem in such large samples.

### 3.4 Dust Obscuration and Reddening

In many astrophysical environments it is commonly found that the gas is somewhat mixed with a certain amount of dust. As it was discussed in § 1.3.1, there are hints in the typical spectrum of AGN pointing to the presence of dust. This component of the diffuse matter usually contributes to the spectrum, because of its effects of extinction, thermal emission, and light polarization as a consequence of scattering (Barvainis 1987; Sanders et al. 1989; Rudy & Schmidt 1988). Though such signatures can be fairly well identified in the spectra of regions surrounding the AGN (Clavel et al. 1989), the question of dust existing within the BLR and affecting its spectral properties is much more uncertain and there are opposite claims in this sense. One of the most important difficulties, that should be overtaken in order to clarify the role of dust, concerns its physical behaviour in the AGN environment. Dust has been studied to some appreciable detail only within our own Galaxy and

there are no definite arguments, that could support the claim for a generalization of its fundamental properties, such as the chemical composition and the grain structure, in other environments, especially AGN.

Anyways, there are some general properties of dust particles, which provide an useful ground to investigate their role in AGN. At first, we know that dust grains cannot survive at very high temperatures, since they begin to evaporate above  $T \simeq 1700$  K. If we consider a distribution of matter surrounding a bright source of optical and UV radiation of luminosity  $L$  at a distance  $r$ , assuming that the dust absorption coefficient is inversely proportional to the radiation wavelength, the equilibrium temperature of a spherical dust grain would be (Netzer 1990):

$$T_{dust} \simeq 1700 \left( \frac{L}{10^{46} \text{ erg s}^{-1}} \right)^{0.2} \left( \frac{r}{1 \text{ pc}} \right)^{-0.4} \text{ K.} \quad (3.22)$$

Applying the temperature limit, introduced by dust evaporation, it turns out that dust grains cannot survive inside a critical radius  $r_{ev}$ , given by:

$$r_{ev} \simeq \left( \frac{L}{10^{46} \text{ erg s}^{-1}} \right)^{0.5} \text{ pc,} \quad (3.23)$$

which is of the same order of magnitude as the estimated size of the BLR. A consequence of this is that dust cannot exist in the core of AGN unless it is located in shielded regions, where the ionizing continuum of the central source may not directly penetrate. Therefore, the distribution of dust should be similar to that of neutral gas.

The existence of a certain amount of dust within the BLR is actually consistent with the comparison of the typical BLR spectra with some photoionization based models. Indeed, it is sometimes observed that such models show a wavelength dependent discrepancy with observations, which could be very well accounted for by a typical dust extinction effect, which is not included in most calculations. Furthermore, a correction for dust extinction both to the emission lines and the ionizing continuum may result in a better agreement among the global observed distribution of emission line intensity ratios and the SED of ionizing radiation. The same models, however, predict

that the total amount of dust cannot be too large. Otherwise, light scattering by dust grains would significantly increase the escape path length of the line photons originated within the clouds. Such a long escape trajectory would leave almost unaffected the intercombination lines, whose probability to be re-absorbed is very low even at the BLR densities, but the resonance lines would suffer from a considerable decay of the high order transitions, which is not observed in the spectra (Ferland & Netzer 1979; Martin & Ferland 1980; Cota & Ferland 1988). Currently we are almost certain about the presence of dust in the AGN environment, to the extent that the size of the dusty region can be estimated in at least one case, namely the bright Seyfert galaxy Fairall 9. This object is known for its striking decrease in ionizing luminosity, which took its spectrum from a Seyfert 1 classification almost to the Seyfert 2 level (Kollatschny & Fricke 1985). Its IR thermal emission underwent a significant corresponding variation, with a delay which was measured and discussed by Clavel et al. (1989). The inferred circum-nuclear dusty structure is an essential component of the AGN unification schemes based on the idea of an obscured central source. However, at present there is no clear indication of the real effect of dust in the spectrum of AGN. It has been suggested that infrared emission line series, like those of the Paschen series of hydrogen, or some lines, emitted by ions such as He II or O I, might be good indicators of dust reddening in the BLR (see e. g. Ward et al. 1987; Wamsteker et al. 1990; Goodrich 1990), due to the relatively simple transfer calculations. Unfortunately their weakness, combined with the problems of blending among several spectral features sharing the same wavelength ranges, make it extremely difficult to infer meaningful indications. Further understanding the distribution and the spectral properties of dust in AGN is fundamental for the interpretation of the BLR physical properties through the analysis of spectroscopic data, since differential absorption and obscuration by dust may significantly affect the formation of the observed spectra.

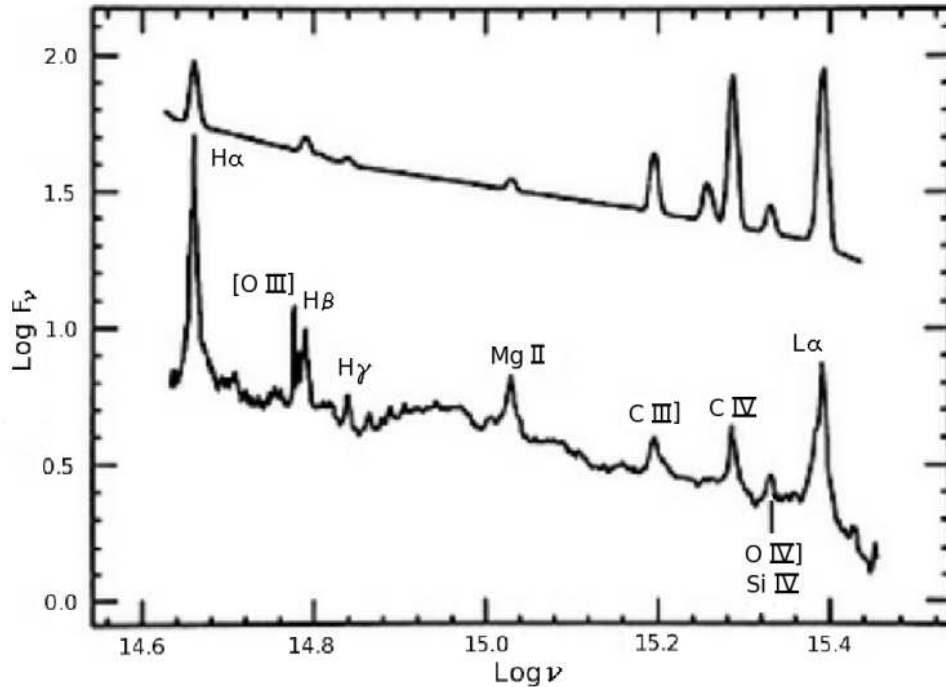


Figure 3.4: Comparison between a composite AGN spectrum (lower line) and a parametric photo-ionization model for the BLR (upper line). The predicted emission lines are given by photo-ionization calculations with the observed continuum and for an assumed BLR structure. Some of the most important emission lines are identified. From Netzer (1990).

## 3.5 BLR Observational Properties

### 3.5.1 Theory and Observations

Combining the results of photo-ionization equilibrium in the BLR plasma with some specific assumptions, concerning its structure, it is possible to predict the properties of the emission line spectrum and to compare them with observations, thus constraining the physics of the BLR. Fig. 3.4 illustrates an example, where a parametric photo-ionization model is compared with an average AGN spectrum. The two are normalized to a common  $L\alpha$  line intensity. Although the overall match between these theoretical predic-

tions and the observations is poor, the relative properties of some emission lines, that can be commonly identified, can be exploited as indicators of the physical conditions, where they are originated.

Usually it is noticed that, due to the relatively simple transfer calculations, the best match among observational data and theoretical predictions is achieved in the case of intercombination lines. The presence of strong resonant lines, in the observations, places a severe constraint on the role played by dust within the BLR. The intensities of such lines is much more difficult to explain, because they are dominated by processes that occur in a very high density plasma and they often involve large and complex transition systems, which are dealt with mainly by means of approximate numerical solutions, rather than with physically grounded calculations. UV resonance lines from heavy elements appear to be very sensitive to the gas temperature and to its ionization (Krolik & Kallman 1988) and models, that achieve good fits in some range of ionization, tend to loose their accuracy elsewhere. An emblematic problem, in this sense, is the difficulty which characterizes the calculation of the hydrogen spectrum. In spite of the simple structure of this element, it is very difficult for theoretical models to explain the observed  $H\alpha$  and  $H\beta$  intensities with respect to  $L\alpha$ . This is largely due to the high density environment, where these emission lines have extreme optical depths, which make the calculation of line transfer somewhat questionable. Similar problems are found in the case of helium lines, for which a large number of energy levels must be taken into account, some of which are very likely to interact with other ion species through fluorescence excitation, or even ionization.

Broad low excitation lines, such as those coming from ions like Mg II, Fe II, and, sometimes, Ca II can be detected in the spectra of many sources (e. g. Ferland & Persson 1989). They are predicted to take origin in a region characterized by low ionization, at very high gas column densities ( $N_{col} \sim 10^{25} \text{ cm}^{-2}$ ), where heating is mainly provided by the absorption of X-ray photons. In particular, the complex electron configuration of the Fe II ion is the source of an extremely crowded emission line spectrum, with thousands of

possible transitions, grouped in some emission bands, which are contributing to a considerable fraction of the total energy that is processed by the BLR. There are several works devoted to the analysis of the Fe II emission lines in AGN (see, for example, Netzer & Wills 1983; Wills et al. 1985; Penston 1987; Joly 1987; Collin-Souffrin et al. 1988b; Dumont & Collin-Souffrin 1990), which are still poorly understood. Their relations with the most energetic fraction of the ionizing radiation field are regarded as a probe of the processes occurring in the closest neighbours of the central black hole (Boller et al. 1996), while the optical blends of this ion have shown light reverberation effects (Kollatschny et al. 2000; Kuehn et al. 2008). On the contrary, very high excitation lines are generally weak, although they are predicted to be a major cooling agent in the innermost regions of an AGN, where only the largest density clouds could be in equilibrium with the intense ionizing radiation field. This suggests that the BLR is unlikely to extend straight to the central engine, but it has some inner radius, where line emission becomes gradually less effective and the plasma essentially reprocesses the spectral continuum (Collin-Souffrin et al. 1988a; Ferland & Rees 1988; Rees et al. 1989).

### 3.5.2 Correlations among the Emission Lines

In view of our understanding of line emission in AGN, the most promising way to identify the main physical processes, occurring in the BLR, is to investigate the relations among several emission lines in large samples. AGN spectra are characterized by a great deal of different behaviours, but the existence of common properties for various objects provides the most convincing evidence of a fundamental underlying physics. Though the field of this study is large, because of the extended frequency ranges, involved in AGN line formation, and much care must be taken in the selection of the objects to be compared, in order to avoid artefacts in the conclusions, robust results are likely to come from a similar analysis.

Looking simply at the properties of the broad emission lines, it is very

difficult to identify generalized trends of reasonable statistical significance. There are suggestions that some particular line ratios, such as, for example  $C\text{ IV } \lambda 1549 / L\alpha$  or  $C\text{ III] } \lambda 1909 / C\text{ IV } \lambda 1549$ , evolve as a function of luminosity, indicating, perhaps, a change in the ionization parameter of the sources, according to their luminosity. The real meaning of such a change, however, remains unclear, since it is hard to discriminate whether it occurs for an increased gas density, a different ionizing SED or a change in the optical depth of the clouds. The observed scatter in most of such relations argues in favour of a substantial combination of several of these effects. A more interesting observation, instead, comes from the comparison of spectral features coming from both the BLR and the NLR. Boroson & Green (1992) investigated the correlation matrix of several properties in the spectrum of many AGN, finding that the most remarkable eigenvector, that could be inferred, implied an anti-correlation among the strength of the Fe II blends and the narrow [O III] emission lines at 4959Å and 5007Å. This property, dubbed the *Boroson & Green Eigenvector 1*, is associated with other minor trends in the profile of the  $H\beta$  emission line. A complete explanation of the physical processes, affecting both the BLR and NLR environments, has not yet been provided. In particular, it is very hard to explain how the luminosity of very extended ionized regions, which should radiate their light almost isotropically, can be related to the brightness of a much more compact source, whose light can only be seen from a restricted range of directions and with a variable amount of extinction (Kuraszkiewicz et al. 2000). It is argued that, due to the purported tight relation among the strength of the Fe II blends and the intrinsic X-ray continuum of the source, the origin of the Eigenvector 1 could be related to some details of the accretion process onto the central SMBH (e. g. Sulentic et al. 2000b; Marziani et al. 2001; Sulentic et al. 2003; Marziani et al. 2003; Sulentic et al. 2007). The Eigenvector 1 could be explained if very hard ionizing radiation, producing strong Fe II emission lines, is less effective in the ionization of the extended NLR. This is actually possible if, for example, hard ionizing radiation is more common in

faint sources, but the reasons for such a mechanism, though attractive, can be very different.

### 3.5.3 Correlations among Lines and Continuum

The relations among the ionizing continuum in the spectra of AGN and the lines, subsequently emitted by the BLR, have been thoroughly analyzed under many different aspects. Although strong correlations among the amount of energy radiated in the continuum and in the lines can be detected, it is found that the emission line profiles and the source luminosities are not significantly related. Since the line profiles track the gas kinematics, while the luminosity measures the power of the central source, which is essentially controlled by the mass of the SMBH and by its accretion rate, it turns out either that AGN can result from various and extreme combinations of such parameters, or that other effects must be taken into account, in order to give a correct interpretation of the observed spectral properties. One of the most intriguing possibilities invokes the role of BLR geometry, a crucial element in our understanding of AGN spectra and of the physics behind them.

There are several arguments suggesting that geometry is important in AGN. Since our measurements of the BLR velocity field can only explore the projection of the motion pattern along our line of sight, our ability to infer the dynamics of gas relies on our guess to the actual distribution of the gas. The physics of matter accretion onto compact massive objects predicts that the accretion flows are likely to form disks (Frank et al. 2002), but the calculation of the corresponding spectra, when disks are powered by black holes, is very complex and we still lack of any definite expectation about possible disk signatures. A disk, seen close to edge-on by an observer, clearly emits broader spectral features than another, oriented in a face-on position, because the projection of the disk rotational velocities on the observer's line of sight would be much larger in the former case, rather than in the latter. The interpretation of line widths in terms of disk inclination is supported, at least partially, by radio observations of some AGN, where the ratio among

the brightness of the compact source, corresponding to the source of ionizing radiation, and that of the surrounding halo decreases, when the emission line widths increase. Since the extended radio halo is supposed to emit its radiation almost isotropically, while the signal of the compact source is highly beamed, probably in the direction of the rotation axis of the plasma, it is found that sources, where the rotation plane is closer to the face-on position, actually have narrower emission lines (Wills & Browne 1986).

Another important property, relating some emission lines to the spectral AGN continuum, was observed by Baldwin (1977) in the C IV  $\lambda 1549$  line and later confirmed by other studies (Osmer & Smith 1980; Wampler et al. 1984; Baldwin et al. 1989; Kinney et al. 1990). In this case, it was noticed that many emission lines are strongly correlated with the luminosity of the AGN continuum, but the relationship does not appear to be exactly linear, as the emission line intensities do not increase as the spectral continuum does. Expressing the line strength in terms of *Equivalent Width* (EW), a measure defined as the width of a hypothetical spectral feature, having the same intensity of the continuum next to an emission line and the flux of that line, the Baldwin relationship is an anti-correlation among the continuum luminosity and the emission line EW. This relation can be detected both in a large sample of sources observed at a single epoch, in which case it is called *Global Baldwin Effect*, as well as in a comparison of several spectra of the same variable object (Wamsteker & Collina 1986; Kinney et al. 1990; Edelson et al. 1990) and it is called *Intrinsic Baldwin Effect*. The reasons for giving rise to intrinsic and global Baldwin effects need not to be exactly the same. Actually, some emission lines can be affected by the global effect and not by the intrinsic one. The opposite might be true, as well. Among the possible processes, which have been invoked as an explanation of the Baldwin effect, it was suggested that variability in the ionizing continuum and the emission lines could imply some changes in the physical properties of the BLR plasma, affecting its ionization parameter and its covering factor in such a way to produce different line responses to the various continuum strengths (Murdoch

1983; Mushotzky & Ferland 1984; Korista & Goad 2004, 2005). Finally, it has also been argued that a good agreement with the observations might be carried out by theoretical BLR models, including thin accretion disks in their continuum sources (Netzer 1985). On the basis of some arguments about the aspect dependent ratio, between the power of the emission lines and of the nearby AGN continuum, which are very similar to the case of radio observations, it is argued that the probability distribution of disk inclinations would be consistent with a global Baldwin effect in some of the strongest broad emission lines.

### 3.6 Probing the BLR

At present a great deal of efforts have been spent, in order to investigate the physics of the BLR, with particular care to the identification of its structure and dynamics. Many advanced spectroscopic techniques are now starting to provide useful constraints to the properties of the broad line emitting gas and, therefore, to achieve a better understanding of its interactions with the central engine, whose nature is still one of the most fascinating fields of research in modern Astrophysics. The large amount of data, which are now provided by extended surveys and detailed observations, can be interpreted in the framework of more and more realistic models, giving us good chances to shed some light on the problems that cannot yet be solved by direct observations, and that will probably persist in the near future.

The spirit of this work is to exploit some of the widely available data, provided by recent and ambitious survey programs, in order to search for properties, predicted by different theoretical models, which may help us to clarify some of the unknown physics in the BLR of various AGN. With this purpose in mind, we collect a sample of sources, investigating mainly the optical range of their spectra and studying the relations of the Balmer series of hydrogen emission lines with other available observations in the selected objects. We compare the results of our measurements with the theoretic-

cal predictions of different interpretations, concerning the influence that the central engine has on the BLR structure. We check for consistency with the results of other research programs and, when possible, by testing our expectations with further observations, collected in other spectral ranges. The methods that we will apply are somewhat already known to Astrophysics, but their use in the field of AGN research has only recently become possible. Thanks to the possibility to access the available public data archives, whose contribution to the development of our knowledge will undoubtedly be unprecedented, we are now able to apply powerful investigation techniques onto very large samples.

# Chapter 4

## Sample Collection and Data Reduction

### 4.1 Introduction

The purpose of our investigation is to explore the physical properties of the BLR in active galaxies, through an analysis of spectroscopic data collected in the optical frequency range of their signal. Our choice to restrict this study mainly to the optical domain of the electro-magnetic spectrum, with a particular care to the Balmer series of hydrogen, descends from the requirement to study a large sample of objects, while reducing as much as possible the influence of the most commonly encountered selection effects. Indeed, extensive observations of specific objects in several spectral ranges are more often available for peculiar, or at least very bright sources, which could not be able to represent a wider population appropriately. On the contrary, large survey programs, mainly undertaken by ground based instruments, provide the required amount of uniform data, which we need to build our sample in a meaningful way. This kind of observational programs is now starting to produce good quality spectra of many objects at a relatively low redshift, where the most easily observed signals fall in the optical and in the near UV spectral windows.

The rest frame optical and UV radiation of AGN carries a huge amount of information concerning the physics of the central engine, both in the spectral continuum and in the emission lines. The relationships existing among several lines and the observed continuum are an effective probe of that considerable part of the high energy spectrum, which is at the origin of many AGN observational properties, but it is very difficult to observe, because it is typically absorbed and reprocessed very close to its own source. A detailed study of a group of emission lines, originated by the same transition series, like in the case of the Balmer lines, is, thus, a desirable way to test the underlying physics of AGN theory and to improve our ability to explain the BLR properties.

In the previous chapters we shortly summarized how the interaction of an ionizing continuum with an astrophysical plasma results in the emission of some characteristic spectra, which can be exploited to investigate the physical conditions of the environments where they are produced. We subsequently turned our attention to the properties of the BLR, bringing together some of the most important results, that spectroscopic analyses could achieve, both with classical methods and with more advanced techniques. Here we focus our discussion onto the selection of the data sample, that we study in this work, describing the techniques which we adopted to prepare our data for subsequent analysis. We start from a discussion of the main features of astrophysical data archive of the *Sloan Digital Sky Survey* (SDSS), then we present the typical source candidates extracted with our criteria from the available database. We finally describe our sample and the development of the reduction procedures, which we exploited on it.

## 4.2 The SDSS Program

### 4.2.1 Telescope and Instrumentation

The SDSS is currently the largest existing archive of uniformly collected spectro-photometric observations of the sky. The aim of this ambitious pro-

gram is to map a wide area of the sky, corresponding approximately to one fourth of the celestial sphere, with the information recorded by a specific instrumental configuration. At the time of writing, the main goal of the project, the *SDSS Legacy Survey*, has been completed with the publication of the 7<sup>th</sup> data release in the on-line archive, which covers more than 8000 square degrees of observed sky, with the detection of 230 million celestial objects and the classification of more than one million of spectra.<sup>1</sup> The successful solution of the SDSS program, with its huge impact on the current and near future research, encouraged the extension of the survey towards more specific projects, aiming at the construction of particular data sets, such as the *Sloan Extension for Galactic Understanding and Exploration* (SEGUE), devoted to the study of the structure and history of the Milky Way, or the *Sloan Supernova Survey*, watching through the Universe for the occurrence of Supernova Ia events and for their fundamental contribution in the development of Cosmology.

The SDSS program takes advantage from the use of a dedicated telescope, operating at the Apache Point Observatory in New Mexico (USA). The telescope is a 2.5 m  $f/5$  modified Ritchey-Chretien instrument, mounted in the altitude - azimuth configuration, with a 1.08 m secondary mirror and a system of corrector lenses, yielding a 3° distortion-free field of view. Its focal plane is equipped with advanced instrumentation for photometric, astrometric, and spectroscopic measurements. The imaging camera exploits an array of 30 SITe/Tektronix 2048x2048 pixel CCD, arranged in columns of five CCD working with specific photometric filters (a detailed description is given by Gunn et al. 1998 and York et al. 2000), while the telescope performs a drift scan of the sky. The telescope's motion forces the image of each object in the field of view to drift across the whole array of filters and each scan is performed twice, with slight pointing offsets, allowing for the correction of

---

<sup>1</sup>The website of the SDSS is <http://www.sdss.org> and it provides online material including full access to the database, lists of publications, technical details, and several useful tools for research at any level.

Table 4.1: SDSS Spectrograph Configuration Summary

CCD	4 x SITe/Tektronix 2048x2048, 49.2 mm <sup>2</sup>
Channels	3800 Å - 6150 Å (blue); 5800 Å - 9200 Å (red)
Fibre Number	2 x 320
Fibre Diameter	3"
Pixel Size	69 km s <sup>-1</sup>
Spectral Resolution	Ranging from 1850 to 2200

the blind gaps in the sensor, due to the edges of the multiple CCD. Other 24 CCD, covered by neutral density filters, are placed before and after the photometric array to collect astrometric data. Spectroscopic observations, instead, are recorded by two spectrographs, each one with a blue and a red channel, separated by dichroic filters. Light from the observed sources is conveyed to the spectrographs by a system of 640 optical fibres, covering a field of view of 3" each, and it is recorded by a total of four additional CCD. A separate telescope of smaller aperture is completely devoted to the observation of standard stars, to provide data for the photometric calibration of the science material at the same time of observation. The SDSS instrumentation, working at full efficiency, stores more than 2 GB of scientific material per operating night.

### 4.2.2 Spectroscopic Data Products

With the available instrumentation, it takes about 15 minutes for the SDSS to record a spectroscopic exposure, having a good confidential signal to noise ratio ( $S / N$ ) down to appreciably faint magnitudes. The optical fibres, which collect light at the telescope's focal plane, convey the signal from different areas of the field of view into both the channels of the two spectrographs, in such a way that every exposure produces 640 spectra, most of which can be ascribed to specific sources. In Table 4.1 we give a summary of the

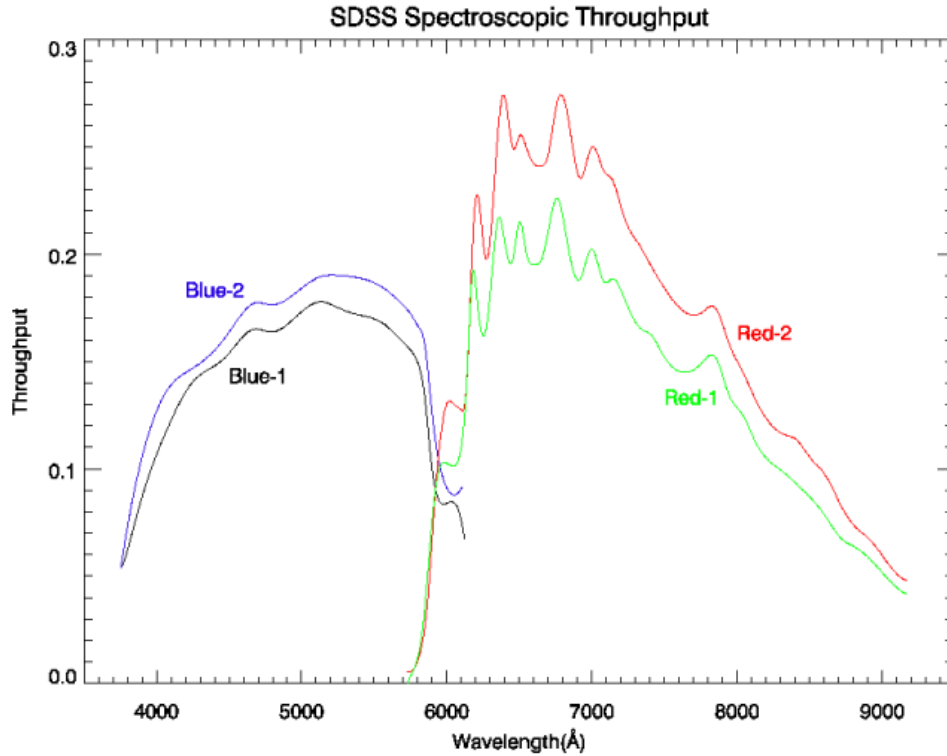


Figure 4.1: Spectroscopic throughput of the SDSS instrumental configuration with respect to the total amount of incident radiation (the plot is taken from the SDSS web site).

fundamental features of the SDSS spectrographic set up, while in Fig. 4.1 we report the instrumental throughput of the two spectrographs at various wavelengths.

One of the major advantages of the SDSS data product is that the scientific material is directly calibrated in physical units, though the raw observations are made available, as well. The wavelength calibration is provided through comparison spectra, produced by means of Hg, Cd, and Ne arc lamps, with an estimated rms error of 0.07 pixels, corresponding to approximately  $10 \text{ km s}^{-1}$ . The calibration in flux, instead, is performed in comparison with standard stars observed at the same time of the involved spectra. The whole calibration procedure is undertaken by the standard

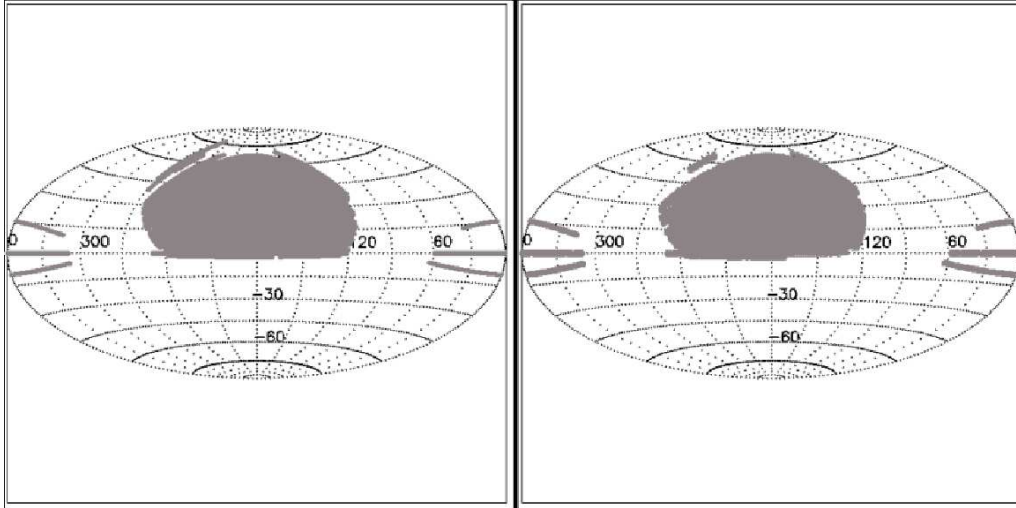


Figure 4.2: SDSS observational sky coverage after the 7<sup>th</sup> data release. The shaded regions represent the fractions of sky observed by the SDSS telescope. The imaging survey is illustrated in the left panel, while the spectroscopic survey is represented in the right panel.

project pipelines, which subsequently store a huge amount of material, ready for scientific investigation.

### 4.2.3 The SDSS Online Data Archive

As it was previously mentioned, the SDSS holds observations of a huge number of celestial bodies, detected on a large fraction of the sky. Fig. 4.2 illustrates the sky coverage of the imaging and spectroscopic surveys, achieved with the 7<sup>th</sup> data release of the SDSS. Searching the complete database for specific targets, in such conditions, is not a trivial task and it requires the implementation of effective tools, that allow the interested users to access the data they are actually seeking for. All the images and spectra collected by the SDSS telescope are stored in the `fits` file format, which, together with the data themselves, includes detailed information about the instrumental set up and the target location. Such indications are used by the data retrieval services to access the archive in the form of selective queries.

There are several ways in which the user can handle the available tools, in order to customize the resulting query and to identify the most useful data. The SDSS adopts a schematic nomenclature system, for the available observations, which is quickly translated by the Object Cross-Identification tools into astronomical coordinates. The Catalog Archive Server (CAS), furthermore, is capable of selecting the objects, according to their position in the sky, and to introduce several additional criteria, mainly based on spectral and photometric properties, thus applying an effective filter on the range of valuable candidates. The user is able to control the quality of data through a quick preview system, then the scientific material is available at the Data Archive Server (DAS). Thanks to the large number of possible selection criteria and to its extended sky coverage, the SDSS data archive can be effectively exploited, together with other existing catalogues, to collect statistically significant samples of objects with appreciably good observational material.

### 4.3 Sample Collection

The main goals of our project are to investigate the thermodynamical properties of the BLR plasma and to study its kinematics through an analysis of the Balmer emission line series. Combining the results of such work, we try to understand the dynamical influence of the central engine onto the surrounding regions and, thus, to reveal some specific details of the physics of AGN. We handled this problem during a three year long research program, selecting two data samples, among the available archives, with slightly different requirements. We analyzed our data to investigate the desired BLR properties and, subsequently, we combined our results together, applying uniform measurements to the common properties of the whole sample. We finally compared our findings with the expectations, concerning other spectral properties of the sources, coming from our interpretation of AGN.

Our first data sample was collected at the spectral database of the 3<sup>rd</sup> data release from the SDSS (Abazajian et al. 2006). According to the purposes of

our work, we searched the SDSS database for sources corresponding to the following requirements:

- objects had to be located at redshift  $z < 0.4$ , in particular it was required that the entire profiles of lines belonging to the Balmer series were covered by the available spectral range;
- only spectra where the Balmer series was clearly recognized, at least up to the  $H\delta$  emission line, were considered;
- the profile of a broad component had to be detectable for each Balmer line;
- such profiles had not to be affected by distortions, due, for example, to bad pixels on the sensors, as well as by the presence of strong foreground or background sources.

The preview spectra provided by the database retrieval software were manually inspected, looking for the objects in better agreement with our requirements, until a number of 115 sources were chosen from approximately 600 candidates, examined in various survey areas. Subsequent inspection of the spectra collected within the database led to the rejection of 25 objects, which were affected by problems that could not be detected in the preview analysis. Therefore the resulting sample included the spectra of 90 variously broad line emitting AGN, corresponding to  $\sim 15\%$  of the candidates that we examined. A significant fraction of this sub-sample (45 spectra) belongs to the collection of sources studied by Boroson (2003).

The investigation of BLR kinematics from the Balmer line profiles further required a homogeneous sample of AGN optical spectra, featuring prominent broad Balmer emission line components. The publication of the 6<sup>th</sup> data release (DR6) in the SDSS spectroscopic database provided a huge number of objects, that could be introduced to update the existing sample (Adelman-McCarthy et al. 2008). In order to collect a set of good signal spectra, we chose to select our candidates in the Véron-Cetty catalogue of Quasars and

Active Galactic Nuclei (12<sup>th</sup> Ed.) (Véron-Cetty & Véron 2006), with the following requirements:

- the object redshift had not to exceed the limit  $z = 0.8$ , because objects at larger redshift have their H $\beta$  emission line beyond the SDSS spectral coverage;
- only bright sources, with  $M_V < -23$ , were considered;
- each object had a spectral classification suggesting the presence of broad emission line components.

On the resulting candidate list, we applied further constraints, that restricted the sample to the most appropriate sources. In particular we chose objects whose spectra had at least three clearly detectable broad Balmer lines and they were not affected by instrumental disturbances or by strong foreground and background contamination. We ended up with a set of 40 additional objects, which complete the list that is described in Table 4.2. Our sample, therefore, features 130 objects located in the redshift range  $0.024 \leq z \leq 0.644$ , with an average redshift of 0.188.

## 4.4 Preliminary Spectral Reduction

Since the SDSS database provides users with pre-processed material, spectra retrieved from the survey are already corrected for instrumental and environmental effects, including the sky emission subtraction and the correction for telluric absorptions. Calibration of data in physical units of flux and wavelength is also performed. Consequently, our preliminary reduction simply needs to take into account a correction for Galactic Extinction and the removal of cosmological redshift. We estimated the effects of absorption in the interstellar medium of the Milky Way using an empirical selective extinction function (see Cardelli et al. 1989), that was computed for each spectrum on the basis of the Galactic Extinction coefficients given by Schlegel et al.

(1998) and available at the *NASA Extragalactic Database (NED)*<sup>2</sup>. After the correction for interstellar absorption within our Galaxy, we took the AGN spectra to the rest frame of their narrow emission lines, thus removing the effect of cosmological redshift.

The spectra so far elaborated still carried a large amount of contaminations, overlapping with the actual BLR signal, which we are interested on. Before we could be able to estimate the properties of the broad line emitting gas, we had to distinguish the contribution of the NLR, that of the host galaxy star light, and to take properly into account the role of the different spectral features, which are blended together even in the BLR spectrum alone.

#### 4.4.1 Host galaxy correction

Light from targets observed by the SDSS spectrographs is collected within sky areas of fixed aperture, which, in the case of AGN, will bring to various contributions from the host galaxy to the total flux recorded by instruments, essentially depending on the object redshift and on the relative importance of the host with respect to its AGN. Although this effect does not significantly influence the properties of the broad emission lines, where the contribution of the host galaxy is completely negligible, the stellar continuum radiation might represent a considerable fraction of the observed continuum and, thus, affect our estimate of the actual AGN luminosity.

A possible way to account for the influence of host galaxies on the formation of the resulting spectra is the one proposed by Vanden Berk et al. (2006) on the basis of the *Karhunen-Loève Transforms*, described in Connolly et al. (1995). This technique assumes that the total spectrum of an AGN and of its host galaxy can be regarded as the result of a sum of orthonormal components, originated independently by the AGN and the host galaxy. The fundamental components, also called *eigenspectra*, are then arranged together

---

<sup>2</sup>The Galactic Extinction coefficients are provided at <http://nedwww.ipac.caltech.edu/>

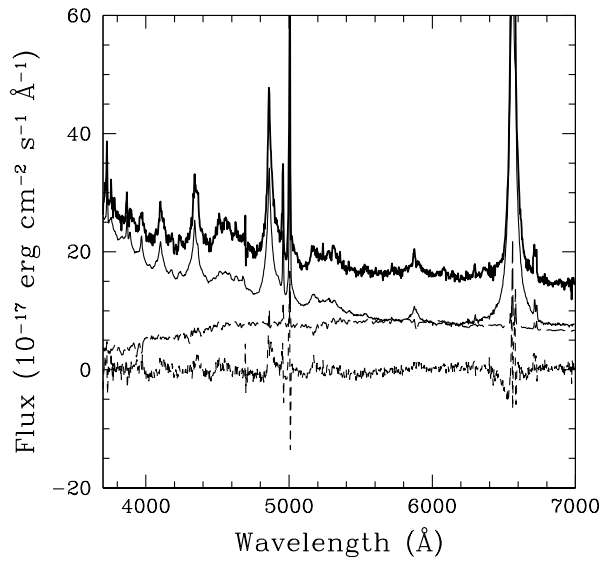


Figure 4.3: Spectral decomposition of 2MASX J10570691–0041446. In this plot we show the spectrum of the object in the rest frame wavelength range used to perform the fit (thick continuous line), the AGN component (thin continuous line), the host galaxy contribution (long dashed line), and the fit residuals (short dashed line).

in a linear combination, which forms the cumulative spectrum:

$$S(\lambda) = \sum_{i=1}^n [q_i \cdot Q_i(\lambda)] + \sum_{j=1}^m [g_j \cdot G_j(\lambda)], \quad (4.1)$$

with  $S(\lambda)$  being the total spectrum,  $Q_i(\lambda)$  the  $i^{\text{th}}$  AGN component, weighted by its coefficient  $q_i$ , and  $G_j(\lambda)$  the  $j^{\text{th}}$  host galaxy eigenspectrum associated to the corresponding coefficient  $g_j$ . Given an appropriate base of eigenspectra, representing the principal components produced by the AGN and those coming from its host, it is possible to compute the wavelength independent weight coefficients  $q_i$  and  $g_j$  which provide the best fit to  $S(\lambda)$ . The set of eigenspectra, computed by Yip et al. (2004a, b) from large samples of galaxy and AGN spectra, provides the appropriate set of principal components to

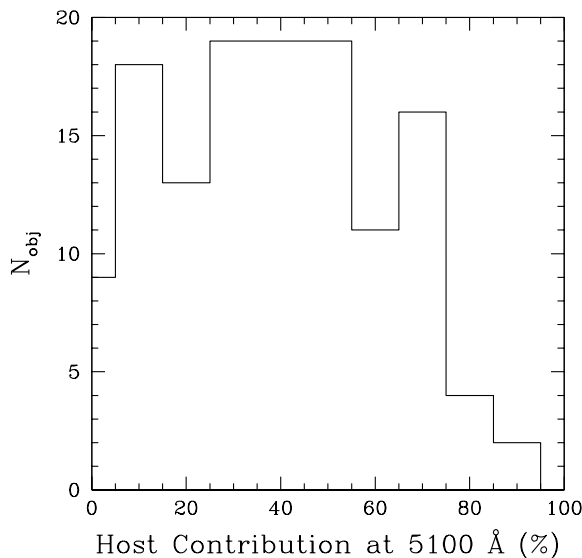


Figure 4.4: Relative contribution of the host galaxy component to the optical continuum of the sources in our sample. The amount of light contamination from the host does not correlate with redshift or luminosity, suggesting that these effects are probably balanced.

carry out the separation outlined in Eq. (4.1). We used an iterative  $\chi^2$  minimization process, which was run over the rest frame wavelengths covering the range from 3700 Å to 7000 Å, to assign the appropriate eigencoefficient values for the decomposition of our spectra. In a similar analysis to the one performed by Vanden Berk et al. (2006), we found that most of the variations within our sample could be accounted for by introducing five galaxy and six AGN components, because a smaller number of eigenspectra left very large residuals, while a larger number took to the danger of noise fluctuation overfitting. The decomposition of our spectra usually yielded a reduced residual of  $0.05 < \chi^2 < 2$  in the continuum. As we show in Fig. 4.3, where we give an example of the spectral decomposition, obtained by combining separately all the AGN and host components, this method is actually able to fit the spec-

tral continuum in good detail, although significant residuals are left in the regions corresponding to the line cores, where the highest order variations of our sample are carried out. The spectral contributions identified as being due to the host were subsequently removed from the observed spectra and they were used to estimate the relative contributions of the AGN and their hosts to the observed luminosities. Fig. 4.4 illustrates the amount of host galaxy contaminations detected in our sample in the form of a histogram. Studying the distribution of these non-AGN components, we found no clear evidence for a redshift or luminosity dependence. Indeed, taking into account objects at larger distances, there is a higher probability to include more powerful AGN and this may balance the effect of light collected from a wider fraction of the host.

#### 4.4.2 Identification of the BLR Spectral Component

Since our interest lies on the investigation of the BLR properties, we had to identify the broad line components in the spectra. In principle, the BLR signature can be isolated if we know which contributions are introduced by the underlying continuum of both the AGN and its host and by the NLR. In many cases large data samples are dealt with by means of automatic processing techniques, which can be particularly useful in a statistical sense, but they neglect most of the peculiar properties of the single sources. In our case, intrinsic differences among the various objects certainly did not simplify the task. Broad and narrow lines, indeed, usually have blended profiles, whose final shape may critically depend on many circumstances, such as the orientation of our line of sight onto the source, the presence of absorbing material, or the amount of signal originating outside the source itself. For this reason we undertook the task of manually identifying the BLR contributions in spectra, rather than relying on automatically collected determinations. We used the *IRAF* software package for reduction and analysis of astrophysical material to study our data. At first, we performed a continuum subtraction, fitting the underlying continuum shape of each spectrum in the rest frame

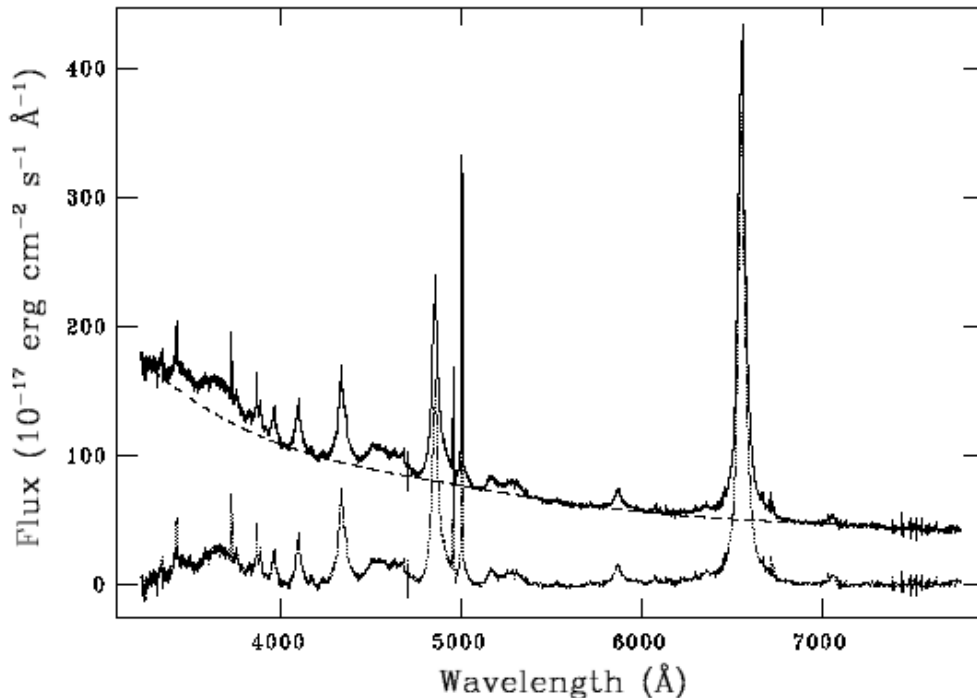


Figure 4.5: Example of continuum radiation subtraction in the spectrum of 2MASS J03221390+0055134. The observed spectrum (thin continuous line) is compared with a `spline` function reproducing the underlying continuum (dashed line). The dotted line in the bottom part of the diagram illustrates the spectrum after continuum subtraction.

wavelength ranges that were not affected by significant line contamination. The shape of the spectral continuum was reproduced by means of `spline` functions, with order ranging from 3 to 7 in the `splot` task of *IRAF*. An example of this method is plotted in Fig. 4.5, where we illustrate the original spectrum of 2MASS J03221390+0055134, compared with the estimated underlying continuum. The resulting continuum subtracted spectrum is drawn in the bottom part of the diagram.

Measuring the properties of the broad lines is often complicated by the multiple spectral features that are blended together. In the case of the Balmer

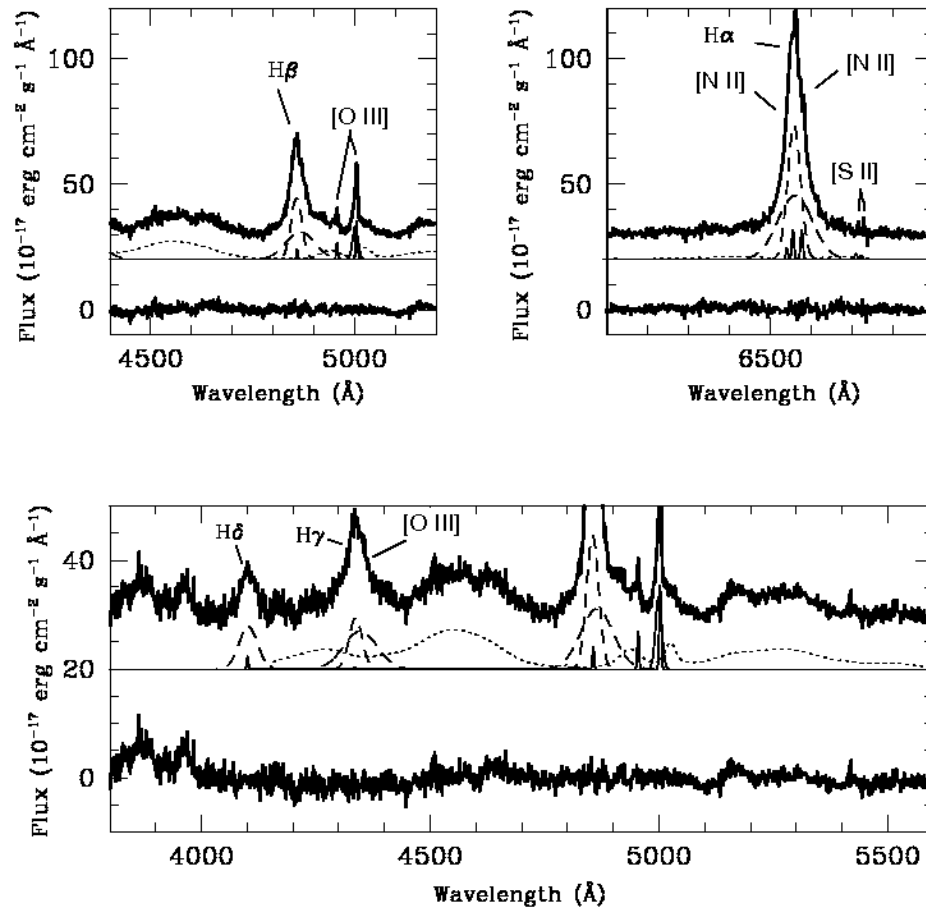


Figure 4.6: Multiple Gaussian decomposition of the Balmer emission line profiles in the spectrum of PC 1014+4717. Using the narrow [O III] emission line at 5007  $\text{\AA}$  as a template for the forbidden lines, we fit the observed spectrum (thick continuous lines in the upper regions of the plots) with a NLR component (thin continuous line), two broad line contributions (long dashed lines), and an appropriately scaled Fe II spectrum (dotted line). The thick continuous lines in the bottom part of the diagram are the fit residuals.

series, narrow lines from [O III], [N II], [S II], together with the narrow Balmer emissions, have to be taken into account, while blends with broad lines from He II and the multiplets of Fe II can heavily affect the observed profiles. As we show in Fig. 4.6, we performed the subtraction of the narrow line components by means of multiple Gaussian fits to their profiles. Using the narrow [O III] feature at 5007Å, we extracted a template profile for forbidden lines in each spectrum and the other narrow lines were required to have compatible widths. The line intensity ratio for the [N II] doublet at  $\lambda\lambda$  6548, 6584 has been fixed to 1 : 3. In a certain number of cases, before proceeding with our measurements of fluxes and profiles, we had to remove the contribution due to the Fe II multiplets. Following the method suggested by Véron-Cetty et al. (2004), it is possible to remove the Fe II contribution from spectra by scaling and broadening an appropriate template, estimated from the spectrum of an AGN featuring prominent Fe II emission lines. In our work, we used the Fe II template spectrum coming from *I Zwicky 1* (Botte et al. 2004), splitting it into two parts, which we scaled in order to achieve a better coincidence with our data.

## 4.5 Programming Language Implementation

So far we described the main guidelines of the techniques we employed in the preliminary data reduction of our sample. With the exception of the correction for the host galaxy contamination in the SDSS spectra, all the elaboration exploited some standard procedures, which are provided by the available software packages, such as *IRAF*. However, many steps of the spectral reduction procedures need the data to be put in an appropriate format, which, sometimes, does not match the output of the previous step. Although this process often involves only quite simple calculations and conversions, the size of our sample is such that an automatic management of these operations is highly desirable. Moreover, the implementation of the host galaxy spectral decomposition, which is not yet available as a standard procedure, required

the introduction of more advanced computational capabilities.

Among the possible solutions, we chose to build our own procedures using the C++ programming language. As an object oriented language, with a combination of powerful low level control routines and more user-friendly functions, C++ has a wide set of advantages over other possibilities, when it is used to build new applications. C++ compilers are widely distributed and portable. They follow a well defined standard (see e. g. Becker 2008 and references therein), which is a built-in feature of some of the most common computer operating systems, and they provide the possibility to access many libraries of specific functions, or even to build personal ones, according to convenience. Without descending into the details of program coding, we summarize here some of the main features offered by this language, with a discussion of their relation with our particular requirements.

### 4.5.1 Dynamic Memory Access

In order to execute calculations with data, our programs must store a certain amount of information in the computer's memory. The simplest way to record the interesting values, such as input data, partial results, and final output, involves the use of *variables*, which are, essentially, fixed memory records of pre-assigned size and location. When a variable is declared, the computer associates it with a specific memory record, whose size is determined on the basis of the information that the user plans to store. As long as the variable exists, each reference to its name forces the computer to access that memory record, performing the required operations with the value stored therein.

The most important limit of variables is that the amount of memory, which the computer will preserve for the subsequent elaboration, is specified at the time of code writing, or, in some cases, in the first operations following the code execution. This means that a code based on variables is not particularly suitable to handle different amounts of input material, because the available memory could be exhausted or wasted, leading to the danger of running wrong calculations. Instead of writing down a code that should be

modified according to the amount of data, which we are going to examine, C++ offers the possibility to handle the computer's memory dynamically, meaning that the code is able to estimate how much memory it needs to perform its calculations and, thus, to prepare the appropriate amount of records and to free the corresponding memory again, once it is no longer needed.

Dynamic memory management occurs through the use of *pointers*, a special kind of variables which, instead of recording a value, store the memory addresses where the values are recorded. Once the size of the data record is given, pointers can be used to build structures of adjacent records, so that the code is able to access the required value simply by stepping from one memory record to the following. In this way, the gathering of input information does not involve the declaration of variables, so that the code can collect an arbitrary number of input data, simply by creating each time a new record in the structure. The only limit is induced by the amount of memory which is physically available. This kind of approach is fundamental for applications which have to access different subsamples of our data with large memory requirements.

### 4.5.2 Data Format Control

Once the calculation of some particular reduction procedure is over, the results are put into hard copies, in the form of machine readable tables. Depending on the specific procedure that was applied, the format of such tables may change and it may also include additional information, concerning, for example, the data reduction history, which might be not accepted by subsequent programs. When two following operations can be handled by means of software tasks, that are both implemented in the same wider package, like it happens in the *IRAF* environment, this problem is unlikely to occur. But, if some of the calculations need to be run outside the environment, all the information written in the files must be translated, according to the operations we are going to perform.

In C++ it is possible to access the information stored within files, oper-

ating with many different data formats, or even specifying new customizable ones. Exploiting the controls provided by the basilar input and output functions of this language, the code can be able to search for the desired information in a large variety of data structures and to create formatted tables, matching the requirements of most of the standard procedures involved in our reduction process. With the amount of material, which we must take into account during the reduction of our spectra, the ability to perform conversions and other calculations by means of quick and simple interface applications is a fundamental aspect of the project.

### 4.5.3 Object Oriented Programming

All the advantages offered by the C++ language, in terms of dynamic memory management and data format control, can be optimized through the introduction of the so called *classes*, which are the characteristic property of object oriented programming languages. A class is an extension of the simple concept of data structure, which, together with the information actually describing the data, can also include instructions to process them in some specific operations, defined by the user. It is, therefore, an independent element of code, used to organize data according to the desired logical criteria, that can be invoked anywhere else in the code, providing a quick and selective access to the data and to their elaboration at once. Conceptually, the purpose to store arbitrary amounts of data and to define the operations to be performed on them can be achieved by linear program coding, as well, but the final structure of the program becomes very complex, because data structures and processing functions are treated as distinct entities and their interactions affect the overall performance of the code at the time of execution. In general, the use of classes greatly enhances the structure and performances of programs devoted to the elaboration of large data sets. Because they are independent from the structure of the programs that interact with them, the instructions written in a class are immediately available for applications, designed to run the elaboration described in that class, without

the need to be specified again.

The blocks of memory, declared in the form of a class, take the name of *objects*. As it happened in the case of the data structures created with pointers, all the information belonging to an object has a specific location in the memory, but the chance to gain access to the data is ruled by the procedures defined by the class. This limitation forces the programs, that use some classes, to adopt the data format defined by these classes, thus providing a further warranty on the communications among different applications. Using objects created by specific classes, for instance, to represent the spectra of our sources in the computer memory, is a convenient way to perform complex calculations in a fairly simple manner. The most representative example is the computation of the host galaxy correction, which requires the computer to fit the observed spectrum as a linear combination of synthetic components coming from the host galaxy and from its active nucleus. Each one of these spectra consists of several data points, representing the radiation wavelength and the corresponding specific flux. Computing the best linear combination of such spectra would, therefore, involve the declaration of large variable arrays to represent them, or, alternatively, the definition of an appropriate class, representing the spectrum, and the declaration of a small number of objects from that class. Using the object oriented method, instead of the first procedure, reduces the amount of work undertaken by the programmer, because, though the calculations still involve all the available data, in this case the organization of input values in the appropriate blocks of memory is automatically managed by the computer itself.

Table 4.2: Sample of Objects Selected from the SDSS Online Archive

Object Name	R. A. (hh:mm:ss.ss)	Dec. (dd:mm:ss.s)	V (mag)	$z$	Detected in Radio
LBQS 0010+0035	00:13:27.31	+00:52:32.0	17.80	0.363	No
2MASX J00133540-0951213	00:13:35.38	-09:51:20.9	17.23	0.060	No
2MASS J00372354+0008122	00:37:23.49	+00:08:12.5	18.53	0.252	No
2MASX J00423686-1049222	00:42:36.86	-10:49:21.8	15.73	0.041	No
SDSS J010712.03+140844.9	01:07:12.03	+14:08:44.9	19.13	0.077	No
2MASX J01100897-1008434	01:10:09.01	-10:08:43.4	17.94	0.050	No
2MASSI J0112549+000313	01:12:54.92	+00:03:13.0	17.35	0.235	No
SDSS J011703.58+000027.4	01:17:03.58	+00:00:27.3	15.90	0.046	Yes
QSO B0119-013	01:21:59.82	-01:02:24.3	15.17	0.054	Yes
2MASX J01352783-0044477	01:35:27.84	-00:44:47.9	18.41	0.080	No
QSO B0137-010	01:40:17.07	-00:50:03.0	15.86	0.334	No
2MASX J01423843+0005145	01:42:38.47	+00:05:14.8	18.45	0.146	No
2MASX J01424828-1008402	01:42:48.30	-10:08:40.1	17.60	0.090	No
SDSS J015046.68+132359.9	01:50:46.68	+13:23:59.9	19.20	0.094	No
2MASX J01591007+0105148	01:59:10.04	+01:05:14.6	16.18	0.217	No
2MASS J02333539-0107446	02:33:35.37	-01:07:44.6	17.94	0.368	No
2MASS J02500703+0025251	02:50:07.02	+00:25:25.4	16.69	0.198	No
LBQS 0254+0101	02:56:46.96	+01:13:49.3	18.02	0.177	No
2MASX J03041778+0028274	03:04:17.78	+00:28:27.3	17.00	0.044	No
2MASX J03063958+0003426	03:06:39.56	+00:03:43.1	17.56	0.107	Yes
LBQS 0307-0101	03:10:27.82	-00:49:50.7	15.75	0.080	No
2MASS J03221390+0055134	03:22:13.90	+00:55:13.4	16.43	0.185	No
2MASS J03233765+0035555	03:23:37.64	+00:35:55.7	17.98	0.215	No
2MASX J03510759-0526370	03:51:07.59	-05:26:37.0	17.65	0.069	No
2MASX J04092918-0429021	04:09:29.15	-04:29:02.6	18.07	0.030	No
RX J0752.8+2617	07:52:45.60	+26:17:35.7	16.80	0.082	Yes
QSO B0752+393	07:55:25.29	+39:11:09.9	15.43	0.034	No
RX J0801.5+4736	08:01:31.97	+47:36:16.0	15.73	0.157	Yes

Object Name	R. A. (hh:mm:ss.ss)	Dec. (dd:mm:ss.s)	V (mag)	$z$	Detected in Radio
RXS J080358.9+433248	08:03:59.23	+43:32:58.4	17.20	0.451	No
1RXS J080534.6+543132	08:05:34.70	+54:31:32.0	15.50	0.406	No
SDSS J081222.99+461529.1	08:12:22.99	+46:15:29.1	17.50	0.311	No
2MASSi J0816522+425829	08:16:52.24	+42:58:29.4	17.25	0.235	No
SDSS J083045.36+340532.1	08:30:45.36	+34:05:32.1	16.13	0.062	No
SDSS J083202.16+461425.8	08:32:02.15	+46:14:25.7	15.72	0.046	No
2MASX J08394965+4847014	08:39:49.64	+48:47:01.4	16.80	0.039	No
SDSS J084025.51+033301.7	08:40:25.51	+03:33:01.7	16.69	0.060	No
NGC 2639 U10	08:42:30.51	+49:58:02.3	18.10	0.305	No
2MASX J08550420+5252477	08:55:04.17	+52:52:48.3	18.72	0.080	No
SDSS J085632.39+504114.0	08:56:32.40	+50:41:14.1	16.40	0.235	No
2MASX J08573780+0528211	08:57:37.78	+05:28:21.3	17.19	0.059	No
SDSS J085828.69+342343.8	08:58:28.71	+34:23:43.8	16.40	0.257	No
2MASX J09043699+5536025	09:04:36.95	+55:36:02.7	16.99	0.037	Yes
SDSS J090455.00+511444.6	09:04:55.01	+51:14:44.6	16.87	0.224	No
RX J0906.0+4851	09:06:01.33	+48:51:48.9	17.50	0.390	No
RX J0908.7+4939	09:08:47.39	+49:40:06.1	17.30	0.419	No
SDSS J092554.25+533558.2	09:25:54.26	+53:35:58.2	18.60	0.070	No
1WGA J0931.9+5533	09:32:00.08	+55:33:47.4	17.48	0.266	Yes
SDSS J093653.84+533126.8	09:36:53.85	+53:31:26.8	17.11	0.228	No
QSO B0934+013	09:37:01.04	+01:05:43.7	15.98	0.051	No
FIRST J094610.9+322325	09:46:11.00	+32:23:26.4	17.54	0.403	Yes
KUV 09484+3557	09:51:23.94	+35:42:49.0	16.30	0.400	No
HS 1001+4840	10:04:13.78	+48:26:07.2	18.10	0.563	No
LBQS 1008+0058	10:10:44.51	+00:43:31.3	16.50	0.178	Yes
2MASS J10131485-0052338	10:13:14.86	-00:52:33.5	17.94	0.276	No
1WGA J1016.7+4210	10:16:45.11	+42:10:25.4	16.42	0.056	Yes
PC 1014+4717	10:17:30.98	+47:02:25.1	18.10	0.335	No

Object Name	R. A. (hh:mm:ss.ss)	Dec. (dd:mm:ss.s)	V (mag)	$z$	Detected in Radio
Mrk 142	10:25:31.28	+51:40:34.8	15.20	0.045	Yes
RX J1030.4+5516	10:30:24.95	+55:16:22.8	17.80	0.435	Yes
FBQS J103359.4+355509	10:33:59.48	+35:55:09.5	16.76	0.169	Yes
2MASX J10425297+0414413	10:42:52.94	+04:14:41.1	17.66	0.052	No
SBS 1047+557B	10:50:55.14	+55:27:23.2	16.70	0.331	No
RX J1054.7+4831	10:54:44.70	+48:31:39.1	15.70	0.286	Yes
FBQS J105648.1+370450	10:56:48.18	+37:04:50.4	17.90	0.387	Yes
2MASX J10570691-0041446	10:57:06.94	-00:41:45.1	17.87	0.188	No
2MASS J10593576-0005513	10:59:35.76	-00:05:51.2	17.88	0.283	No
2MASX J11050361+0745313	11:05:03.60	+07:45:31.0	18.07	0.073	No
FBQS J110704.5+320630	11:07:04.52	+32:06:30.2	17.60	0.243	Yes
MCG+10-16-111	11:18:57.68	+58:03:23.5	15.33	0.027	No
2MASX J11220940+0117199	11:22:09.40	+01:17:19.5	18.03	0.058	No
SDSS J112813.02+102308.3	11:28:13.02	+10:23:08.3	16.45	0.050	Yes
FBQS J112956.5+364919	11:29:56.50	+36:49:19.0	17.59	0.399	Yes
2MASX J11390898+5911547	11:39:08.97	+59:11:54.8	15.33	0.060	No
2MASX J11410569+0241173	11:41:05.71	+02:41:17.0	16.79	0.090	No
FBQS J115117.7+382221	11:51:17.76	+38:22:21.7	16.20	0.336	Yes
LBQS 1150+0010	11:52:34.99	-00:05:42.7	17.50	0.129	No
2MASS J11574174+0412506	11:57:41.75	+04:12:50.5	18.22	0.095	No
2MASS J11575874-0022208	11:57:58.73	-00:22:20.7	16.38	0.260	No
RX J1200.4+3334	12:00:28.70	+33:34:43.0	17.71	0.284	No
2MASX J12033294+0229346	12:03:32.94	+02:29:34.6	14.76	0.077	Yes
RX J1203.8+3711	12:03:53.70	+37:11:33.0	18.57	0.401	Yes
1RXS J121759.9+303306	12:17:59.50	+30:33:14.0	17.99	0.363	No
RX J1218.3+3850	12:18:22.72	+38:50:43.5	16.02	0.194	No
FBQS J122035.1+385317	12:20:35.10	+38:53:16.7	16.60	0.376	Yes
Mrk 50	12:23:24.13	+02:40:44.4	14.84	0.023	No
FBQS J122424.2+401510	12:24:24.20	+40:15:10.0	17.79	0.415	Yes

Object Name	R. A. (hh:mm:ss.ss)	Dec. (dd:mm:ss.s)	V (mag)	$z$	Detected in Radio
FBQS J122624.2+324429	12:26:24.22	+32:44:29.4	17.01	0.242	Yes
2MASX J12431998+0252562	12:43:19.98	+02:52:56.1	15.62	0.087	No
LBQS 1244+0238	12:46:35.24	+02:22:08.7	16.20	0.048	Yes
FBQS J125602.0+385230	12:56:02.06	+38:52:30.7	18.00	0.419	Yes
Mrk 236	13:00:19.96	+61:39:18.1	16.10	0.051	No
2MASX J13005216+5641056	13:00:52.10	+56:41:05.8	16.88	0.072	No
2MASS J13071325-0036018	13:07:13.25	-00:36:01.6	17.53	0.170	No
2MASS J13075656+0107097	13:07:56.57	+01:07:09.6	17.59	0.275	No
FBQS J132515.0+330556	13:25:15.01	+33:05:56.2	18.30	0.356	Yes
1WGA J1331.6+0131	13:31:38.03	+01:31:51.6	17.35	0.080	Yes
LBQS 1338-0038	13:41:13.93	-00:53:15.1	17.05	0.237	Yes
2MASX J13421004+5642106	13:42:10.11	+56:42:10.2	17.00	0.040	No
LBQS 1340-0038	13:42:51.60	-00:53:45.2	17.00	0.326	No
SDSS J134351.07+000434.8	13:43:51.60	+00:04:34.7	16.79	0.074	No
2MASX J13442643+4416194	13:44:26.41	+44:16:20.0	17.16	0.055	No
SDSS J134452.91+000520.2	13:44:52.91	+00:05:20.2	15.85	0.087	No
LBQS 1342-0000	13:44:59.45	-00:15:59.5	17.80	0.245	No
2MASS J13452470-0259396	13:45:24.69	-02:59:39.8	17.18	0.085	No
2MASX J13495283+0204456	13:49:52.84	+02:04:45.1	16.14	0.033	Yes
SDSS J135542.76+644045.0	13:55:42.75	+64:40:44.9	16.76	0.070	No
LBQS 1434+0020	14:37:04.12	+00:07:05.0	17.50	0.140	No
SDSS J144050.77+520446.0	14:40:50.77	+52:04:46.0	17.80	0.317	No
RX J1452.4+4522	14:52:24.67	+45:22:23.7	17.30	0.469	Yes
FBQS J145958.4+333701	14:59:58.43	+33:37:01.8	16.11	0.645	Yes
Mrk 1392	15:05:56.55	+03:42:26.3	14.58	0.036	Yes
2MASX J15102489+0058438	15:10:24.92	+00:58:43.9	17.69	0.070	No
2MASX J15192168+5908239	15:19:21.67	+59:08:23.7	15.89	0.079	No
2MASX J15195659+0016149	15:19:56.57	+00:16:14.5	17.62	0.114	No
QSO B1534+580	15:35:52.40	+57:54:09.5	15.00	0.030	Yes

Object Name	R. A. (hh:mm:ss.ss)	Dec. (dd:mm:ss.s)	V (mag)	$z$	Detected in Radio
SDSS J153830.78+444038.5	15:38:30.78	+44:40:38.5	17.67	0.073	No
FIRST J154348.6+401324	15:43:48.60	+40:13:24.9	13.05	0.318	Yes
SDSS J154833.03+442226.0	15:48:33.03	+44:22:26.1	17.40	0.321	Yes
FBQS J155147.4+330007	15:51:47.42	+33:00:07.9	17.60	0.422	Yes
2MASX J15541741+3238381	15:54:17.43	+32:38:37.8	14.92	0.048	Yes
MCG+06-36-003	16:13:01.63	+37:17:14.8	14.80	0.070	No
SDSS J161951.31+405847.2	16:19:51.31	+40:58:47.2	15.08	0.038	No
Mrk 699	16:23:45.88	+41:04:56.3	15.55	0.034	Yes
2E 1652.4+3930	16:54:08.15	+39:25:33.3	15.81	0.069	No
2MASS J16595894+6202181	16:59:58.93	+62:02:18.1	17.91	0.232	No
QSO B1717+5818	17:17:50.59	+58:15:14.0	17.20	0.310	No
2MASS J17190229+5937159	17:19:02.29	+59:37:15.8	17.59	0.178	No
2MASS J17202672+5540243	17:20:26.69	+55:40:24.0	16.96	0.359	No
SDSS J205822.14-065004.3	20:58:22.14	-06:50:04.3	18.54	0.070	No
2MASS J23493277-0036458	23:49:32.76	-00:36:45.6	16.90	0.279	No
SDSS J235156.12-010913.3	23:51:56.12	-01:09:13.3	15.30	0.174	Yes

Note – This table reports a summary of some general properties of the objects included in our sample. It lists the names of the objects, their coordinates in the sky, the apparent magnitudes in the V band, the cosmological redshifts, and a flag reporting whether the sources have been detected by the FIRST VLA sky survey.



# Chapter 5

## Thermodynamical Properties of the BLR

### 5.1 Introduction

Due to its proximity to the central energy source of AGN, the properties of the BLR are tightly related to the physical processes occurring in these objects. Therefore, understanding its physics and kinematics is a crucial step in the investigation of AGN. Indeed, there are three main reasons of interest: first of all, there is outstanding evidence for interaction among the spectral continuum and the emission lines originated in the BLR; on the other hand, the kinematics of the BLR gas is probably controlled by the central source, through the competing effects of its gravity and its radiation pressure; finally, a large fraction of the X-ray and UV energy, emitted by the continuum source, is reprocessed in the BLR and transferred to the broad emission lines, which, as a consequence, carry indirect information concerning the unknown properties of the ionizing continuum.

In order to improve the overall understanding of AGN physics, many BLR studies were focused on geometries, dimensions, and correlations among the BLR kinematical properties and the general characteristics of the corresponding AGN (see e. g. Sulentic et al. 2000a; Popović et al. 2004; Kaspi et al.

2005 etc.), while other works have been devoted to reconstructing the physical conditions in the BLR emitting gas (Kaspi & Netzer 1999; Popović 2003; Popović et al. 2006; Korista & Goad 2004, 2005; Véron-Cetty et al. 2006). The broad line strength, width, and shape are powerful tools for gas diagnostics in the different parts of the emitting region of AGN (e. g. Osterbrock 1989). However, there is the problem that the broad emission lines are complex and that they are probably coming from different regions with possible changes in the kinematical and physical conditions. Furthermore, it has been shown that the broad emission line profiles of some AGN may be explained with a two-component model (see e. g. Popović et al. 2002, 2003, 2004; Ilić et al. 2006; Bon et al. 2006).

Here we describe our investigation of the spectral features in the 90 objects included in our first selection of the sample, combining the analysis of the broad Balmer emission line components with a study of the source physical properties, that we were able to infer from the available data. Exploiting some recent results that have been achieved by means of the RM technique (see, for example, Kaspi 2005; Bentz 2006), we try to determine the thermodynamical influence played by the radiation field on the BLR plasma and to constrain its role in controlling the BLR structure. This chapter is organized according to the following plan: in § 5.2 we outline the theory behind the techniques of investigation that we adopted to explore the BLR plasma physics; in § 5.3 we report the extraction of our measurements and their related uncertainties; § 5.4 will list our results, with a discussion of our findings and their limits, while in § 5.5 we summarize our concluding remarks.

## 5.2 Boltzmann Plots for Plasma Diagnostics

The ratio among the broad emission line fluxes depends on the physical processes, such as collisions, photo-ionizations, and recombinations, which affect the plasma ionization and excitation balance, as well as on the effects of radiation transfer from the source to the observer. The detailed treatment of

this balance in dense astrophysical environments is very complex, but, under specific circumstances, some general information, concerning the physical conditions in the line emitting material, might be inferred without a complete calculation of the actual configuration. If we consider the case of a line emitting plasma, that, for simplicity, we assume to be optically thin with respect to its own emission line photons, we can express the wavelength integrated flux of a single line, originated in the transition from an excited ion configuration  $u$  to a lower energy level  $l$ , as:

$$F_{ul} = \frac{hc}{\lambda_{ul}} A_{ul} g_u \int_0^\ell N_u dx, \quad (5.1)$$

where we denoted with  $\lambda_{ul}$  the transition wavelength, with  $A_{ul}$ ,  $g_u$ , and  $N_u$  the radiative transition probability, the upper level's statistical weight, and its population, respectively, while  $\ell$  represents the spatial extension of the line emitting region.

If the electrons can reach an equilibrium between ionization and recombination, the plasma may settle down to a configuration where the population of the high energy levels of ions, with respect to the next ion's ground state, is described by Saha-Boltzmann distributions, with the electron temperature in the place of the excitation one. In this condition, which is referred to as a *Partial Local Thermodynamical Equilibrium* (PLTE), Eq. (5.1) can be expressed as (see, e. g., Griem 1997; Konjević 1999; Popović 2003):

$$F_{ul} \approx \frac{hc}{\lambda_{ul}} A_{ul} g_u \ell \frac{N_0}{Z} \exp\left(-\frac{E_u}{k_B T_e}\right), \quad (5.2)$$

in which  $N_0$  represents the total number density of the radiating species,  $Z$  its partition function, and  $E_u$  the upper level's excitation energy, while  $T_e$  is the local electron temperature. It is convenient to normalize the integrated flux of Eq. (5.2) with respect to the atomic constants, that characterize the transition, by introducing the normalized line intensity:

$$I_n = \frac{\lambda_{ul} F_{ul}}{A_{ul} g_u}. \quad (5.3)$$

Using Eq. (5.2) into Eq. (5.3), we find that the normalized line intensity, for the emission lines of a particular ion species, is a function of the electron

temperature and of the high excitation level's energy:

$$I_n \approx hcl \frac{N_0}{Z} \exp\left(-\frac{E_u}{k_B T_e}\right). \quad (5.4)$$

The Boltzmann Plot method (BP) exploits the normalized intensities of several emission lines, in order to study the thermodynamical conditions of the line emitting plasma. Taking into account a number of emission lines, that belong to the same transition series, the terms describing the ion distribution in Eq. (5.4) do not change according to the choice of the upper energy level. The normalized line intensity, then, may be put in the form of:

$$\log(I_n) = B - AE_u, \quad (5.5)$$

where  $B$  is a constant whose value is a characteristic of the involved transition series, while  $A$  takes the role of a *temperature parameter*, corresponding to:

$$A = \frac{\log e}{k_B T_e} \approx \frac{5060}{T_e} \quad [\text{K}^{-1}]. \quad (5.6)$$

Therefore, in conditions of PLTE, the normalized line intensities of a specific series of transitions, involving high excitation levels of an ion, fall onto a straight line in the parametric plane of  $\log(I_n)$  vs.  $E_u$ , whose slope is inversely proportional to the electron temperature. The ability of a straight line to fit the real distribution of data reflects the approximation of Eq. (5.4), which appropriately describes a PLTE plasma, where the emission line photons are not re-absorbed within the source.

Unfortunately, it is very unlikely that the assumptions, on which the BP technique is based, can be valid throughout the whole BLR environment. Furthermore, the possibility that a relationship, like Eq. (5.5), may be induced by radiation transfer in a high optical depth plasma should also be considered. On the other hand, it has been argued that such circumstances arise more frequently in presence of a high temperature recombination dominated plasma or under the effect of strong intrinsic reddening within the source (see, for instance, Popović 2003, 2006), where the BP would not serve as an effective thermodynamical diagnostic tool. These extreme conditions,

too, may not apply in general to the complex structure of the BLR, where we should, therefore, expect to find at least a fraction of the gas in fairly good agreement with the fundamental hypotheses of the BP. In the following sections, we investigate the role played by this component, studying how the results of a BP analysis of the BLR spectra are related with various components of the broad Balmer emission line profiles.

### 5.3 Spectral Analysis

Once the broad line components had been fairly isolated in the spectra, we performed a number of measurements in order to estimate their fluxes and the corresponding profile widths, taken both as *full widths at half the maximum* (FWHM) and as *full widths at zero intensity* (FWZI) levels. In order to improve our accuracy, the fluxes of the Balmer lines were measured several times and the uncertainties to be associated to the averaged flux determinations were computed as:

$$\sigma_F = \sqrt{\left(\frac{\sigma_{\text{cont}}}{I_{50}} \cdot F\right)^2 + \bar{\sigma}_F^2}, \quad (5.7)$$

where  $\sigma_{\text{cont}}$  represents the rms due to noise fluctuations, that we estimated in the continuum close to the emission lines,  $F$  and  $I_{50}$  are, respectively, the total fluxes of the lines and their half maximum intensities, while  $\bar{\sigma}_F$  is the standard deviation of our multiple flux determinations, computed assuming different choices of the continuum intensity level. A list of flux ratios for various Balmer lines, with respect to  $\text{H}\beta$ , from our sources, is given in Table 5.1. Their uncertainties were obtained as:

$$\sigma_{R_j} = R_j \cdot \sqrt{\left(\frac{\sigma_{F_j}}{F_j}\right)^2 + \left(\frac{\sigma_{\text{H}\beta}}{F_{\text{H}\beta}}\right)^2}, \quad (5.8)$$

where  $R_j$  is the ratio of  $j^{\text{th}}$  Balmer line with respect to  $\text{H}\beta$ .

Because of the lack of any direct method to estimate the ionizing continuum luminosity of these objects, by means of their SDSS spectra, we

searched for alternative indications of this very important parameter. Since the strength of the ionizing radiation field is certainly related with the emission line intensity of photo-ionized regions, we looked at the narrow emission lines of [O III] to test the assumption that the optical continuum luminosity of our spectra is actually related to the corresponding ionizing continuum. For this reason we performed similar flux measurements on the [O III] emission line at 5007 Å, that are also reported in Table 5.1.

In order to estimate the FWHM and FWZI, we restricted our attention only on the strongest spectral features of the BLR, namely H $\alpha$  and H $\beta$ , and the [O III] 5007Å line of the NLR. After choosing a zero emission intensity level, we computed the line peak intensities and we used the inferred values to define a half maximum intensity. Half widths at half the maximum and at zero intensity were taken both on the red and the blue line wings, respectively where the line profiles crossed the half and the zero intensity levels. Such determinations were repeated several times for each line, taking into account different guesses to the zero intensity levels, then they were averaged together, eventually providing the mean values with their corresponding standard deviations. We corrected the emission line profiles for instrumental broadening, assuming that the profiles were affected by the instrumentation according to:

$$W_{\text{obs}} = \sqrt{W_{\text{int}}^2 + W_{\text{ins}}^2}, \quad (5.9)$$

where  $W_{\text{obs}}$  and  $W_{\text{int}}$  are the observed and intrinsic line widths, while  $W_{\text{ins}}$  characterizes the instrumental broadening, which, in terms of velocity units, may be expressed as  $W_{\text{ins}} = c/R \approx 160 \text{ km s}^{-1}$ .

To estimate the continuum luminosities, we performed averaged flux measurements over the rest frame wavelength range running from 5075 Å to 5125 Å. The fluxes, that we derived both in the continuum and in the selected emission lines, were converted into specific luminosities, making the assumption of isotropic emission of radiation from the sources. Here we used the cosmological redshift as a distance estimator, in the framework of a model characterized by  $H_0 = 75 \text{ km s}^{-1} \text{ Mpc}^{-1}$ ,  $\Omega_m = 0.3$ , and  $\Omega_\Lambda = 0.7$ . We as-

sumed the sources included in our sample to have optical luminosities given by:

$$L_{5100} = 5100 \text{ \AA} L_{\lambda}, \quad (5.10)$$

where  $L_{\lambda}$  is the specific continuum luminosity measured at 5100 Å (in units of  $\text{erg s}^{-1} \text{ \AA}^{-1}$ ), and their bolometric luminosities, which we needed in order to investigate the role of the ionizing radiation field, to be roughly ten times as much (see Elvis et al. 1994, but also the discussions given by Collin et al 2002; Collin & Kawaguchi 2004).

## 5.4 Results

Since we are going to consider the influence of the central source of an AGN onto the BLR, we must necessarily confront the problems due to its currently unresolvable structure. The conversion of observational data into physical parameters requires some assumptions to be made about the BLR structure and dynamics. Recent investigations (e. g. Vestergaard et al. 2000; Niłojajuk et al. 2005; Peterson et al. 2004; Sulentic et al. 2006, etc.) suggested that the BLR geometry should be considerably flattened, rather than spherical, and its motions should occur mainly in an orbital configuration, as opposed to radial infalls or outflows. Because kinematical information from spectroscopic observations of unresolved sources only concerns the radial component of the actual motion pattern, our measurements are limited to the projection of the gas flows onto our line of sight.

Given that the BLR is dynamically affected by the gravitational field of the central source and by its radiation pressure, the broad line emitting medium must be controlled by the balance of these forces. As a consequence, the mass of the central engine and its energetic output should be tightly related to the size and velocity field measured in the BLR (Wandel et al. 1999; Wu et al. 2004; Peterson et al. 2004; Kaspi et al. 2005). In order to estimate the size of the BLR, a number of AGN have been studied with the Reverberation Mapping technique, described in Chapter 3. Although

this method is currently one of the most powerful available probes of the structure of the BLR, it is very expensive, because it requires large monitoring campaigns for each object under study. Using the available data it was nonetheless possible to investigate how the BLR radii change as a function of the AGN luminosities in various spectral ranges. In the optical domain Kaspi et al. (2005) argued that the size of the BLR scales with the source luminosity according to:

$$\frac{R_{\text{BLR}}}{10 \text{ lt-days}} = (2.23 \pm 0.21) \left[ \frac{\lambda L_{\lambda}(5100 \text{ \AA})}{10^{44} \text{ erg s}^{-1}} \right]^{0.69 \pm 0.05}. \quad (5.11)$$

More recently (see, e. g., Bentz et al. 2006), this kind of relationship has been reviewed for different RM sources and it has been suggested that the power law index of Eq. (5.11) may be consistent with the value of  $\alpha = 0.5$ , predicted on the basis of some simple photo-ionization calculations, that essentially assume a small range of standard values for the gas column densities, the ionization parameter, and the ionizing SED in the BLR of different AGN. The two interpretations differ in the way of dealing with the host galaxy contamination. In view of our reduction procedures, the interpretation given by Bentz et al. (2006) is more suitable to estimate the source properties from our measurements. We adopt this interpretation in the calculation of the BLR size, but we compare it with the predictions of the one suggested by Kaspi et al. (2005).

Once we have calculated a typical BLR size, it is possible to estimate the dynamical influence, played by the central SMBH, from the kinematical information that we measured in our spectra. In the course of the past years, many efforts were spent in order to clarify the relation of simple AGN spectral properties, such as the emission line widths, and the intrinsic dynamics of the sources. Assuming the BLR to be in virial equilibrium with the gravitational potential of the central engine (see e. g. Woo & Urry 2002; Sulentic et al. 2006 and references therein, for a discussion of implications), a general expression to estimate the SMBH mass is:

$$M_{\text{BH}} = \frac{R_{\text{BLR}} \Delta v^2}{G}, \quad (5.12)$$

where  $G$  is the gravitational constant and  $\Delta v$  represents a velocity field, which is somehow related to the emission line profiles. In the lack of useful information, concerning the real flattening of the BLR and its inclination with respect to our line of sight (see, for example, Bian 2005, for a discussion of the BLR inclination), Netzer (1990) proposed an isotropic motion pattern, where the appropriate velocity field could be computed from the FWHM of the involved emission lines, by means of:

$$\Delta v = \frac{\sqrt{3}}{2} \text{FWHM}, \quad (5.13)$$

and subsequently be introduced into Eq. (5.12) to get the mass. Furthermore, combining a measurement of the continuum luminosity with the black hole mass, it is possible to give rough estimates of the accretion rates onto the SMBH, with respect to their Eddington limits:

$$\dot{M} = \frac{L_{\text{bol}}}{\eta c^2} = \dot{M}_{\text{Edd}} \frac{L_{\text{bol}}}{L_{\text{Edd}}}, \quad (5.14)$$

where  $L_{\text{bol}} \approx 10L_{5100}$  is the bolometric luminosity and  $\eta$  is the efficiency of the accretion process, here assumed to be of order 10%, representing the fraction of rest energy, in the mass flow, that is converted to radiation. Such simple estimates, however, are potentially prone to large uncertainties, because the simplified assumptions, that they adopt, do not take into account the fundamental role of the BLR structural properties. For this reason, we do not apply Eq. (5.12) and Eq. (5.14) to estimate masses and accretion rates in our objects, but only to compare their properties with the predictions of our structural models. We give a summary of the results, so far achieved by our calculations, in Table 5.2, while the calculation of masses and accretion rates will be performed in the next chapter, where the role of the BLR geometry is investigated in greater detail.

Since the selection of this sample is limited in redshift by the requirement of the Balmer series falling into the available spectral range, it lacks the most powerful broad line AGN. However, as we show in Fig. 5.1, where we compare the FWHM of  $H\beta$  and the [O III] forbidden emission line,

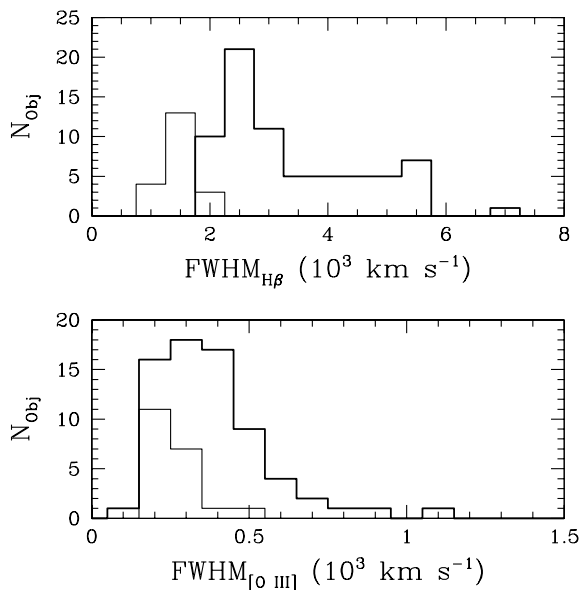


Figure 5.1: Line width distribution of the sample, plotted as a comparison of the FWHM in  $\text{H}\beta$  (top panel) and the corresponding value in  $[\text{O III}] \lambda 5007$  (bottom panel). The thin continuous histograms show the distribution of NLS1 galaxies, with  $\text{FWHM}_{\text{H}\beta} < 2000 \text{ km s}^{-1}$ , while the thick continuous histograms represent broad line emitting AGN.

the sample appears to be fairly well distributed, although there are no objects featuring very broad lines. Among the 90 spectra of this sample, 20 match the classical definition of *Narrow Line Seyfert 1* (NLS1) galaxies, with  $\text{FWHM}_{\text{H}\beta} < 2000 \text{ km s}^{-1}$ , while the others are spread in the range of  $2000 \text{ km s}^{-1} < \text{FWHM}_{\text{H}\beta} < 7000 \text{ km s}^{-1}$ . NLS1 are typically different from other Seyfert galaxies under many points of view. They are commonly observed to have super-solar metallicities in their nuclei and they often show strong Fe II multiplets, together with a soft slope and high variability in the X-rays (see e. g. Boller et al. 1996). Moreover they are usually observed to have relatively high Fe II /  $[\text{O III}]$  intensity ratios and strong soft X-ray excesses. Many explanations have been proposed by various authors to give

an interpretation of the properties found in NLS1. Simply assuming that the line broadening depends on the gravitational potential of the SMBH and that the BLR is not systematically larger in these sources, Boller et al. (1996) suggested that NLS1 are powered by comparatively low mass black holes, with respect to normal Seyfert 1 galaxies. It has also been proposed that they could be young AGN in a growing phase (Mathur et al. 2001), that the narrow line profiles could be the effect of a partially obscured BLR (Smith et al. 2002) or that they could arise from an extremely flat geometry seen at low inclinations (Osterbrock & Pogge 1985), but the polarization signatures which we should expect in the last two cases have not been reported so far. Many of the characteristic properties of NLS1 could not be further investigated in our sample, because of its limited spectral coverage and of the usually not ideal s/n ratios, which, in many cases, did not allow us to actually measure the strength of Fe II emission. In conclusion, we found that the NLS1 in this sub-sample, that are located at an average redshift of  $z = 0.064$ , have on average the  $L_{\text{FeII}}/L_{5100} = 0.029 \pm 0.013$ ,  $L_{\text{FeII}}/L_{[\text{OIII}]} = 4.30 \pm 3.08$ , and  $L_{\text{FeII}}/L_{\text{H}\beta} = 16.82 \pm 7.81$  luminosity ratios, while the other AGN have  $L_{\text{FeII}}/L_{5100} = 0.024 \pm 0.020$ ,  $L_{\text{FeII}}/L_{[\text{OIII}]} = 4.36 \pm 5.31$ , and  $L_{\text{FeII}}/L_{\text{H}\beta} = 13.09 \pm 11.66$ . In the following we kept a distinction of NLS1 galaxies from the other AGN.

#### 5.4.1 The Continuum Source and Emission Line Properties

At present it is strongly believed that the main interactions between the central power source of an AGN and the surrounding emission line regions occurs via radiative processes. A direct measurement of the AGN continuum luminosity on the spectra, however, is not straightforward because of the several uncertainties about the actual ionizing SED in the source, which can even be affected in various manners by stellar contributions from the AGN host galaxy (see, for instance, Bentz et al. 2006). On the other hand, some clues about the reliability of the optical continuum intensity as an estimator

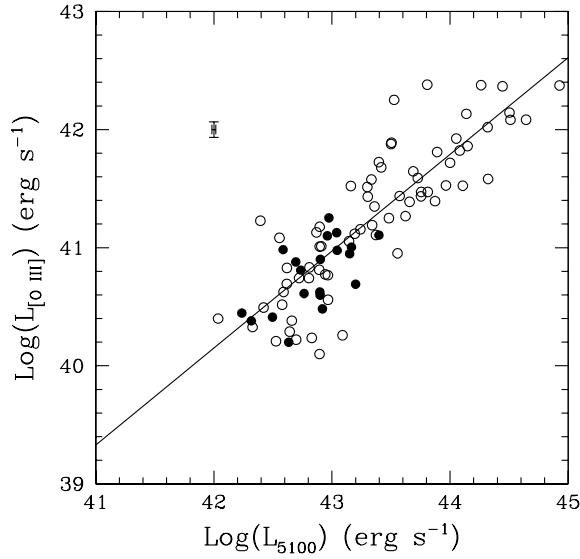


Figure 5.2: Correlation between the [O III]  $\lambda 5007$  line luminosity and the optical continuum luminosity measured in the spectra. NLS1 galaxies have been identified with filled circles, while the other broad line emitting sources are represented by open circles. The cross located in the upper left corner of the diagram shows the median uncertainty of our measurements. The straight line fit is achieved by means of Eq. (5.15). Intrinsic absorption and starlight contributions might be responsible for the scatter.

of the ionizing radiation field strength come from the observation of how the emission line intensities, which should be controlled by the amount of ionizing radiation, correlate with the estimated continuum luminosities. In Fig. 5.2, we show the distribution of our sample in the case of [O III]  $\lambda 5007$  as a function of the optical source luminosities. The behaviour that we find is described by the relation:

$$\log(L_{[\text{O III}]}) = (0.820 \pm 0.052) \cdot \log(L_{5100}) + (5.710 \pm 2.270), \quad (5.15)$$

with a correlation coefficient  $R = 0.712$  and a probability to occur by chance  $P_0 < 10^{-6}$ . Most of the scatter observed in this relation can be accounted for

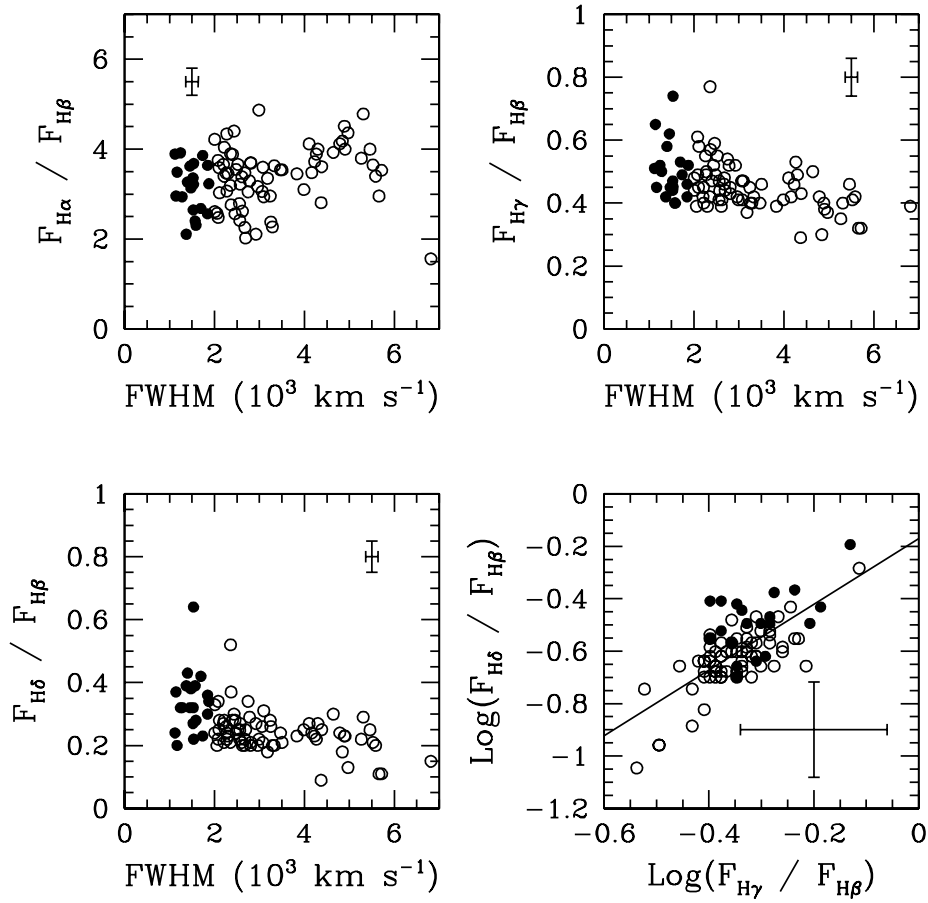


Figure 5.3: Panels from the upper left to the lower left show the Balmer line flux ratios with respect to  $H\beta$  as a function of the FWHM measured in spectra. We observe an averagely larger Balmer decrement in objects with broader line profiles. The bottom right panel illustrates the only correlation observed between  $H\delta/H\beta$  and  $H\gamma/H\beta$ . We plot with open circles the broad line emitting sources and with filled ones NLS1 galaxies. The median uncertainty estimates are given by the crosses shown in each plot.

in terms of intrinsic source absorptions or stellar light contributions which could have been not perfectly removed.

Turning our attention onto the Balmer line intensity ratios over the sample, we found the median values of  $H\alpha / H\beta = 3.45 \pm 0.65$ ,  $H\gamma / H\beta = 0.45 \pm 0.08$ , and  $H\delta / H\beta = 0.25 \pm 0.08$ . We, then, compared the properties of the sources with the corresponding line profiles. The plots shown in Fig. 5.3 illustrate the Balmer line flux ratios as a function of the FWHM measured in the spectra. Our measurements of the Balmer line flux ratios are prone to quite large uncertainties, presumably reflected by the resulting scatter, but the plots suggest the existence of a weak relation between the Balmer decrement and the width of the line profiles. Although the correlations are not particularly strong (having  $R = 0.226$ ,  $P_0 = 3.34 \cdot 10^{-2}$  in the case of  $H\alpha / H\beta$ , while  $R = -0.482$ ,  $P_0 = 1.71 \cdot 10^{-6}$  for  $H\gamma / H\beta$ , and  $R = -0.510$ ,  $P_0 < 10^{-6}$  for  $H\delta / H\beta$ ), they apparently strengthen with increasing line widths, but this may be simply due to the small number of such objects. Almost no particular correlations are, instead, observed among the Balmer line flux ratios themselves, with the only exception of the ratios among  $H\delta / H\beta$  and  $H\gamma / H\beta$ , whose values are related by:

$$\log(F_{H\delta}/F_{H\beta}) = (1.253 \pm 0.133) \cdot \log(F_{H\gamma}/F_{H\beta}) - (0.171 \pm 0.047), \quad (5.16)$$

with a correlation coefficient of  $R = 0.709$  and  $P_0 < 10^{-6}$ . These findings agree very well with earlier results obtained by Rafanelli (1985), who, while investigating the relationships among the Balmer line intensities and profiles in a sample of 12 Seyfert 1 galaxies, recorded a correlation like the one given in Eq. (5.16), with a slope of 1.24, and the absence of similar relations involving the other emission lines.

### 5.4.2 Global Baldwin Effect

Concerning the relationship among the emission line intensities and the AGN continuum luminosity, we generally observe high degrees of correlation, supporting the hypothesis that the optical continuum luminosity might be used to estimate the ionizing radiation field. The occurrence of a power law slope like  $L_{[\text{O III}]} \propto L_{5100}^\alpha$  with  $\alpha = 0.820 \pm 0.52$  in Eq. (5.15), however, indicates

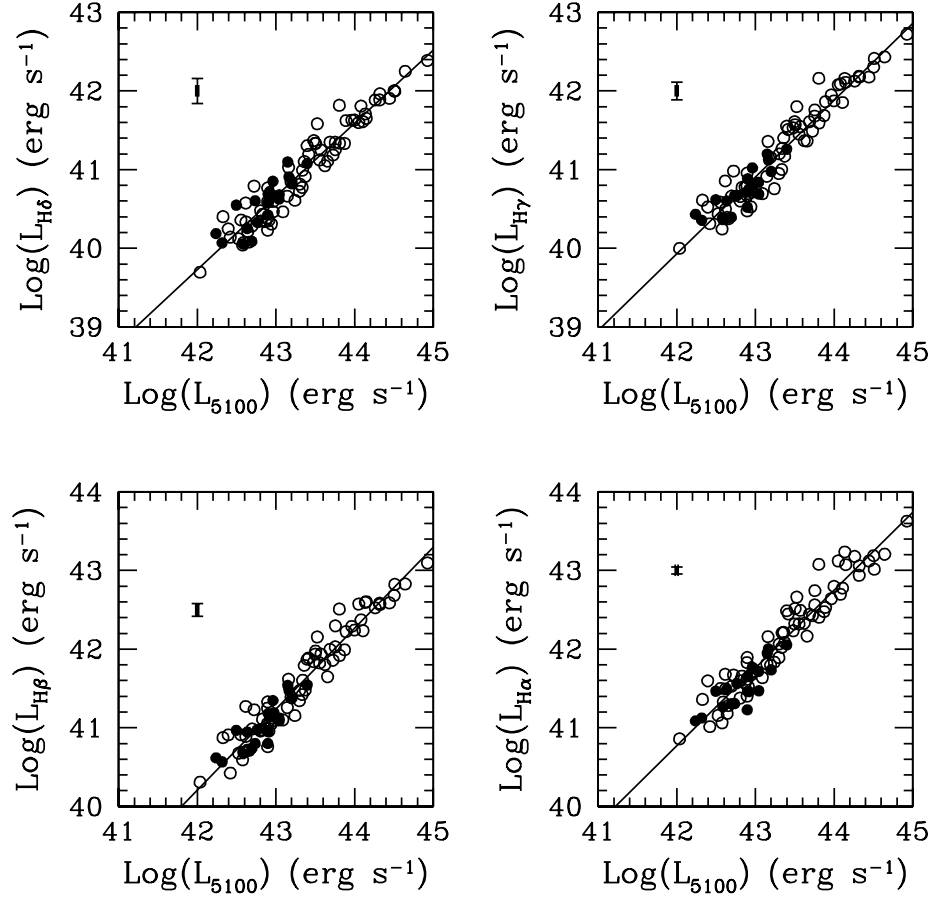


Figure 5.4: Correlations between the optical continuum luminosity and the H $\delta$  (upper left panel), H $\gamma$  (upper right panel), H $\beta$  (lower left panel), and H $\alpha$  emission line luminosities (lower right panel). Open circles represent broad line emitting objects, while filled circles are NLS1. The straight lines are the best fits of Eq. (5.17) and the error bars show the median uncertainties associated with our measurements.

the presence of a global Baldwin Effect in this line (Baldwin 1977; Kong et al. 2006). As we look for the situation of the broad Balmer line components, instead, we find little or no evidence for global Baldwin Effect, since

the observed emission line luminosities are related to the optical continuum through:

$$\log(L_{H\alpha}) = (0.989 \pm 0.031) \cdot \log(L_{5100}) - (0.784 \pm 1.346) \quad (5.17a)$$

$$\log(L_{H\beta}) = (1.029 \pm 0.030) \cdot \log(L_{5100}) - (3.025 \pm 1.289) \quad (5.17b)$$

$$\log(L_{H\gamma}) = (0.976 \pm 0.029) \cdot \log(L_{5100}) - (1.063 \pm 1.226) \quad (5.17c)$$

$$\log(L_{H\delta}) = (0.931 \pm 0.030) \cdot \log(L_{5100}) + (0.631 \pm 1.299), \quad (5.17d)$$

with correlation coefficients of  $R = 0.937$ ,  $0.967$ ,  $0.974$ , and  $0.972$ , spanning from Eq. (5.17a) to Eq. (5.17d), and  $P_0 < 10^{-6}$  in all cases. The situation of the Balmer lines is summarized in Fig. 5.4. Here we note that, although there are works which actually detected a significant intrinsic Baldwin Effect, particularly in the case of the broad  $H\beta$  component, in long time covering observations of some well studied objects (e. g. Gilbert & Peterson 2003; Goad et al. 2006), no strong indications have been found in literature concerning the existence of a global Baldwin Effect in the BLR Balmer line spectra (see e. g. Yee 1980; Binette et al. 1993; Osmer & Shields 1999).

### 5.4.3 Line Profiles and Boltzmann Plots

The Balmer line flux ratios, that we previously discussed, are the fundamental ingredient of our thermodynamical investigation of the BLR with the BP method. When we apply the BP to the Balmer series of a BLR spectrum, the resulting slope  $A$  clearly depends on the Balmer decrement, though there is a substantial difference between these two properties, since, for instance, we find objects with a rising BP slope ( $A < 0$ ), although this does not imply  $H\alpha$  to be actually fainter than the other Balmer lines, but only to have a lower *normalized* intensity. The shape of the Balmer decrement, as well, influences the BP, which can be dramatically limited by the restrictions involved in the assumptions about the physical conditions within the plasma. Intrinsic reddening effects of the AGN environment, too, may influence the method, enhancing low order lines with respect to the high order ones, thus taking to

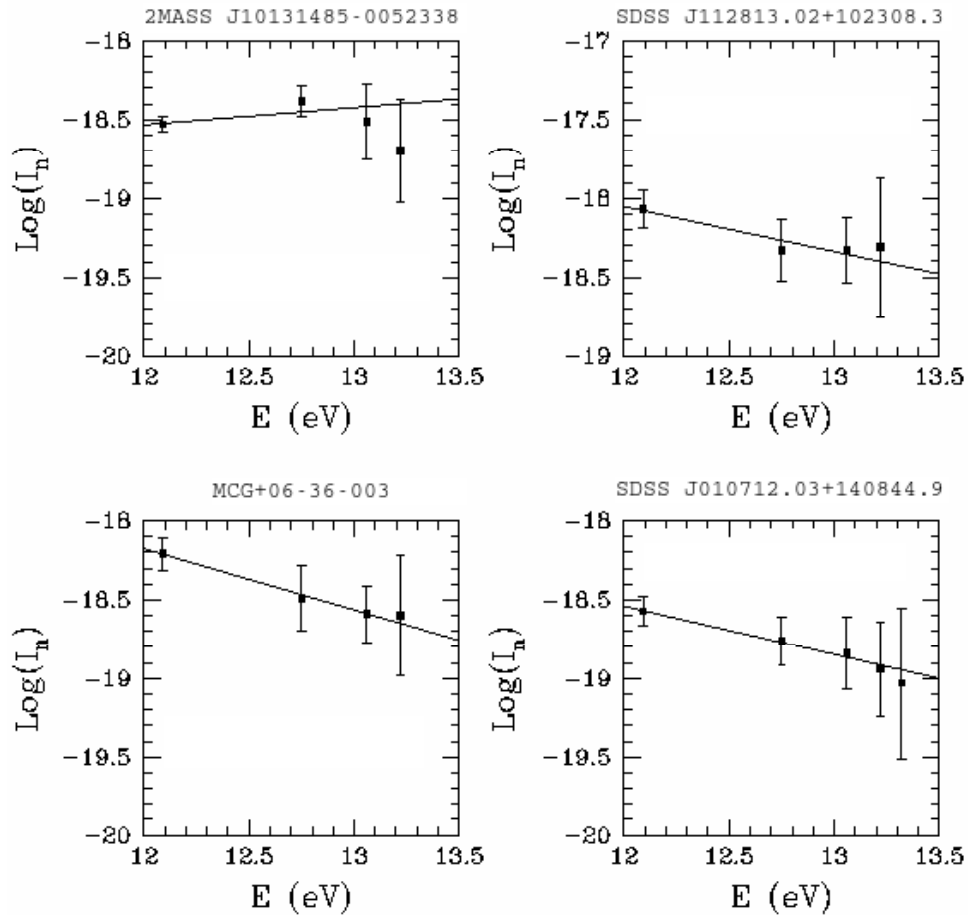


Figure 5.5: Four examples of Boltzmann Plots applied to the spectra of objects belonging to the sample: in the upper left panel no straight line fit is achieved (class iv); in the upper right panel only a poor fit is performed (class iii); the bottom left panel gives a good fit, but  $\text{H}\epsilon$  could not be detected in the spectrum (class ii); finally the bottom right panel shows a straight line fit to the normalized intensities of the Balmer series up to  $\text{H}\epsilon$  (class i).

a steeper straight line fit. Therefore, in presence of intrinsic reddening, the inferred BP temperatures would be probably lower than the actual values, although there are indications that the straight line fit to the normalized

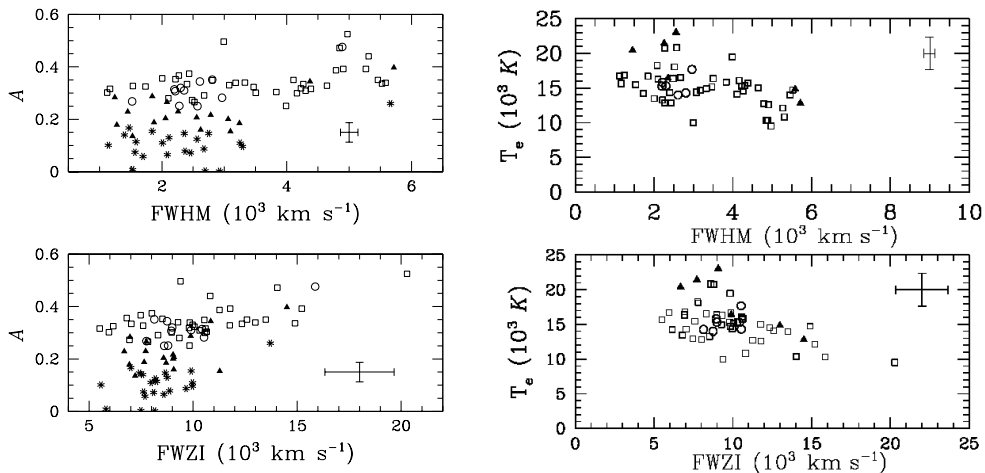


Figure 5.6: In the left panels we plot the BP slope  $A$  as a function of the BLR velocity fields, inferred by both the FWHM and FWZI of the Balmer lines: the open circles are sources of class i; the open squares represents objects of class ii; filled triangles are spectra of class iii and, finally, asterisks are objects with BP class iv. In the right panels we illustrate the inferred electron temperatures, with the same symbology, but only for objects where the BP analysis yielded reasonable fits. The crosses in the lower right corners of each panel are the median uncertainties of measurements.

intensities of the series is not qualitatively affected (Popović 2003).

According to whether the observed spectra could be described by a relation like Eq. (5.5), we studied the results of BP and we found the occurrence of four most common situations, corresponding to: (i) a good fit of the Balmer series up to the  $H\epsilon$  emission line; (ii) a good fit where, however, the  $H\epsilon$  line could not be detected; (iii) a poor fit to the observed lines; (iv) no possible straight line fit of the line normalized intensities. Examples for each one of these classes can be found in Fig. 5.5. We report the BP slopes and an indication of the proper class in Table 5.2, while, in Fig. 5.6, we show the distribution of the resulting BP slopes, as a function of the BLR velocity fields, and that of the inferred temperatures, when available. A summary of the

electron temperatures, estimated from the BP, is given in Table 5.3. Here we see that the BP slope increases on average with the broad line widths, as it was previously reported (Popović 2003, 2006). The total degree of correlation is quite weak ( $R = 0.381$ ,  $P_0 = 2.27 \cdot 10^{-4}$ , in the case of the relation between  $A$  and FWHM, while it is  $R = 0.470$ ,  $P_0 = 3.28 \cdot 10^{-6}$  for that between  $A$  and FWZI), but it grows significantly if only the cases where a reasonable BP fit is achieved are taken into account ( $R = 0.453$ ,  $P_0 = 1.08 \cdot 10^{-3}$  for  $A$  and FWHM,  $R = 0.579$ ,  $P_0 = 1.30 \cdot 10^{-5}$  for  $A$  and FWZI).

As it is clearly demonstrated by Fig. 5.6, the result of this BP analysis is to suggest the presence of lower temperature plasmas in objects, featuring broader emission lines, at least when the condition of PLTE appears to hold. More generally, objects with narrower emission lines have a shallower Balmer decrement, indicating either high temperature, or a large degree of ionization. An explanation to this observational effect can involve both intrinsic properties of the source, as well as the influence of extinction in different amounts of obscuring material.

#### 5.4.4 Line Profiles and AGN Accretion Rates

The rate of the accretion process that produces the ionizing continuum of radiation in AGN plays a fundamental role in affecting the physical conditions of the emission line regions. Many theoretical works suggest that the SED of an ionizing radiation field depends on the rate and the efficiency of the accretion process (e. g. Netzer et al. 1992; Kong et al. 2006), which, in turn, controls the ionization status of the BLR and its stability (Nicastro 2000).

Unfortunately, most determinations of the accretion rate in AGN may be considerably affected by the large uncertainties, that are related to several model dependent assumptions. Although there are works suggesting that many difficulties could be overtaken with the identification of more direct signatures of the accretion process in high energy spectra (see, for example, Shemmer et al. 2006), only the rough estimates, obtained by means of Eq. (5.14), are possible in absence of multi-frequency spectroscopic observa-

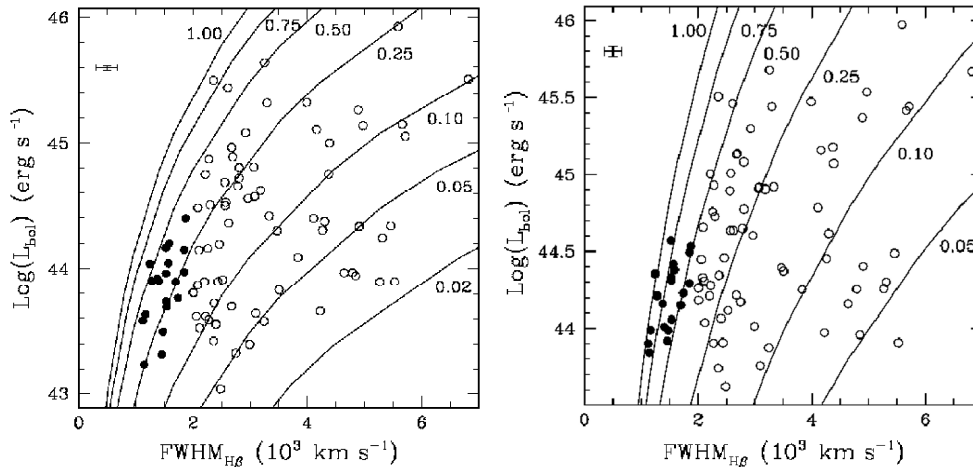


Figure 5.7: Bolometric luminosities vs.  $\text{FWHM}_{\text{H}\beta}$  in the sample, compared with models calculated in the assumption of the BLR structural model of Bentz et al. (2006) (left panel) and with the one of Kaspi et al. (2005) (right panel). Filled circles represent NLS1, while open circles are broad line AGN. The cross in the upper left corners gives the median uncertainty of the measurements. The curves track the expected locations of black holes with masses between  $10^4 M_{\odot}$  (bottom left side of the diagram) and  $10^9 M_{\odot}$  (upper right region) accreting at the labelled values of  $\dot{M}/\dot{M}_{\text{Edd}}$ , if their emission were isotropic, and the accretion efficiencies were  $\eta = 0.1$ .

tions. Such estimates essentially descend from a comparison of continuum luminosities and line profile widths. Once these measurements have been related to the bolometric luminosity and to the mass of the central energy source, with the choice of specific models, it is possible to evaluate the accretion rate of an object, that is usually expressed in terms of its ratio to the Eddington limit corresponding to the SMBH mass, or, in other words, as an *Eddington ratio*.

In our work, we tested how the assumption of two different structural models for the BLR affected the range of Eddington ratios covered by the sample, that we studied so far. Applying the simplified assumptions of Net-

zer (1990), we adopted isotropic gas motions and radiation field, together with a constant efficiency, to calculate the hypothetical bolometric luminosities of AGN powered by SMBH, with masses spanning over the range from  $10^4 M_{\odot}$  to  $10^9 M_{\odot}$ . The corresponding emission line widths were calculated for virial motions in the gravitational fields of these objects, using the BLR structural properties according to Bentz et al. (2006) and to Kaspi et al. (2005). The comparison is illustrated in the two diagrams of Fig. 5.7. According to these simple models, the distribution of our data in line width and continuum luminosity is achieved by various combinations of black hole mass and accretion rate, where the highest values of the Eddington ratio are found in the range of objects with relatively narrow line profiles. The main difference among the two schemes concerns the role of NLS1 galaxies, which do not appear to have exceptional properties, in the models based on Bentz et al. (2006), while they lie in the range of very high accretion rates, close to or even above the Eddington limit, if the BLR scales as in Kaspi et al. (2005).

## 5.5 Discussion

In this chapter we described our analysis of emission line flux and profile measurements, extracted from the spectra in the first selection of our sample. Most of our attention has been devoted to the investigation of the broad components of the Balmer emission line series, in order to test the efficiency of the BP technique, as a thermodynamical diagnostic tool, and to study the relationship among the broad Balmer line properties and the source kinematics. Although only a fraction of the objects under study were found to be in reasonable agreement with the physical assumptions, that are required to apply the BP for thermodynamical analysis, we found that both the shape of the Balmer decrement and the approximation to a condition of PLTE are related to the line profile widths. Objects with broad emission lines are associated with pronounced Balmer decrements, whose shape are usually in better agreement with the fundamental assumption of PLTE. On the other

hand, AGN that feature narrower emission lines have shallower decrements, as well as a BP which is not characteristic of PLTE. Taking into account the sources, where at least a reasonable fit could be achieved, our results point towards the determination of lower temperatures in objects with broader emission lines.

However, the interpretation of BP in terms of intrinsic thermodynamical properties of the source is not straightforward. The line flux ratios, from which we compute the normalized intensity for the BP, might be affected by some amount of extinction, resulting in a stronger decrement in the flux of the high order emission lines of the Balmer series, with respect to the low order ones. While such an effect can influence the temperature estimate of a BP, that would be lower than the real value, it is very unlikely that the shape of the plot could mimic a PLTE, if the plasma has not at least some component in this condition. The relation among the BP temperature parameter  $A$  and the line profile widths in the spectra, therefore, points towards a difference in the ionization conditions within the BLR of objects with unequal line broadening. Objects with relatively narrow emission lines are more frequently associated to poor fits in the BP or they show shallower decrements in the Balmer series than broad line emitting sources.

On the basis of the BP analysis, we try to investigate the role played by the ionizing radiation field in determining the thermodynamical properties of the BLR. Our study of emission lines and optical continuum properties allowed us to provide preliminary estimates of the continuum source luminosities and to compare them with the predictions of different simple BLR structural models. By means of this test, we found that the differences observed in the ionization conditions of the BLR plasma could be related to the properties of the SMBH, combining especially its mass and accretion rate. The extreme simplification of these models, however, which deal with the BLR velocity field in terms of an isotropic distribution of virial motions, cannot be directly applied to the sources, because it is unlikely to be realistic and it would introduce a strong dependence of the estimated properties on

the line profile widths.

In order to understand in greater detail the role played by those properties of the central engine, which control the ionization conditions of the BLR through the continuum radiation, we need to improve our understanding of the BLR structure, taking into account the role of its geometry and of its kinematical components. The simple analysis, so far performed on parametric information concerning the broad line profiles, is not able to provide the advanced indications that we need in this field. A major achievement in the interpretation of the role played by the central engine, therefore, would come from a more detailed study of the BLR kinematics from the emission line profiles, which is fundamental for the construction of realistic dynamical models. The possibility to perform this kind of investigation on the Balmer series and the final considerations about the inferred properties of the central engine are the topics of the next chapter.

Table 5.1: Emission Line Fluxes

Object Name	F(H $\beta$ )	$R_\epsilon$	$R_\delta$	$R_\gamma$	$R_\alpha$	F([O III])
LBQS 0010+0035	1210 $\pm$ 108	ND	0.239 $\pm$ 0.044	0.417 $\pm$ 0.054	3.476 $\pm$ 0.330	237 $\pm$ 25
2MASX J00133540-0951213	427 $\pm$ 54	ND	0.239 $\pm$ 0.048	0.511 $\pm$ 0.081	3.890 $\pm$ 0.543	872 $\pm$ 63
2MASS J00372354+0008122	1054 $\pm$ 95	0.089 $\pm$ 0.017	0.208 $\pm$ 0.031	0.388 $\pm$ 0.062	3.388 $\pm$ 0.358	632 $\pm$ 65
2MASX J00423686-1049222	740 $\pm$ 87	ND	0.242 $\pm$ 0.046	0.485 $\pm$ 0.095	4.335 $\pm$ 0.556	637 $\pm$ 50
SDSS J010712.03+140844.9	954 $\pm$ 72	0.105 $\pm$ 0.026	0.208 $\pm$ 0.035	0.445 $\pm$ 0.061	3.397 $\pm$ 0.300	242 $\pm$ 22
2MASX J01100897-1008434	5856 $\pm$ 452	0.105 $\pm$ 0.021	0.212 $\pm$ 0.032	0.428 $\pm$ 0.050	3.689 $\pm$ 0.306	3154 $\pm$ 126
2MASSI J0112549+000313	702 $\pm$ 82	ND	0.279 $\pm$ 0.063	0.405 $\pm$ 0.080	4.040 $\pm$ 0.548	611 $\pm$ 16
SDSS J011703.58+000027.4	956 $\pm$ 40	0.135 $\pm$ 0.040	0.268 $\pm$ 0.038	0.442 $\pm$ 0.035	3.218 $\pm$ 0.172	1194 $\pm$ 35
QSO B0119-013	1860 $\pm$ 137	ND	0.263 $\pm$ 0.041	0.401 $\pm$ 0.050	2.385 $\pm$ 0.233	334 $\pm$ 50
2MASX J01352783-0044477	4053 $\pm$ 227	0.057 $\pm$ 0.013	0.197 $\pm$ 0.029	0.421 $\pm$ 0.041	3.400 $\pm$ 0.234	771 $\pm$ 60
QSO B0137-010	1315 $\pm$ 100	ND	0.204 $\pm$ 0.049	0.408 $\pm$ 0.062	2.621 $\pm$ 0.250	473 $\pm$ 45
2MASX J01423843+0005145	345 $\pm$ 37	ND	0.371 $\pm$ 0.090	0.652 $\pm$ 0.128	2.959 $\pm$ 0.369	233 $\pm$ 13
2MASX J01424828-1008402	16431 $\pm$ 788	ND	0.219 $\pm$ 0.030	0.530 $\pm$ 0.059	3.894 $\pm$ 0.217	14866 $\pm$ 536
SDSS J015046.68+132359.9	4297 $\pm$ 379	ND	0.182 $\pm$ 0.033	0.299 $\pm$ 0.050	4.175 $\pm$ 0.408	2272 $\pm$ 80
2MASX J01591007+0105148	935 $\pm$ 100	ND	0.205 $\pm$ 0.048	0.406 $\pm$ 0.070	3.598 $\pm$ 0.425	296 $\pm$ 22
2MASS J02333539-0107446	1067 $\pm$ 87	ND	0.203 $\pm$ 0.039	0.420 $\pm$ 0.048	3.632 $\pm$ 0.343	663 $\pm$ 33
2MASS J02500703+0025251	940 $\pm$ 65	ND	0.319 $\pm$ 0.056	0.619 $\pm$ 0.080	3.617 $\pm$ 0.281	613 $\pm$ 37
LBQS 0254+0101	964 $\pm$ 82	ND	0.211 $\pm$ 0.038	0.462 $\pm$ 0.059	3.535 $\pm$ 0.319	129 $\pm$ 21
2MASX J03041778+0028274	618 $\pm$ 67	ND	0.272 $\pm$ 0.055	0.521 $\pm$ 0.088	2.108 $\pm$ 0.267	174 $\pm$ 24
2MASX J03063958+0003426	496 $\pm$ 94	ND	0.381 $\pm$ 0.107	0.448 $\pm$ 0.112	3.139 $\pm$ 0.631	138 $\pm$ 8
LBQS 0307-0101	1953 $\pm$ 113	ND	0.091 $\pm$ 0.018	0.290 $\pm$ 0.030	2.806 $\pm$ 0.211	293 $\pm$ 33
2MASS J03221390+0055134	564 $\pm$ 68	ND	0.236 $\pm$ 0.050	0.484 $\pm$ 0.084	4.216 $\pm$ 0.557	408 $\pm$ 50

Object Name	F(H $\beta$ )	$R_\epsilon$	$R_\delta$	$R_\gamma$	$R_\alpha$	F([O III])
2MASS J03233765+0035555	5994 $\pm$ 288	0.081 $\pm$ 0.011	0.208 $\pm$ 0.022	0.416 $\pm$ 0.038	3.185 $\pm$ 0.177	1729 $\pm$ 222
2MASX J03510759-0526370	7617 $\pm$ 454	0.122 $\pm$ 0.017	0.251 $\pm$ 0.028	0.471 $\pm$ 0.059	2.422 $\pm$ 0.182	6649 $\pm$ 310
2MASX J04092918-0429021	4767 $\pm$ 310	ND	0.177 $\pm$ 0.025	0.366 $\pm$ 0.049	3.352 $\pm$ 0.260	1385 $\pm$ 42
RX J0752.8+2617	487 $\pm$ 84	ND	0.329 $\pm$ 0.100	0.437 $\pm$ 0.116	2.614 $\pm$ 0.501	295 $\pm$ 24
QSO B0752+393	2868 $\pm$ 290	0.143 $\pm$ 0.035	0.422 $\pm$ 0.070	0.529 $\pm$ 0.083	2.679 $\pm$ 0.303	1914 $\pm$ 63
SDSS J083045.36+340532.1	4102 $\pm$ 265	ND	0.245 $\pm$ 0.036	0.462 $\pm$ 0.065	3.995 $\pm$ 0.290	1582 $\pm$ 92
SDSS J083202.16+461425.8	2902 $\pm$ 217	0.098 $\pm$ 0.022	0.275 $\pm$ 0.043	0.424 $\pm$ 0.054	3.663 $\pm$ 0.300	1388 $\pm$ 54
2MASX J08394965+4847014	10536 $\pm$ 588	ND	0.214 $\pm$ 0.037	0.409 $\pm$ 0.046	3.646 $\pm$ 0.210	1164 $\pm$ 41
SDSS J084025.51+033301.7	938 $\pm$ 73	ND	0.231 $\pm$ 0.038	0.461 $\pm$ 0.058	3.725 $\pm$ 0.325	439 $\pm$ 19
2MASX J08550420+5252477	991 $\pm$ 122	ND	0.225 $\pm$ 0.052	0.494 $\pm$ 0.100	3.860 $\pm$ 0.507	430 $\pm$ 42
2MASX J08573780+0528211	959 $\pm$ 127	ND	0.522 $\pm$ 0.133	0.775 $\pm$ 0.174	3.897 $\pm$ 0.551	1127 $\pm$ 52
2MASX J09043699+5536025	699 $\pm$ 120	ND	0.243 $\pm$ 0.061	0.489 $\pm$ 0.123	3.552 $\pm$ 0.632	862 $\pm$ 24
SDSS J092554.25+533558.2	406 $\pm$ 50	ND	0.638 $\pm$ 0.150	0.741 $\pm$ 0.144	3.222 $\pm$ 0.483	416 $\pm$ 22
QSO B0934+013	1684 $\pm$ 92	ND	0.258 $\pm$ 0.039	0.550 $\pm$ 0.050	3.469 $\pm$ 0.221	1352 $\pm$ 76
LBQS 1008+0058	2334 $\pm$ 139	0.107 $\pm$ 0.000	0.204 $\pm$ 0.020	0.448 $\pm$ 0.043	3.702 $\pm$ 0.284	1731 $\pm$ 64
2MASS J10131485-0052338	2300 $\pm$ 114	ND	0.150 $\pm$ 0.026	0.388 $\pm$ 0.051	1.562 $\pm$ 0.088	417 $\pm$ 54
1WGA J1016.7+4210	5835 $\pm$ 497	0.097 $\pm$ 0.016	0.361 $\pm$ 0.061	0.456 $\pm$ 0.073	2.557 $\pm$ 0.278	1497 $\pm$ 198
Mrk 142	2045 $\pm$ 133	ND	0.300 $\pm$ 0.041	0.421 $\pm$ 0.045	3.636 $\pm$ 0.300	2349 $\pm$ 68
2MASX J10425297+0414413	755 $\pm$ 71	ND	0.223 $\pm$ 0.051	0.615 $\pm$ 0.093	3.746 $\pm$ 0.395	1037 $\pm$ 66
2MASX J10570691-0041446	1087 $\pm$ 76	ND	0.365 $\pm$ 0.066	0.566 $\pm$ 0.043	2.764 $\pm$ 0.231	357 $\pm$ 29
2MASS J10593576-0005513	934 $\pm$ 86	ND	0.219 $\pm$ 0.037	0.458 $\pm$ 0.089	2.256 $\pm$ 0.231	162 $\pm$ 32
2MASX J11050361+0745313	1610 $\pm$ 186	ND	0.219 $\pm$ 0.062	0.348 $\pm$ 0.063	3.798 $\pm$ 0.469	589 $\pm$ 25
MCG+10-16-111	10103 $\pm$ 594	ND	0.271 $\pm$ 0.036	0.480 $\pm$ 0.055	4.121 $\pm$ 0.277	7199 $\pm$ 279

Object Name	F(H $\beta$ )	$R_\epsilon$	$R_\delta$	$R_\gamma$	$R_\alpha$	F([O III])
2MASX J11220940+0117199	1791 $\pm$ 115	ND	0.223 $\pm$ 0.039	0.452 $\pm$ 0.055	3.678 $\pm$ 0.316	2470 $\pm$ 69
SDSS J112813.02+102308.3	2622 $\pm$ 262	ND	0.317 $\pm$ 0.076	0.518 $\pm$ 0.075	3.916 $\pm$ 0.454	2644 $\pm$ 208
2MASX J11390898+5911547	1654 $\pm$ 160	0.164 $\pm$ 0.047	0.284 $\pm$ 0.055	0.586 $\pm$ 0.094	2.563 $\pm$ 0.309	887 $\pm$ 52
2MASX J11410569+0241173	1109 $\pm$ 285	ND	0.279 $\pm$ 0.113	0.581 $\pm$ 0.179	3.027 $\pm$ 0.803	377 $\pm$ 13
LBQS 1150+0010	859 $\pm$ 79	0.205 $\pm$ 0.059	0.251 $\pm$ 0.054	0.438 $\pm$ 0.084	2.021 $\pm$ 0.198	332 $\pm$ 48
2MASS J11574174+0412506	2188 $\pm$ 195	0.134 $\pm$ 0.023	0.269 $\pm$ 0.064	0.442 $\pm$ 0.082	3.359 $\pm$ 0.311	739 $\pm$ 111
2MASS J11575874-0022208	5477 $\pm$ 177	ND	0.112 $\pm$ 0.020	0.322 $\pm$ 0.043	2.959 $\pm$ 0.129	990 $\pm$ 48
2MASX J12033294+0229346	3719 $\pm$ 270	0.122 $\pm$ 0.017	0.200 $\pm$ 0.028	0.424 $\pm$ 0.043	3.167 $\pm$ 0.241	501 $\pm$ 80
Mrk 50	870 $\pm$ 97	ND	0.248 $\pm$ 0.059	0.549 $\pm$ 0.093	3.659 $\pm$ 0.428	987 $\pm$ 40
2MASX J12431998+0252562	738 $\pm$ 51	ND	0.202 $\pm$ 0.029	0.453 $\pm$ 0.063	3.488 $\pm$ 0.277	132 $\pm$ 24
LBQS 1244+0238	3619 $\pm$ 160	ND	0.286 $\pm$ 0.035	0.519 $\pm$ 0.040	3.288 $\pm$ 0.170	1982 $\pm$ 73
Mrk 236	2488 $\pm$ 128	ND	0.301 $\pm$ 0.052	0.496 $\pm$ 0.057	3.933 $\pm$ 0.270	1105 $\pm$ 54
2MASX J13005216+5641056	1731 $\pm$ 146	ND	0.254 $\pm$ 0.056	0.453 $\pm$ 0.059	3.590 $\pm$ 0.321	1088 $\pm$ 43
2MASS J13071325-0036018	1204 $\pm$ 80	0.081 $\pm$ 0.022	0.224 $\pm$ 0.034	0.408 $\pm$ 0.050	2.792 $\pm$ 0.201	537 $\pm$ 35
2MASS J13075656+0107097	1956 $\pm$ 109	0.062 $\pm$ 0.012	0.229 $\pm$ 0.037	0.398 $\pm$ 0.043	4.509 $\pm$ 0.397	1389 $\pm$ 56
1WGA J1331.6+0131	2753 $\pm$ 268	0.172 $\pm$ 0.034	0.388 $\pm$ 0.076	0.396 $\pm$ 0.062	2.396 $\pm$ 0.262	2120 $\pm$ 269
LBQS 1338-0038	1433 $\pm$ 99	0.110 $\pm$ 0.020	0.227 $\pm$ 0.033	0.394 $\pm$ 0.050	3.465 $\pm$ 0.300	1174 $\pm$ 42
2MASX J13421004+5642106	903 $\pm$ 78	ND	0.197 $\pm$ 0.046	0.477 $\pm$ 0.079	3.470 $\pm$ 0.338	155 $\pm$ 13
LBQS 1340-0038	840 $\pm$ 90	ND	0.271 $\pm$ 0.055	0.490 $\pm$ 0.073	4.004 $\pm$ 0.474	355 $\pm$ 25
SDSS J134351.07+000434.8	1269 $\pm$ 122	0.138 $\pm$ 0.030	0.341 $\pm$ 0.058	0.520 $\pm$ 0.070	3.228 $\pm$ 0.358	462 $\pm$ 53
2MASX J13442643+4416194	2292 $\pm$ 238	ND	0.386 $\pm$ 0.076	0.417 $\pm$ 0.077	2.110 $\pm$ 0.241	512 $\pm$ 81
SDSS J134452.91+000520.2	1912 $\pm$ 103	ND	0.106 $\pm$ 0.024	0.318 $\pm$ 0.036	3.528 $\pm$ 0.221	428 $\pm$ 31
LBQS 1342-0000	1577 $\pm$ 136	0.138 $\pm$ 0.027	0.340 $\pm$ 0.050	0.494 $\pm$ 0.054	2.478 $\pm$ 0.840	406 $\pm$ 117

Object Name	F(H $\beta$ )	$R_\epsilon$	$R_\delta$	$R_\gamma$	$R_\alpha$	F([O III])
2MASS J13452470-0259396	3518 $\pm$ 243	ND	0.314 $\pm$ 0.040	0.474 $\pm$ 0.053	2.938 $\pm$ 0.227	1317 $\pm$ 46
2MASX J13495283+0204456	3930 $\pm$ 220	ND	0.217 $\pm$ 0.034	0.412 $\pm$ 0.063	4.869 $\pm$ 0.303	8162 $\pm$ 260
SDSS J135542.76+644045.0	4383 $\pm$ 352	0.130 $\pm$ 0.021	0.319 $\pm$ 0.053	0.473 $\pm$ 0.060	2.649 $\pm$ 0.228	2483 $\pm$ 163
LBQS 1434+0020	1321 $\pm$ 87	0.123 $\pm$ 0.020	0.220 $\pm$ 0.022	0.500 $\pm$ 0.059	3.075 $\pm$ 0.245	335 $\pm$ 43
Mrk 1392	1348 $\pm$ 144	0.142 $\pm$ 0.037	0.433 $\pm$ 0.080	0.578 $\pm$ 0.102	3.266 $\pm$ 0.381	1202 $\pm$ 29
2MASX J15102489+0058438	10659 $\pm$ 695	ND	0.225 $\pm$ 0.028	0.380 $\pm$ 0.045	3.997 $\pm$ 0.308	15250 $\pm$ 377
2MASX J15192168+5908239	1596 $\pm$ 131	0.127 $\pm$ 0.027	0.321 $\pm$ 0.067	0.502 $\pm$ 0.075	2.939 $\pm$ 0.263	416 $\pm$ 72
2MASX J15195659+0016149	1306 $\pm$ 133	ND	0.245 $\pm$ 0.061	0.429 $\pm$ 0.050	3.612 $\pm$ 0.452	392 $\pm$ 27
QSO B1534+580	1658 $\pm$ 122	ND	0.230 $\pm$ 0.042	0.393 $\pm$ 0.050	3.445 $\pm$ 0.279	238 $\pm$ 25
SDSS J153830.78+444038.5	1212 $\pm$ 90	ND	0.282 $\pm$ 0.047	0.447 $\pm$ 0.066	2.957 $\pm$ 0.247	1017 $\pm$ 30
2MASX J15541741+3238381	3053 $\pm$ 283	ND	0.286 $\pm$ 0.056	0.401 $\pm$ 0.071	4.783 $\pm$ 0.464	3065 $\pm$ 116
MCG+06-36-003	1797 $\pm$ 193	ND	0.237 $\pm$ 0.051	0.420 $\pm$ 0.059	4.122 $\pm$ 0.484	528 $\pm$ 17
SDSS J161951.31+405847.2	2609 $\pm$ 164	ND	0.297 $\pm$ 0.048	0.520 $\pm$ 0.075	4.404 $\pm$ 0.313	6830 $\pm$ 293
Mrk 699	6033 $\pm$ 481	0.091 $\pm$ 0.022	0.280 $\pm$ 0.048	0.402 $\pm$ 0.055	2.307 $\pm$ 0.200	1254 $\pm$ 186
2E 1652.4+3930	2396 $\pm$ 178	ND	0.281 $\pm$ 0.069	0.474 $\pm$ 0.074	3.881 $\pm$ 0.318	3564 $\pm$ 131
2MASS J16595894+6202181	1440 $\pm$ 101	ND	0.249 $\pm$ 0.044	0.408 $\pm$ 0.053	3.099 $\pm$ 0.244	149 $\pm$ 27
QSO B1717+5818	1906 $\pm$ 144	ND	0.201 $\pm$ 0.043	0.402 $\pm$ 0.067	2.272 $\pm$ 0.220	521 $\pm$ 49
2MASS J17190229+5937159	5646 $\pm$ 297	ND	0.130 $\pm$ 0.016	0.366 $\pm$ 0.042	4.360 $\pm$ 0.344	1955 $\pm$ 144
2MASS J17202672+5540243	3722 $\pm$ 253	ND	0.240 $\pm$ 0.042	0.404 $\pm$ 0.042	3.538 $\pm$ 0.258	5491 $\pm$ 213
SDSS J205822.14-065004.3	1116 $\pm$ 191	ND	0.202 $\pm$ 0.056	0.385 $\pm$ 0.101	2.571 $\pm$ 0.480	296 $\pm$ 30
2MASS J23493277-0036458	1837 $\pm$ 176	ND	0.337 $\pm$ 0.061	0.543 $\pm$ 0.081	3.051 $\pm$ 0.328	519 $\pm$ 45
SDSS J235156.12-010913.3	522 $\pm$ 52	ND	0.261 $\pm$ 0.040	0.473 $\pm$ 0.085	3.063 $\pm$ 0.353	186 $\pm$ 17

Note – Fluxes are expressed in units of  $10^{-17}$  erg cm $^{-2}$  s $^{-1}$  Å $^{-1}$

Table 5.2: Calculated Spectral Properties

Object Name	$\text{FWHM}_{\text{H}\beta}$	FWZI	$L_{5100}$	$R_{\text{BLR}}$	$A$	Class
LBQS 0010+0035	$4163 \pm 234$	$10573 \pm 1458$	$12804 \pm 106$	$654 \pm 64$	$0.313 \pm 0.009$	ii
2MASX J00133540-0951213	$1122 \pm 113$	$5951 \pm 1632$	$386 \pm 17$	$113 \pm 13$	$0.301 \pm 0.043$	ii
2MASS J00372354+0008122	$2608 \pm 179$	$8524 \pm 2044$	$27783 \pm 494$	$963 \pm 99$	$0.380 \pm 0.044$	i
2MASX J00423686-1049222	$2272 \pm 123$	$7478 \pm 1355$	$389 \pm 8$	$114 \pm 12$	$0.391 \pm 0.037$	ii
SDSS J010712.03+140844.9	$2214 \pm 122$	$8956 \pm 1661$	$5676 \pm 139$	$435 \pm 46$	$0.319 \pm 0.026$	i
2MASX J01100897-1008434	$2808 \pm 216$	$10537 \pm 1261$	$5319 \pm 46$	$421 \pm 42$	$0.352 \pm 0.020$	i
2MASS J0112549+000313	$2218 \pm 117$	$8591 \pm 2372$	$416 \pm 5$	$118 \pm 12$	$0.138 \pm 0.038$	iv
SDSS J011703.58+000027.4	$2571 \pm 243$	$8610 \pm 1831$	$3358 \pm 153$	$335 \pm 39$	$0.242 \pm 0.014$	i
QSO B0119-013	$3253 \pm 101$	$9969 \pm 1480$	$43986 \pm 273$	$1211 \pm 118$	$0.119 \pm 0.046$	iv
2MASX J01352783-0044477	$5586 \pm 379$	$12992 \pm 1813$	$84506 \pm 1418$	$1679 \pm 172$	$0.340 \pm 0.060$	iii
QSO B0137-010	$2621 \pm 97$	$9068 \pm 1374$	$2295 \pm 33$	$277 \pm 28$	$0.177 \pm 0.049$	iv
2MASX J01423843+0005145	$1142 \pm 53$	$5568 \pm 1203$	$173 \pm 8$	$76 \pm 9$	$0.122 \pm 0.059$	iv
2MASX J01424828-1008402	$4266 \pm 150$	$12344 \pm 2467$	$2011 \pm 31$	$259 \pm 26$	$0.346 \pm 0.041$	ii
SDSS J015046.68+132359.9	$4846 \pm 410$	$14046 \pm 3127$	$878 \pm 13$	$171 \pm 17$	$0.486 \pm 0.041$	ii
2MASX J01591007+0105148	$3077 \pm 201$	$9978 \pm 2151$	$3736 \pm 65$	$353 \pm 36$	$0.350 \pm 0.012$	ii
2MASS J02333539-0107446	$3330 \pm 291$	$9277 \pm 1278$	$2613 \pm 50$	$295 \pm 31$	$0.337 \pm 0.013$	ii
2MASS J02500703+0025251	$1453 \pm 33$	$6686 \pm 1400$	$207 \pm 7$	$83 \pm 9$	$0.247 \pm 0.070$	iii
LBQS 0254+0101	$3504 \pm 98$	$8969 \pm 1945$	$676 \pm 18$	$150 \pm 16$	$0.308 \pm 0.023$	ii
2MASX J03041778+0028274	$2922 \pm 157$	$8149 \pm 1091$	$12096 \pm 185$	$635 \pm 65$	$-0.017 \pm 0.028$	iv
2MASX J03063958+0003426	$1474 \pm 185$	$7004 \pm 1460$	$314 \pm 13$	$102 \pm 12$	$0.206 \pm 0.069$	iv
LBQS 0307-0101	$4372 \pm 128$	$10846 \pm 1882$	$5701 \pm 114$	$436 \pm 45$	$0.332 \pm 0.129$	iv
2MASS J03221390+0055134	$2005 \pm 112$	$6805 \pm 1110$	$644 \pm 22$	$147 \pm 16$	$0.374 \pm 0.033$	ii

Object Name	$\text{FWHM}_{\text{H}\beta}$	FWZI	$L_{5100}$	$R_{\text{BLR}}$	$A$	Class
2MASS J03233765+0035555	$2356 \pm 115$	$9902 \pm 1747$	$31883 \pm 238$	$1031 \pm 101$	$0.307 \pm 0.046$	i
2MASX J03510759-0526370	$2563 \pm 162$	$8176 \pm 1738$	$3162 \pm 72$	$325 \pm 34$	$0.131 \pm 0.036$	iv
2MASX J04092918-0429021	$3181 \pm 154$	$9837 \pm 1301$	$4192 \pm 42$	$374 \pm 37$	$0.343 \pm 0.041$	ii
RX J0752.8+2617	$2009 \pm 119$	$7978 \pm 1915$	$639 \pm 17$	$146 \pm 16$	$0.158 \pm 0.034$	iv
QSO B0752+393	$1697 \pm 111$	$7686 \pm 1003$	$788 \pm 9$	$162 \pm 16$	$0.077 \pm 0.062$	iv
SDSS J083045.36+340532.1	$5460 \pm 239$	$13492 \pm 1879$	$2187 \pm 55$	$270 \pm 29$	$0.360 \pm 0.026$	ii
SDSS J083202.16+461425.8	$2199 \pm 176$	$10423 \pm 1518$	$787 \pm 16$	$162 \pm 17$	$0.330 \pm 0.037$	i
2MASX J08394965+4847014	$5526 \pm 179$	$14898 \pm 3208$	$786 \pm 13$	$162 \pm 17$	$0.342 \pm 0.007$	ii
SDSS J084025.51+033301.7	$4227 \pm 234$	$9804 \pm 1742$	$457 \pm 6$	$123 \pm 12$	$0.330 \pm 0.019$	ii
2MASX J08550420+5252477	$1736 \pm 48$	$6162 \pm 1113$	$581 \pm 23$	$139 \pm 16$	$0.354 \pm 0.028$	ii
2MASX J08573780+0528211	$2359 \pm 140$	$7423 \pm 1429$	$264 \pm 2$	$94 \pm 9$	$0.193 \pm 0.119$	iv
2MASX J09043699+5536025	$2483 \pm 163$	$6940 \pm 1361$	$109 \pm 1$	$60 \pm 6$	$0.308 \pm 0.022$	ii
SDSS J092554.25+533558.2	$1532 \pm 131$	$5811 \pm 1291$	$544 \pm 7$	$135 \pm 14$	$0.048 \pm 0.137$	iv
QSO B0934+013	$2258 \pm 57$	$7719 \pm 1285$	$1445 \pm 53$	$220 \pm 25$	$0.235 \pm 0.050$	iii
LBQS 1008+0058	$2806 \pm 94$	$8138 \pm 1723$	$6408 \pm 298$	$462 \pm 54$	$0.353 \pm 0.026$	i
2MASS J10131485-0052338	$6816 \pm 164$	$11309 \pm 1542$	$32469 \pm 359$	$1041 \pm 104$	$-0.109 \pm 0.121$	iv
1WGA J1016.7+4210	$1845 \pm 130$	$9904 \pm 2052$	$1411 \pm 43$	$217 \pm 24$	$0.167 \pm 0.093$	iv
Mrk 142	$1845 \pm 226$	$9883 \pm 1104$	$942 \pm 8$	$177 \pm 17$	$0.302 \pm 0.055$	ii
2MASX J10425297+0414413	$2082 \pm 95$	$7751 \pm 1499$	$741 \pm 17$	$157 \pm 17$	$0.276 \pm 0.073$	ii
2MASX J10570691-0041446	$2370 \pm 78$	$8870 \pm 2027$	$528 \pm 13$	$133 \pm 14$	$0.069 \pm 0.027$	iv
2MASS J10593576-0005513	$2674 \pm 174$	$9662 \pm 1278$	$9233 \pm 112$	$555 \pm 56$	$0.103 \pm 0.046$	iv
2MASX J11050361+0745313	$5268 \pm 262$	$15224 \pm 2513$	$783 \pm 18$	$162 \pm 17$	$0.416 \pm 0.023$	ii
MCG+10-16-111	$4107 \pm 104$	$12589 \pm 2159$	$2500 \pm 74$	$289 \pm 31$	$0.358 \pm 0.042$	ii
2MASX J11220940+0117199	$1534 \pm 164$	$7596 \pm 1698$	$494 \pm 8$	$128 \pm 13$	$0.326 \pm 0.013$	ii

Object Name	$\text{FWHM}_{\text{H}\beta}$	FWZI	$L_{5100}$	$R_{\text{BLR}}$	$A$	Class
SDSS J112813.02+102308.3	$1244 \pm 88$	$6968 \pm 1366$	$1094 \pm 28$	$191 \pm 20$	$0.299 \pm 0.049$	ii
2MASX J11390898+5911547	$2459 \pm 137$	$8101 \pm 1995$	$1560 \pm 14$	$228 \pm 22$	$0.086 \pm 0.035$	iv
2MASX J11410569+0241173	$2114 \pm 263$	$8755 \pm 2906$	$337 \pm 3$	$106 \pm 10$	$0.163 \pm 0.054$	iv
LBQS 1150+0010	$2693 \pm 92$	$7488 \pm 1375$	$7788 \pm 272$	$510 \pm 57$	$0.032 \pm 0.034$	iv
2MASS J11574174+0412506	$1522 \pm 93$	$7755 \pm 1910$	$1461 \pm 67$	$221 \pm 26$	$0.287 \pm 0.006$	i
2MASS J11575874-0022208	$5662 \pm 214$	$13711 \pm 2510$	$14086 \pm 326$	$685 \pm 72$	$0.263 \pm 0.084$	iv
2MASX J12033294+0229346	$2963 \pm 129$	$10524 \pm 1714$	$3599 \pm 24$	$347 \pm 34$	$0.285 \pm 0.016$	i
Mrk 50	$2521 \pm 94$	$7832 \pm 1657$	$815 \pm 11$	$165 \pm 17$	$0.279 \pm 0.042$	ii
2MASX J12431998+0252562	$1168 \pm 66$	$5511 \pm 1239$	$431 \pm 23$	$120 \pm 15$	$0.322 \pm 0.021$	ii
LBQS 1244+0238	$2782 \pm 159$	$9034 \pm 1683$	$4544 \pm 32$	$389 \pm 38$	$0.217 \pm 0.036$	iv
Mrk 236	$4644 \pm 239$	$11765 \pm 1589$	$925 \pm 10$	$176 \pm 17$	$0.335 \pm 0.053$	ii
2MASX J13005216+5641056	$2104 \pm 170$	$9338 \pm 1766$	$1398 \pm 21$	$216 \pm 22$	$0.309 \pm 0.012$	ii
2MASS J13071325-0036018	$2556 \pm 105$	$9077 \pm 1663$	$4884 \pm 53$	$404 \pm 40$	$0.219 \pm 0.039$	iii
2MASS J13075656+0107097	$4890 \pm 231$	$15868 \pm 2613$	$18328 \pm 267$	$782 \pm 79$	$0.489 \pm 0.073$	i
1WGA J1331.6+0131	$1569 \pm 79$	$7615 \pm 1448$	$1105 \pm 44$	$192 \pm 22$	$0.086 \pm 0.053$	iv
LBQS 1338-0038	$2300 \pm 94$	$8993 \pm 1537$	$3202 \pm 64$	$327 \pm 34$	$0.329 \pm 0.023$	i
2MASX J13421004+5642106	$2676 \pm 112$	$8311 \pm 1699$	$499 \pm 7$	$129 \pm 13$	$0.305 \pm 0.033$	ii
LBQS 1340-0038	$4301 \pm 146$	$10310 \pm 1888$	$2361 \pm 14$	$281 \pm 27$	$0.328 \pm 0.036$	ii
SDSS J134351.07+000434.8	$1873 \pm 151$	$8801 \pm 2287$	$2502 \pm 42$	$289 \pm 30$	$0.243 \pm 0.029$	ii
2MASX J13442643+4416194	$1372 \pm 63$	$8145 \pm 2017$	$830 \pm 18$	$166 \pm 18$	$0.002 \pm 0.063$	iv
SDSS J134452.91+000520.2	$5717 \pm 135$	$14506 \pm 2272$	$11300 \pm 211$	$614 \pm 64$	$0.394 \pm 0.081$	iii
LBQS 1342-0000	$2086 \pm 103$	$7648 \pm 2218$	$3036 \pm 42$	$318 \pm 32$	$0.197 \pm 0.046$	iv
2MASS J13452470-0259396	$3097 \pm 205$	$11282 \pm 1869$	$439 \pm 3$	$121 \pm 12$	$0.161 \pm 0.031$	iv
2MASX J13495283+0204456	$2990 \pm 681$	$9396 \pm 1882$	$248 \pm 11$	$91 \pm 11$	$0.506 \pm 0.023$	ii

Object Name	$\text{FWHM}_{\text{H}\beta}$	FWZI	$L_{5100}$	$R_{\text{BLR}}$	$A$	Class
SDSS J135542.76+644045.0	$1527 \pm 98$	$7214 \pm 1614$	$914 \pm 34$	$175 \pm 20$	$0.151 \pm 0.031$	iv
LBQS 1434+0020	$2278 \pm 76$	$8744 \pm 1467$	$7476 \pm 79$	$499 \pm 50$	$0.360 \pm 0.039$	i
Mrk 1392	$1400 \pm 122$	$7570 \pm 1644$	$798 \pm 12$	$163 \pm 17$	$0.162 \pm 0.066$	iv
2MASX J15102489+0058438	$4906 \pm 266$	$11785 \pm 2483$	$2163 \pm 35$	$269 \pm 27$	$0.400 \pm 0.027$	ii
2MASX J15192168+5908239	$1278 \pm 109$	$6936 \pm 1521$	$795 \pm 30$	$163 \pm 18$	$0.202 \pm 0.030$	iv
2MASX J15195659+0016149	$4387 \pm 171$	$10600 \pm 1802$	$10002 \pm 165$	$578 \pm 59$	$0.321 \pm 0.016$	ii
QSO B1534+580	$3834 \pm 322$	$10655 \pm 1295$	$1230 \pm 9$	$203 \pm 20$	$0.318 \pm 0.015$	ii
SDSS J153830.78+444038.5	$3242 \pm 188$	$8706 \pm 1439$	$379 \pm 3$	$112 \pm 11$	$0.201 \pm 0.016$	iv
2MASX J15541741+3238381	$5312 \pm 382$	$10818 \pm 1375$	$1746 \pm 29$	$241 \pm 25$	$0.466 \pm 0.056$	ii
MCG+06-36-003	$4789 \pm 217$	$11267 \pm 1272$	$927 \pm 10$	$176 \pm 17$	$0.396 \pm 0.018$	ii
SDSS J161951.31+405847.2	$2436 \pm 92$	$8016 \pm 2087$	$788 \pm 17$	$162 \pm 17$	$0.393 \pm 0.063$	ii
Mrk 699	$2402 \pm 207$	$7030 \pm 1450$	$360 \pm 9$	$110 \pm 12$	$0.123 \pm 0.056$	iv
2E 1652.4+3930	$3990 \pm 122$	$9829 \pm 1132$	$21004 \pm 234$	$837 \pm 83$	$0.351 \pm 0.025$	ii
2MASS J16595894+6202181	$1586 \pm 67$	$8242 \pm 1964$	$1586 \pm 37$	$230 \pm 24$	$0.259 \pm 0.019$	ii
QSO B1717+5818	$3292 \pm 159$	$9966 \pm 1622$	$20876 \pm 227$	$835 \pm 83$	$0.110 \pm 0.069$	iv
2MASS J17190229+5937159	$4973 \pm 216$	$20280 \pm 3400$	$13749 \pm 519$	$677 \pm 77$	$0.530 \pm 0.075$	ii
2MASS J17202672+5540243	$3469 \pm 244$	$10064 \pm 1750$	$1996 \pm 20$	$258 \pm 26$	$0.332 \pm 0.011$	ii
SDSS J205822.14-065004.3	$2058 \pm 109$	$8580 \pm 1663$	$415 \pm 10$	$118 \pm 12$	$0.232 \pm 0.043$	iv
2MASS J23493277-0036458	$2749 \pm 69$	$8662 \pm 1328$	$213 \pm 10$	$84 \pm 10$	$0.153 \pm 0.038$	iv
SDSS J235156.12-010913.3	$3062 \pm 153$	$9042 \pm 1614$	$6475 \pm 43$	$465 \pm 45$	$0.211 \pm 0.009$	iv

Note – FWHM and FWZI are expressed in units of  $\text{km s}^{-1}$

$L_{5100}$  is given in  $10^{40} \text{ erg s}^{-1}$

$R_{\text{BLR}}$  is in  $10^{14} \text{ cm}$

Table 5.3: Electron Temperatures Estimated from the BP of Objects Belonging to Class i and ii

Object Name	$T_e$ (K)	Object Name	$T_e$ (K)	Object Name	$T_e$ (K)
LBQS 0010+0035	$16000 \pm 1000$	SDSS J084025.51+033301.7	$15000 \pm 3000$	2MASX J13421004+5642106	$17000 \pm 5000$
2MASX J00133540-0951213	$17000 \pm 7000$	2MASX J08550420+5252477	$14000 \pm 3000$	LBQS 1340-0038	$15000 \pm 5000$
2MASS J00372354+0008122	$13000 \pm 5000$	2MASX J09043699+5536025	$16000 \pm 4000$	SDSS J134351.07+000434.8	$21000 \pm 7000$
2MASX J00423686-1049222	$13000 \pm 4000$	LBQS 1008+0058	$14000 \pm 3000$	2MASX J13495283+0204456	$10000 \pm 1000$
SDSS J010712.03+140844.9	$16000 \pm 4000$	Mrk 142	$17000 \pm 9000$	LBQS 1434+0020	$14000 \pm 5000$
2MASX J01100897-1008434	$14000 \pm 2000$	2MASX J10425297+0414413	$18000 \pm 15000$	2MASX J15102489+0058438	$13000 \pm 3000$
SDSS J011703.58+000027.4	$21000 \pm 4000$	2MASX J11050361+0745313	$12000 \pm 2000$	2MASX J15195659+0016149	$16000 \pm 2000$
2MASX J01424828-1008402	$15000 \pm 5000$	MCG+10-16-111	$14000 \pm 5000$	QSO B1534+580	$16000 \pm 2000$
SDSS J015046.68+132359.9	$10000 \pm 3000$	2MASX J11220940+0117199	$16000 \pm 2000$	2MASX J15541741+3238381	$11000 \pm 4000$
2MASX J01591007+0105148	$14000 \pm 1000$	SDSS J112813.02+102308.3	$17000 \pm 8000$	MCG+06-36-003	$13000 \pm 2000$
2MASS J02333539-0107446	$15000 \pm 2000$	2MASX J12033294+0229346	$18000 \pm 3000$	SDSS J161951.31+405847.2	$13000 \pm 6000$
LBQS 0254+0101	$16000 \pm 4000$	Mrk 50	$18000 \pm 8000$	2E 1652.4+3930	$14000 \pm 3000$
2MASS J03221390+0055134	$14000 \pm 4000$	2MASX J12431998+0252562	$16000 \pm 3000$	2MASS J16595894+6202181	$20000 \pm 4000$
2MASX J04092918-0429021	$15000 \pm 5000$	Mrk 236	$15000 \pm 7000$	2MASS J17190229+5937159	$10000 \pm 4000$
SDSS J083045.36+340532.1	$14000 \pm 3000$	2MASX J13005216+5641056	$16000 \pm 2000$	2MASS J17202672+5540243	$15000 \pm 2000$
SDSS J083202.16+461425.8	$15000 \pm 5000$	2MASS J13075656+0107097	$10000 \pm 5000$		
2MASX J08394965+4847014	$15000 \pm 1000$	LBQS 1338-0038	$15000 \pm 3000$		

# Chapter 6

## BLR Gas Kinematics

### 6.1 Introduction

The simplified structural BLR models, that we introduced in the previous chapter, suggested that the relations among the gas velocity field and its thermodynamical properties, as estimated from the BP, are both influenced by the physical processes which occur in the central continuum source. During the past years, a lot of work has been devoted to understand the relationship between the BLR dynamics and the corresponding broad emission line profiles (Capriotti et al. 1980, 1981; Ferland et al. 1992; Peterson & Wandel 1999; Korista & Goad 2004, 2005), but, while the former is probably very complex, often with evidence for multiple components (Popović et al. 2004), the latter is the result of a combination of effects involving the gas motion pattern and the radiation transfer across an environment which is only approximately understood. Although many important achievements have been obtained in the angular resolution of AGN cores at radio wavelengths (e. g. Kellerman et al. 1998), the actual distribution of the broad line emitting medium is still matter of debate.

Using the RM results, which provide a reliable way to constrain the volume where the nuclear activity is confined (e. g. Wandel et al. 1999; Peterson & Wandel 2000; Peterson et al. 2004), the simple mass estimate of Eq. (5.12)

can be written in the form of:

$$M_{BH} = f \cdot \frac{R_{BLR} \text{FWHM}^2}{G}, \quad (6.1)$$

where  $f$  represents a geometrical factor, accounting for the unknown distribution of the line emitting material, while the FWHM is taken from the profile of a fairly well recognized broad emission line. The role played by  $f$  was carefully investigated in several works (see, for instance, Vestergaard et al. 2000; Nikolaĭjuk et al. 2005; Marziani et al. 2006; Decarli et al. 2008a), which compared different methods to estimate the mass and the dynamical influence of the central engine. What is commonly found is that the assumption of a simple parameter, such as the FWHM of an emission line, to represent the gas kinematical properties is highly uncertain, if the geometry is not properly taken into account.

In this chapter we describe the results we obtained by studying the kinematical properties of the BLR gas with a technique based on the analysis of the total line profile, which exploits the cross-correlation method and the Gauss-Hermite profile fitting to infer the line broadening function (BF) in the optical domain. We developed this method on the AGN spectra selected in the Véron-Cetty Catalogue and extracted from the SDSS database. We show that some interesting clues to the geometry of the BLR can be identified in this way and we apply the results to estimate the SMBH properties in the whole sample of AGN, that we collected. This chapter is organized as follows: in § 6.2 we describe the analytical formalism to extract the profile broadening functions and to calculate the corresponding Gauss-Hermite expansions; in § 6.3 we present the reduction techniques that we adopted; § 6.4 introduces our BLR model, with a discussion of the main limits and some indications to improve the analysis; finally we discuss our results in § 6.5.

## 6.2 Theoretical Line Profiles

In the effort towards revealing the intrinsic properties of AGN cores, line profile analysis often played a major role. Under specific assumptions about

the dynamical conditions within the BLR, such as the hypothesis of virial motions driven by the combined effect of the central engine's gravity and radiation pressure, a number of representative parameters, like the line widths at different intensity levels, or the line asymmetry factors, usually computed in the form of ratios among the line extension toward the blue and red wavelengths, with respect to the line core position, were used in order to describe the profiles and to evaluate the properties of the engine. This kind of approach is prone to the effects of the substantially unknown BLR geometry, with the possibility to introduce systematic misinterpretation of data. Furthermore, it assumes quite specific measurements to be a good approximation of the entire emission line profile, losing some precious physical details.

In this section we describe a generalized approach to the line profile fitting, already exploited in the past years in the field of advanced stellar kinematics, but adopted for gas kinematics as well (Barton et al. 2000).

### 6.2.1 Emission Line Broadening from Cross-Correlation

There are indications, in the BLR spectrum, that the distribution of the line emitting material may be different, according to the ionization potential of the considered emission lines (see e. g. Gaskell & Sparke 1986; Sulentic et al. 1995; Marziani et al. 1996; Snedden & Gaskell 2004; Matsuoka et al. 2008; Mullaney & Ward 2008; Sluse et al. 2008, etc.). Indeed, the interaction of the most energetic AGN radiation with gas probably produces a region where matter is highly ionized. On the contrary, optical shielding effects allow for the survival of low ionization species, in regions where only comparatively low energy photons may penetrate. Therefore, if the BLR structure is such that the shielded component is different from the directly exposed one, the properties of the emission lines will depend on their ionization potential.

On the other hand, choosing to analyze a set of emission lines belonging to a statistical distribution of matter and radiation interactions, it is more likely that the emission regions are not dramatically different. In the optical domain, the Balmer series of hydrogen is the most appropriate choice,

because of its strength above the underlying continuum.

Assuming that the Balmer line emission is not affected by large variations across the BLR and introducing the cross-correlation formalism, originally described by Tonry & Davis (1979) and then updated by Statler (1995), we can approximate the observed line spectra as the convolution of an appropriate template of narrow emission lines  $T(x)$ , each one representing a single emitting unit, with the BLR kinematical broadening function  $B(x)$ :

$$S(x) \simeq T(x) * B(x), \quad (6.2)$$

where  $S(x)$  is the observed spectrum, while  $x$  represents a logarithmic wavelength coordinate of the form:

$$x = A \ln \lambda + B, \quad (6.3)$$

such that the effect of radial velocities results in linear shifts along  $x$ . Eq. (6.2) can be explicitly written as:

$$S(x) \simeq \int T(x)B(x - x') dx' \quad (6.4)$$

and, if we compute the cross-correlation function of the spectrum with the template, we find:

$$X(x) = S(x) \otimes T(x) = \int S(x)T(x + x') dx'. \quad (6.5)$$

Using Eq. (6.4), the cross-correlation function becomes:

$$X(x) \simeq \int \int T(x)B(x - x'') dx''T(x + x') dx', \quad (6.6)$$

which, upon changing order of integration, is:

$$X(x) \simeq \int \int T(x)T(x + x') dx' B(x - x'') dx''. \quad (6.7)$$

Based on the definitions of cross-correlation and convolution, Eq. (6.7) approximates the cross-correlation function of the spectrum and the template as the convolution of the template autocorrelation function with the object's BF (Statler 1995):

$$X(x) \simeq [T(x) \otimes T(x)] * B(x). \quad (6.8)$$

Since  $T(x)$  is known and  $X(x)$  is drawn from observations, as far as the template is correct, it is possible to recover  $B(x)$ .

Restricting our analysis to the primary cross-correlation peak, which carries most of the kinematical information and it is weakly affected by template mismatch, Eq. (6.7) can be written in its discrete form, with the simplified notation  $F_i = F(x_i)$ :

$$X_k \simeq \sum_{i=0}^N \left( \sum_{j=0}^N T_i T_{i+j} \right) B_{k-i}. \quad (6.9)$$

Provided that all the functions are null when they are computed outside the range  $0 \leq i \leq N$ , Eq. (6.9) defines a system of  $N + 1$  linear equations in the  $N + 1$  variables  $B_{k-i}$  ( $k \geq i$ ). A standard  $\chi^2$ -minimization routine can be therefore used to infer the BF of the Balmer lines.

### 6.2.2 Analytical expressions for the broadening functions

As previously mentioned, the BLR broadening functions are influenced by the effects of complex kinematics within the source and of radiation transfer from the source to the observer. For this reason it is hardly conceivable that a simple analytic expression might be used to fit the resulting profiles. In the case of a geometrically complex distribution of motions in the line emitting region, multiple Gaussian functions provide reasonable fits to the observed profiles. Two Gaussian contributions can usually fit the broad component of  $H\beta$  (Popović et al. 2004; Chen et al. 2008), but other contributions, up to five more Gaussians, might be needed to account for the narrow emission lines of  $H\beta$  and [O III]. Furthermore, the presence of ordered kinematical components modifies the shape of the BF, raising non-Gaussian features in the profiles.

A good way to estimate the importance of non-Gaussian components is to parameterize the observed BF by means of a Gauss-Hermite orthonormal expansion, similarly to what is described in Van Der Marel & Franx (1993) for

the case of stellar kinematics in elliptical galaxies. Following their method, if we call  $\alpha(v)$  the normal Gaussian function:

$$\alpha(v) = \frac{1}{\sqrt{2\pi}\sigma_v} \exp\left(-\frac{v^2}{2\sigma_v^2}\right), \quad (6.10)$$

where  $\sigma_v$  is the line of sight velocity dispersion, the emission line BF can be expressed as a function of  $v$  :

$$B(v) = B_0\alpha(v - V_{sys}) \left[ 1 + \sum_{i=3}^N h_i H_i(v - V_{sys}) \right], \quad (6.11)$$

in which we call  $B_0$  the BF normalization factor,  $V_{sys}$  the systemic radial velocity offset between the BF and the chosen reference frame,  $H_i(v - V_{sys})$  the  $i^{\text{th}}$  order Hermite polynomial, and  $h_i$  the corresponding coefficient. A wide description of the properties of the Hermite polynomials is given in Van Der Marel & Franx (1993). It is demonstrated that odd order functions account for asymmetric distortions of the Gaussian profile, while even order functions have a symmetric effect. Truncating Eq. (6.11) to  $N = 4$ , the Hermite polynomials are expressed by:

$$H_3(y) = \frac{1}{\sqrt{6}}(2\sqrt{2}y^3 - 3\sqrt{2}y) \quad (6.12a)$$

$$H_4(y) = \frac{1}{\sqrt{24}}(4y^4 - 12y^2 + 3). \quad (6.12b)$$

Therefore, it is possible to estimate the role of non-Gaussian kinematical components, using the whole BF profile, simply by fitting the observed shape with a truncated Gauss-Hermite series and measuring the appropriate values of  $h_3$  and  $h_4$ .

## 6.3 Spectral Analysis

### 6.3.1 The Balmer Line Broadening Functions

Following the application of the preliminary reduction procedures, described in Chapter 4, we have got a new set of BLR Balmer line spectra. Our task is

then to recover their BF, by means of the cross-correlation technique outlined in § 6.2.1. To calculate the cross-correlation functions, we build a template of Balmer emission lines, following the median line intensity ratios presented in Chapter 5 (see also La Mura et al. 2007) for the first selection of our AGN sample. Our template assumes that the SDSS instrumental profile is a Gaussian function with  $\text{FWHM} = 167 \text{ km s}^{-1}$ . At the spectral resolution of SDSS data, the logarithmic sampling of the wavelength coordinate can be performed with discrete bins corresponding to  $69 \text{ km s}^{-1}$  each. Here we use the *IRAF* task `fxcor` to compute the template autocorrelation function:

$$A(x) = T(x) \otimes T(x) \quad (6.14)$$

and the cross-correlation functions of the BLR spectra with the template, following the definition of Eq. (6.5). Again a  $\chi^2$ -minimization algorithm can be exploited to infer the BF in its discrete form. Applying the least squares formalism to the equation system (6.9), it follows that the BF of each spectrum must satisfy the relations:

$$\sum_{i=0}^N B_i \left( \sum_{j=0}^N A_j A_{i-k} \right) = \sum_{i=k}^N A_{i-k} X_i. \quad (6.15)$$

In principle, it is possible to extract an accurate solution for the BF by solving the equation system (6.15) with  $0 \leq k \leq N$ . In practice the task is not simple, because it involves the inversion of a coefficient matrix as large as  $[(N+1) \times (N+1)]$ , with  $N$  increasing with the line profile widths up to  $N \simeq 400$ . However, the complete solution of such a system is not the real purpose of this work, since we are not seeking the detailed shape of the BF, but we are rather looking for the importance of non-Gaussian components. Therefore, we chose to solve the system at lower resolution, interpolating the BF every 8 bins with an analytical profile, which we assumed to be a Gauss-Hermite expansion.

We compared the properties inferred for the BF of our spectra with the results obtained by applying the Gauss-Hermite profile fitting directly to the  $\text{H}\beta$  emission line. We found that the expansion coefficients in the two cases

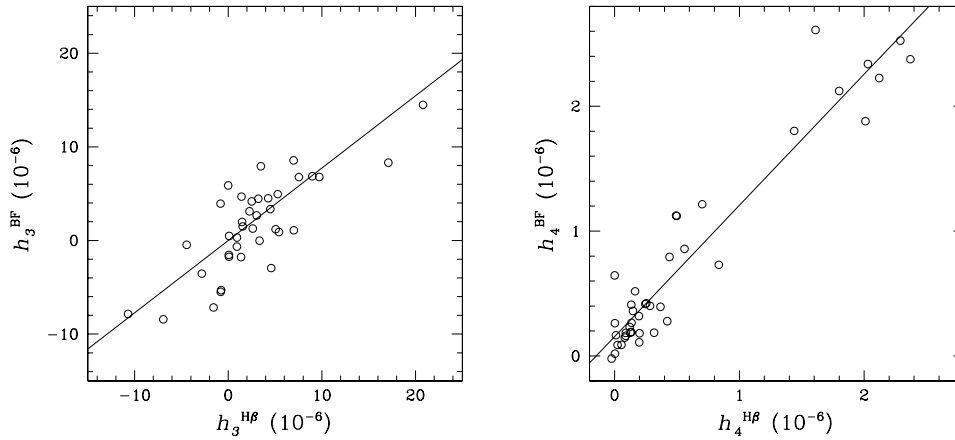


Figure 6.1: Gauss-Hermite expansion coefficients of the line profile BF compared with the corresponding ones in the profile of  $H\beta$ . The straight lines, shown in each panel, are the best fit functions described in Eq. (6.16) and Eq. (6.17).

are highly correlated, supporting a tight relationship among the  $H\beta$  emission line profile and the BF of the Balmer series. The details of this comparison are given in Fig. 6.1, where we plot the values of the expansion coefficients obtained in both ways. As a result, we get:

$$h_3^{\text{BF}} = (0.773 \pm 0.073)h_3^{\text{H}\beta} + (0.721 \pm 0.554) \cdot 10^{-6}, \quad (6.16)$$

with a correlation coefficient  $R = 0.865$  and a null hypothesis  $P_0 < 10^{-6}$  and

$$h_4^{\text{BF}} = (1.051 \pm 0.052)h_4^{\text{H}\beta} + (0.154 \pm 0.049) \cdot 10^{-6}, \quad (6.17)$$

with  $R = 0.955$  and  $P_0 < 10^{-6}$ .

Here we would like to point out that the matrix inversion must be computed only once, because it involves coefficients exclusively drawn from the template autocorrelation function. The cross-correlation functions of the spectra, instead, only affect the known terms of Eq. (6.15). Hence the advantage of this technique.

### 6.3.2 Emission Line Widths and Continuum Luminosity

After the calculation of the BF of our sample, we performed more measurements of spectral properties in the data, estimating, in particular, the FWHM of the  $H\beta$  emission line and the AGN continuum radiation luminosity at 5100 Å. These are needed to infer some of the source physical properties, such as the central black hole mass, its accretion rate, and the size of the BLR.

In the case of the line profile measurements, we looked at the  $H\beta$  emission line in the BLR spectra, which we previously isolated for cross-correlation with the template. To account for the uncertain continuum and narrow line corrections, we applied the same technique, used in the corresponding measurements onto the spectra of our first sub-sample: we performed five different measurements of the line half width at half the maximum both on the blue and red wing of the line, varying our guess to the continuum and line peak intensity; we combined these estimates to calculate the FWHM, then we averaged them together, and we computed the  $1\sigma$  dispersion. As a further step, we reproduced the broad  $H\beta$  profile with two Gaussian functions and we applied the same measurements to the identified components.

Following the same analogy with the procedures described in § 5.3, we measured the AGN optical continuum luminosities at 5100 Å. Here, the main source of error arises from the noise fluctuations around the actual signal intensity. For this reason, we assumed the specific continuum luminosity at 5100 Å to be represented by the average luminosity, evaluated in the range running from 5075 Å to 5125 Å, and the associated error to be given by its standard deviation. Therefore, we measured the continuum fluxes of our spectra and we computed the related specific luminosities using the object redshift as a distance indicator, in the framework of the cosmological model defined by  $H_0 = 75 \text{ km s}^{-1} \text{ Mpc}^{-1}$ ,  $\Omega_{matter} = 0.3$ , and  $\Omega_\Lambda = 0.7$ . Our guess to the bolometric luminosity, which is needed to infer the accretion rate onto the

central black hole, can be made from the specific luminosity measurements:

$$L_{bol} \simeq 10 \cdot (5100 \text{ \AA} \cdot L_{5100}) \quad (6.18)$$

(e. g. Elvis et al. 1994; but see also Collin et al. 2002; Collin & Kawaguchi 2004, and references therein), where  $L_{5100}$  represents our estimate to the continuum specific luminosity at 5100 Å, given in  $\text{erg s}^{-1} \text{ \AA}^{-1}$ , and  $L_{bol}$  is the bolometric luminosity, in units of  $\text{erg s}^{-1}$ . We note, however, that this assumption is prone to the effect of the large dispersion in the SED of AGN and it may easily introduce an uncertainty of a factor  $\sim 2$ , which propagates in the estimated black hole masses and accretion rates.

## 6.4 The BLR Structural Models

A clear determination of the black hole mass is not possible unless we are able to discriminate the role played by  $f$  in Eq. (6.1). In many circumstances, the black hole mass problem is dealt with through the assumption of a particular geometry, such as a random distribution of virial motions (Netzer 1990; Wandel et al. 1999; Peterson & Wandel 2000), or a flattened rotating system with an inclination mostly inferred by means of statistical considerations (Decarli et al. 2008a). The very nature of the broad line emitting entities has been investigated extensively (see, for example, Arav et al. 1997, 1998; Laor 2006), leading to the conclusion that the broad line profiles either result from the combination of a large number of emitters, in the order of  $\sim 10^7$ , or it is produced by motions of a smooth medium. In both cases, it is noticed that a random motion pattern could not be dynamically stable.

With the exception of those objects whose line profiles clearly show double peaks, a strong clue towards an highly inclined rotating system, the BLR inclination is still an open question of crucial importance for determination of black hole mass and accretion rate. Indeed, the assumption of a universal geometrical factor usually leads to the detection of high accretion rates in NLS1 galaxies, while adjusting the geometrical factor, according to statistics,

affects the black hole masses largely reducing most of the differences. Both these paths might be sources of systematic misunderstandings, therefore a direct and independent measurement of the BLR inclination, or, alternatively, of the black hole accretion rate, would be highly desirable in order to discriminate among the actual dynamical properties and the effect of inclination (Kelly et al. 2008). A similar test has been performed, for a restricted sample, by Hicks & Malkan (2008) in near infrared spectroscopic observations, leading to the conclusion that the observed gas kinematics is consistent with RM based results for nearly face-on disk structures.

### 6.4.1 Inclination and line profile broadening

Since the BLR structure cannot be represented by a random motion pattern, we can expect the shape of the broad emission lines to exhibit large deviations from the Gaussian profile. In the extreme case of the marked double peaks in the spectral lines of Arp 102B, a peculiar source studied by Chen & Halpern (1989), the BLR structure is well explained in terms of the combination of a quasi spherical component with a rotating disk, probably the external accretion disk, seen at an inclination of  $i = 32^\circ$ . Popović et al. (2004) applied the same model to other single peaked line emitting sources and they found that mildly inclined disks could be responsible for the observed line profiles as well, although uncertainties on the model free parameters might affect the values of the inferred inclinations, as Collin et al. (2006) pointed out.

If the BLR has a flattened component which is seen at low inclination, its emission lines clearly do not exhibit double peaks, but the geometrical structure still modifies the dynamical interpretation of data. We illustrate this concept in Fig. 6.2, where we plot the expected FWHM in the broadening function of disks surrounding black holes of increasing mass and we compare it to the situation of a black hole of fixed mass, but with the disk seen under different inclinations. It is clear that, within the range of our calculations, there is a mass - inclination degeneracy on the resulting FWHM.

Exploiting the model developed in Chen et al. (1989), Chen & Halpern

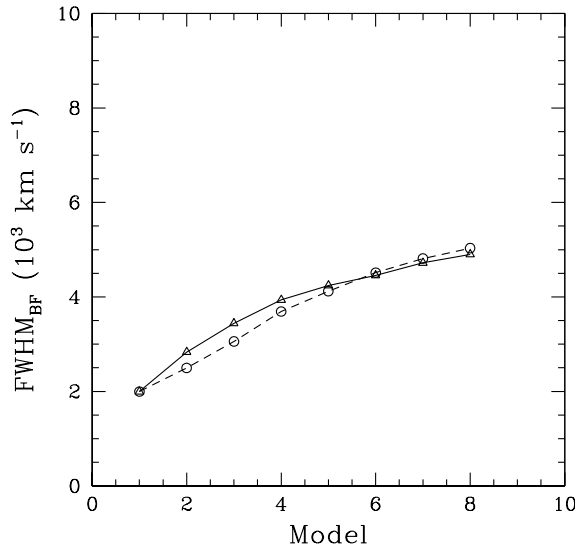


Figure 6.2: Expected FWHM in the BF of emission lines originated in a disk structure. The empty triangles, connected by the continuous line are the predicted values for reference disk models with  $i = 10^\circ$ , in the gravitational field of SMBH with  $M = 1, 2, 4, 6, 8, 10,$  and  $14 \cdot 10^7 M_\odot$  (respectively, models from 1 to 8); the circles with the dashed line show the predicted behaviour for the reference disk model in the gravitational field of the SMBH with  $M = 10^7 M_\odot$ , when seen under inclinations of  $i = 10^\circ, 15^\circ, 20^\circ, 25^\circ, 30^\circ, 35^\circ, 40^\circ,$  and  $45^\circ$  (again from model 1 to 8).

(1989), and Popović et al. (2004), we computed a range of expected non-Gaussian profiles in the case of a two-component BLR structure seen at different inclinations, with a flattened rotating disk and a surrounding distribution of gas, giving rise to a bell-shaped contribution. In its original purpose, this model was conceived to fit the properties of an accretion disk, introducing some free parameters for the disk radii, intrinsic velocity dispersion, and line emission. Adjusting these parameters, it would be possible to fit the broad emission line profiles of possibly all the spectra of our sample,

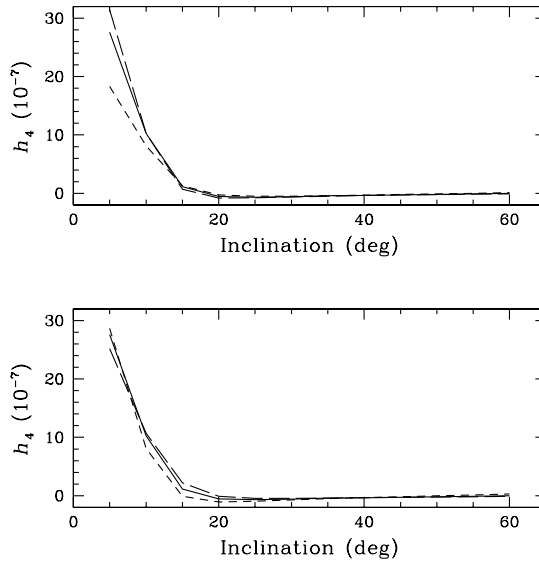


Figure 6.3: Comparison of the reference model predictions, concerning the BF kurtosis (continuous line), with four variants: in the upper panel we plot models with stronger (long dashed line) and weaker (short dashed line) disk emission, with respect to the surrounding gas contribution; in the bottom panel we show the differences obtained by setting  $\sigma_{Bell} = 0.07 c$  (short dashed line) and  $\sigma_{Bell} = 0.09 c$  (long dashed line).

but reasonable fits can be obtained in several ways, without tightly constraining the physical properties of the BLR. Here we try to predict the effect of a flattened BLR component on the observed line profiles, therefore we fix some of these parameters on the basis of the results collected by La Mura et al. (2007). Our reference model assumes  $R_{in} = 1834 R_S$  for inner radius,  $R_{BLR} = 18340 R_S$  for outer radius,  $\sigma_{Disk} = 0.003 c$  as the intrinsic velocity dispersion in the disk, and  $\alpha = -2.0$  for the radial emission power law, where  $R_S$  and  $c$  represent the Schwarzschild radius and the speed of light. Moreover, this model includes a surrounding gas distribution having a velocity dispersion of  $\sigma_{Bell} = 0.008 c$ . The reference model carries out the best match

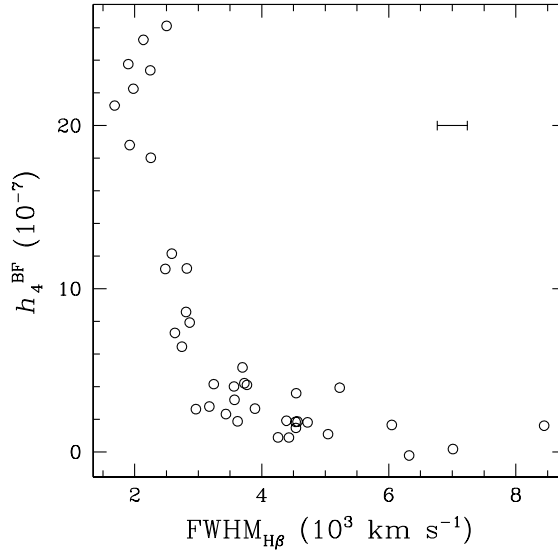


Figure 6.4: BF kurtosis plotted as a function of  $\text{FWHM}_{\text{H}\beta}$ . We observe a large evolution of the line profile kurtosis, depending on the line profile broadening, which agrees with the predicted effects of inclination in nearly face-on flattened structures. The effect is weaker in objects with broader emission lines.

to the observed line profiles with the assumption of various disk inclinations.

In Fig. 6.3, we compare the reference model with some variants, obtained with slightly different parameters. We note that all the models predict a strong dependence of the line profile kurtosis (the coefficient  $h_4$  in the Gauss-Hermite expansion) on the disk inclination, in the range of small values of  $i$ . The reason is quite simple, because a nearly face-on disk enhances the low radial velocity peak of the BF, increasing the kurtosis of the profile, while an edge-on disk is more likely to affect the high velocity wings. However, differences in the relative normalization of the bell-shaped component, with respect to the disk, or in its intrinsic velocity dispersion, may also affect the inferred kurtosis. The assumed strength of the bell-shaped component has a large effect on the predicted kurtosis for  $i \leq 10^\circ$ , while its velocity

dispersion has a weaker influence in the range  $10^\circ \leq i \leq 20^\circ$ . Since large changes in the model parameters quickly result in predictions that do not match the observed line profiles, we assume, in our calculations, a confidential uncertainty of  $\Delta i = \pm 2^\circ$ , for  $i \leq 10^\circ$ , and of  $\Delta i = \pm 5^\circ$ , for  $i > 10^\circ$ , where the dependence of kurtosis on inclination becomes shallower. At  $i \geq 20^\circ$  the kurtosis is no longer a useful indicator of inclination.

As we show in Fig. 6.4, however, where we plot the measured values of  $h_4$  as a function of  $\text{FWHM}_{\text{H}\beta}$ , there is a remarkable evolution of the line profile kurtosis, which decreases for increasing line profile width. Such an effect is a clear indication that a considerable variation of the geometrical factor  $f$  might be present and it should be taken into account in order to estimate the actual properties of the SMBH located in the centre. Using the model predictions, we can exploit the broad line kurtosis to estimate the inclination of the flattened BLR component and to apply a correction to our dynamical interpretation of the observed line profiles. It should be noted, however, that, although the kurtosis is estimated from the whole profile, it reduces the available information to a single parameter. It is, therefore, very important that the model provides a good fit of the observed line profiles.

## 6.4.2 Mass and accretion rate estimates

It can be shown that completely neglecting the role played by the BLR geometrical factor may lead to incorrect black hole mass estimates, with uncertainties that, in the worst cases, could span over two orders of magnitude. This problem is particularly important in the case of NLS1 galaxies, whose nature has been carefully investigated, to find out whether they are characterized by flattened rotating structures seen at low inclination (Osterbrock & Pogge 1985), or they are actually low mass black holes accreting at very high rates, sometimes well beyond the Eddington limit, as it is discussed, for instance, by Boller et al. (1996) and Komossa (2008). Moreover, the role played by non gravitational forces, especially in the case of high radiative efficiency, may also influence the kinematical properties of gas, as suggested

by Marconi et al. (2008), affecting the reliability of the virial assumption. In their work, La Mura et al. (2007) found that, although NLS1 had quite high accretion rates, they were not exceptional with respect to other AGN in the sample, a result echoed by the considerations of Decarli et al. (2008a).

On the other hand, while Shemmer et al. (2006) argue that X-ray observations may provide a direct clue to the black hole accretion rate and thus remove the degeneracy introduced by the  $\text{FWHM}_{\text{H}\beta}$  dependent mass estimates, Decarli et al. (2008b) and Labita et al. (2006) use the black hole correlations with the host properties, identified by Ferrarese et al. (2000, 2006), to calibrate the geometrical factor. Both methods suggest that some care should be taken in using only the profile width of  $\text{H}\beta$  to infer the physical properties of AGN.

With the information coming from the line profile distortions, we compute our estimates of the black hole mass and accretion rate by introducing an *equivalent velocity field*, defined by:

$$v_{eq} = \frac{1}{2} \left[ \frac{\sqrt{3}}{2} \text{FWHM}_{Bell}(\text{H}\beta) + \frac{\text{FWHM}_{Disk}(\text{H}\beta)}{4 \sin i} \right]. \quad (6.19)$$

Assuming that the line profile broadening results from both planar and non-planar motions (Labita et al. 2006; McLure et al. 2002; Jarvis & McLure 2006, etc.),  $v_{eq}$  combines the velocity estimates obtained from the  $\text{H}\beta$  emission line profile by fitting two Gaussian functions, which are subsequently compared with the reference model, providing a distinction among the bell-shaped and the flattened contributions. The corresponding geometrical factors are assumed to be, respectively, the classical interpretation of Netzer (1990) and that of a rotating disk, confined in a smaller region with respect to the other component. The inclination of the disk is estimated by comparison of the BF kurtosis with that of the reference model, as shown in Fig. 6.5, and its characteristic radius is assumed to be approximately four times smaller than the typical size of the surrounding gas distribution. To calculate the black hole mass, we introduce  $v_{eq}$  in Eq. (6.1), bringing the geometrical factor into the modified velocity field, and we estimate the cor-

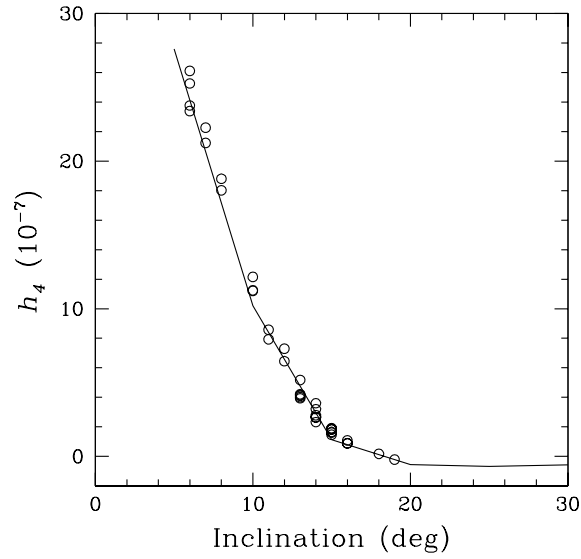


Figure 6.5: BLR inclination inferred by comparison among the BF kurtosis, predicted by the reference model for various inclinations, and the corresponding distribution observed in the sample.

responding Eddington ratio from the bolometric luminosity in Eq. (6.18).

The results of our measurements and calculations, concerning this subsample, are summarized in Table 6.1, together with the computed uncertainty ranges, while in Table 6.2 we report the properties of the remaining objects. Our method breaks the strong dependence of the black hole accretion rate and mass estimates on the width of  $H\beta$  since it exploits more indications, coming from the broadening functions of the observed Balmer lines. Moreover, the typical inclinations inferred for the BLR of our spectra are consistent with those estimated by Popović et al. (2008), suggesting that this situation is quite common in single peaked broad line emitters. The tables, however, do not include the errors which could be introduced by our assumptions, concerning the source luminosity and the BLR structure. Such uncertainties may be as large as a factor of 2 or 3, as seen in the AGN SED distribution, or

by adopting different structural models for the BLR. We shall further discuss the role of these uncertainties with the help of some consistency checks.

## 6.5 Discussion

While our estimates of bolometric luminosity and, consequently, black hole mass and accretion rate are essentially scaled by our measurement of the optical continuum luminosity, the dynamical interpretation of the line profiles still suffers from undeniable shortcomings. Adopting a two-component model to explain the line profile broadening complicates the relationship among  $\text{FWHM}_{\text{H}\beta}$  and the black hole mass, introducing a geometrical factor which depends on the inclination of the flattened component and on its relative importance with respect to the BLR as a whole. Because disks are the most viable solution to support accretion flows in presence of angular momentum, numerous authors suggested that the broad line gas could originate in the disks themselves (e. g. Shields 1977; Shlosman et al. 1985; Emmering et al. 1992). Models based on accretion disks only, however, have great difficulties in accounting for AGN observational properties (see Kinney 1994, for example). The assumption of a two-component model improves our ability to understand the observed line profiles, but it still fails in placing strong constraints on the structure of the BLR, since the origin of the bell-shaped component is not clear. Indeed, there are models, such as those of Collin-Souffrin & Dumont (1990), Jackson et al. (1991), Murray & Chiang (1997), which achieve a good match with observations on more physical grounds, either exploiting very large disk radii, or computing the effect of radiation transfer across radial gas flows close to the disk. Clearly, the choice of different models affects the interpretation of AGN dynamical properties and this is a major concern in the case of the BLR.

A particularly important problem, involving the determination of AGN physical properties from emission lines, resides in the line profile asymmetries. Several factors, such as partial obscuration, geometrical structure, or large

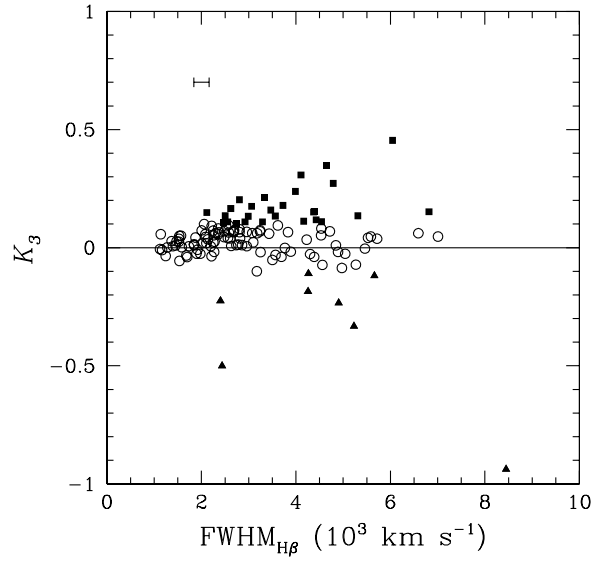


Figure 6.6:  $\text{H}\beta$  asymmetry parameter distribution vs.  $\text{FWHM}_{\text{H}\beta}$ . Filled symbols represent objects where the asymmetric component exceeds 10% of the Gaussian contribution. We plot as triangles objects that are affected by negative asymmetry, yielding blue shifted peaks and red shifted wings, while we use squares to represent positive asymmetry sources, with a redshifted peak and blue shifted wings. Large asymmetries characterize objects where fits with the reference model are more likely to be problematic. The bar in the upper left region of the diagram is a median estimate of the measurement errors.

scale non-virialized motions can produce asymmetric line profiles. Moreover, relativistic effects within the gravitational field of the SMBH give rise to asymmetries, especially in the high velocity wings of the profile, which are included in the calculations of the model by Chen & Halpern (1989). In order to assess how much the asymmetric components affect our estimates of the velocity field, we introduced an asymmetry parameter:

$$K_3 = h_3 H_3(\text{FWHM}_{\text{H}\beta}), \quad (6.20)$$

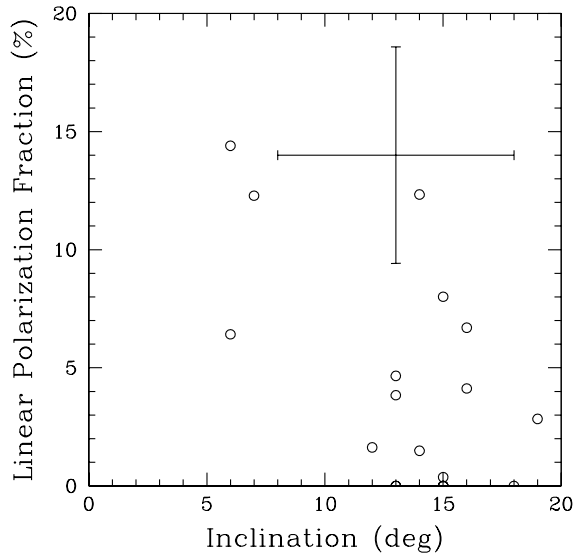


Figure 6.7: Degree of linear polarization, detected by the VLA FIRST survey at the radio frequency of 1.4 GHz, compared with the inferred BLR inclination. The cross in the upper left corner of the diagram is the median uncertainty estimate.

expressing the relative contribution of the asymmetric component, with respect to the Gaussian component, in the profile of  $H\beta$  at its half-maximum level. As we show in Fig. 6.6, the asymmetric component gives a contribution to the FWHM which rarely exceeds the 10% level. The most extreme cases, where the asymmetric component becomes larger than 20%, occur only in the range of broad line emitting sources. Although this does not appear to be a general property of broad line objects, it echoes the observation of larger asymmetries in objects where  $\text{FWHM}_{H\beta} > 4000 \text{ km s}^{-1}$ , which is among the features identified by Sulentic et al. (2000a, 2006) in their distinction between Population A and B sources. Objects with the largest asymmetries are more problematic in their comparison with the reference model, used to calculate the equivalent velocity field in the BLR.

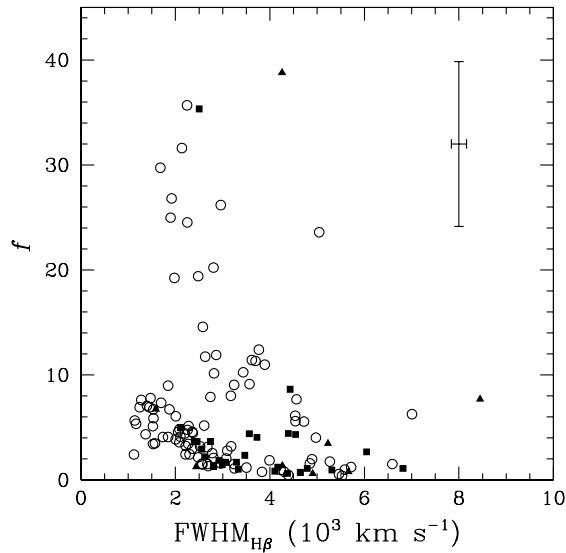


Figure 6.8: Geometrical factors obtained by comparing the virial product of Eq. (6.1) with our black hole mass estimates. Symbols are the same as in Fig. 6.6. The effect of the geometrical factor is generally stronger as the line profile width decreases, with a correction to the black hole mass estimate, which can be as high as a factor of  $\sim 40$ .

Most of the results achieved in this work, therefore, depend critically on the choice of our reference model, which leads us to conclude that the BLR has a flattened component, that is commonly seen at  $i \leq 20^\circ$ . In the case of radio-loud sources, nearly face-on disk structures are likely to produce a radio jet oriented along our line of sight towards the object, and the resulting signal should be highly variable and polarized. Although we were not able to find any information about variability, some of the radio loud sources in our sample have been detected in the NRAO VLA Sky Survey (NVSS), which provides measurements of the radio flux and polarization at the frequency of 1.4 GHz (Condon et al. 1998).<sup>1</sup> These objects were identified in Table 4.2

<sup>1</sup>Polarization data are available at <http://www.cv.nrao.edu/nvss/NVSSlist.shtml>

and a plot of the reported degree of linear polarization with our inclination estimates is illustrated in Fig. 6.7. Although the uncertainties are quite large, a significant degree of linear polarization is detected in many objects and it appears to be an averagely decreasing function of  $i$ .

A comparison of our mass determinations with the simple isotropic assumption allows us to study the properties of the geometrical factor within our sample. The situation depicted in Fig. 6.8 clearly indicates that significant effects, up to a factor  $\sim 40$ , should be expected and that they are more commonly observed in the range of sources with  $\text{FWHM}_{\text{H}\beta} \leq 3000 - 4000 \text{ km s}^{-1}$ . We find that the average value of the geometrical factor for black hole mass determinations based on  $\text{FWHM}_{\text{H}\beta}$  is  $f = 6.51$ , in fairly good agreement with the result achieved by Onken et al. (2004), who gave  $f = 5.5 \pm 1.9$  using the emission line dispersions.

Table 6.1: Estimated Properties of the Kinematical Sample

Object Name	$\text{FWHM}_{\text{H}\beta}$	$L_{5100}$	$h_3$	$h_4$	$i$	$v_{eq}$	$K_3$	$M_{BH}$	$L_{bol}/L_{Edd}$
RX J0801.5+4736	$7009 \pm 336$	$20 \pm 1$	3.1	0.2	$18 \pm 5$	$15152 \pm 1837$	0.047	$14 \pm 5$	$0.011 \pm 0.004$
RXS J080358.9+433248	$2632 \pm 222$	$36 \pm 2$	8.9	7.3	$12 \pm 5$	$7791 \pm 1298$	0.007	$5 \pm 2$	$0.054 \pm 0.027$
1RXS J080534.6+543132	$3174 \pm 299$	$83 \pm 2$	-71.6	2.8	$14 \pm 5$	$7761 \pm 948$	-0.100	$8 \pm 3$	$0.083 \pm 0.032$
SDSS J081222.99+461529.1	$2807 \pm 283$	$37 \pm 1$	68.6	8.6	$11 \pm 5$	$10903 \pm 1795$	0.066	$10 \pm 4$	$0.028 \pm 0.013$
2MASSi J0816522+425829	$3768 \pm 186$	$25 \pm 1$	-0.3	4.1	$13 \pm 5$	$11461 \pm 1812$	-0.001	$9 \pm 4$	$0.021 \pm 0.010$
NGC 2639 U10	$6046 \pm 210$	$17 \pm 1$	46.8	1.7	$15 \pm 5$	$8537 \pm 1025$	0.454	$4 \pm 1$	$0.031 \pm 0.012$
SDSS J085632.39+504114.0	$2819 \pm 157$	$39 \pm 1$	39.3	11.2	$10 \pm 5$	$7759 \pm 1898$	0.039	$5 \pm 3$	$0.057 \pm 0.036$
SDSS J085828.69+342343.8	$3570 \pm 265$	$37 \pm 1$	-15.4	3.2	$14 \pm 5$	$9317 \pm 1257$	-0.031	$7 \pm 3$	$0.038 \pm 0.016$
SDSS J090455.00+511444.6	$3620 \pm 142$	$19 \pm 1$	45.0	1.9	$15 \pm 5$	$10570 \pm 1450$	0.094	$7 \pm 3$	$0.021 \pm 0.009$
RX J0906.0+4851	$2503 \pm 100$	$35 \pm 1$	197.8	26.1	$6 \pm 2$	$12852 \pm 2495$	0.135	$13 \pm 7$	$0.020 \pm 0.011$
RX J0908.7+4939	$2137 \pm 71$	$87 \pm 2$	83.1	25.3	$6 \pm 2$	$10378 \pm 1845$	0.035	$14 \pm 6$	$0.048 \pm 0.023$
1WGA J0931.9+5533	$5045 \pm 482$	$26 \pm 1$	-4.7	1.1	$16 \pm 5$	$21168 \pm 1902$	-0.026	$32 \pm 9$	$0.006 \pm 0.002$
SDSS J093653.84+533126.8	$4255 \pm 175$	$25 \pm 1$	-54.9	0.9	$16 \pm 5$	$22892 \pm 2378$	-0.185	$36 \pm 12$	$0.005 \pm 0.002$
FIRST J094610.9+322325	$1684 \pm 235$	$31 \pm 2$	-161.1	21.2	$7 \pm 2$	$7932 \pm 1005$	-0.033	$5 \pm 2$	$0.048 \pm 0.021$
KUV 09484+3557	$3244 \pm 289$	$22 \pm 1$	49.4	4.1	$13 \pm 5$	$8428 \pm 1161$	0.074	$5 \pm 2$	$0.037 \pm 0.017$
HS 1001+4840	$2962 \pm 230$	$24 \pm 3$	58.8	2.6	$14 \pm 5$	$13091 \pm 1433$	0.067	$12 \pm 4$	$0.016 \pm 0.008$
PC 1014+4717	$2583 \pm 103$	$25 \pm 1$	85.5	12.1	$10 \pm 5$	$8517 \pm 1896$	0.064	$5 \pm 3$	$0.038 \pm 0.023$
RX J1030.4+5516	$2246 \pm 157$	$40 \pm 4$	144.8	23.4	$6 \pm 2$	$11587 \pm 2125$	0.072	$12 \pm 6$	$0.026 \pm 0.016$
FBQS J103359.4+355509	$4543 \pm 237$	$13 \pm 1$	26.7	3.6	$14 \pm 5$	$8155 \pm 804$	0.110	$3 \pm 1$	$0.030 \pm 0.010$
SBS 1047+557B	$2253 \pm 97$	$43 \pm 2$	44.6	18.0	$8 \pm 2$	$9640 \pm 1305$	0.022	$8 \pm 3$	$0.039 \pm 0.016$
RX J1054.7+4831	$4428 \pm 274$	$49 \pm 2$	31.1	0.9	$16 \pm 5$	$11238 \pm 1494$	0.118	$12 \pm 5$	$0.030 \pm 0.013$
FBQS J105648.1+370450	$4538 \pm 272$	$20 \pm 2$	19.8	1.5	$15 \pm 5$	$9266 \pm 1158$	0.081	$5 \pm 2$	$0.028 \pm 0.014$

Object Name	$\text{FWHM}_{\text{H}\beta}$	$L_{5100}$	$h_3$	$h_4$	$i$	$v_{eq}$	$K_3$	$M_{BH}$	$L_{bol}/L_{Edd}$
FBQS J110704.5+320630	$8447 \pm 558$	$18 \pm 1$	-35.5	1.6	$15 \pm 5$	$20244 \pm 3385$	-0.938	$24 \pm 11$	$0.006 \pm 0.003$
FBQS J112956.5+364919	$3564 \pm 452$	$10 \pm 1$	67.7	4.0	$13 \pm 5$	$6458 \pm 719$	0.134	$2 \pm 1$	$0.041 \pm 0.020$
FBQS J115117.7+382221	$3696 \pm 242$	$188 \pm 4$	-17.8	5.2	$13 \pm 5$	$10746 \pm 1498$	-0.039	$22 \pm 8$	$0.065 \pm 0.026$
RX J1200.4+3334	$2864 \pm 173$	$9 \pm 1$	10.8	7.9	$11 \pm 5$	$8535 \pm 1589$	0.011	$3 \pm 1$	$0.023 \pm 0.014$
RX J1203.8+3711	$3725 \pm 1020$	$27 \pm 2$	79.2	4.2	$13 \pm 5$	$6487 \pm 1360$	0.179	$3 \pm 2$	$0.068 \pm 0.041$
1RXS J121759.9+303306	$3435 \pm 258$	$17 \pm 1$	33.4	2.3	$14 \pm 5$	$9501 \pm 1416$	0.059	$5 \pm 2$	$0.025 \pm 0.013$
RX J1218.3+3850	$4564 \pm 483$	$15 \pm 1$	-17.4	1.9	$15 \pm 5$	$10922 \pm 2094$	-0.073	$6 \pm 3$	$0.018 \pm 0.009$
FBQS J122035.1+385317	$1899 \pm 164$	$93 \pm 2$	-84.3	23.8	$6 \pm 2$	$8200 \pm 1549$	-0.025	$9 \pm 4$	$0.079 \pm 0.040$
FBQS J122424.2+401510	$4721 \pm 397$	$35 \pm 2$	15.0	1.8	$15 \pm 5$	$9616 \pm 958$	0.069	$8 \pm 2$	$0.035 \pm 0.013$
FBQS J122624.2+324429	$4535 \pm 533$	$7 \pm 1$	12.7	1.8	$15 \pm 5$	$9693 \pm 1214$	0.052	$3 \pm 1$	$0.016 \pm 0.007$
FBQS J125602.0+385230	$1978 \pm 147$	$31 \pm 3$	-78.5	22.3	$7 \pm 2$	$7495 \pm 1330$	-0.026	$4 \pm 2$	$0.054 \pm 0.032$
FBQS J132515.0+330556	$1921 \pm 102$	$27 \pm 1$	-29.5	18.8	$8 \pm 2$	$8592 \pm 1176$	-0.009	$5 \pm 2$	$0.039 \pm 0.017$
SDSS J144050.77+520446.0	$2483 \pm 134$	$20 \pm 1$	67.7	11.2	$10 \pm 5$	$9449 \pm 1890$	0.045	$6 \pm 3$	$0.028 \pm 0.016$
RX J1452.4+4522	$6594 \pm 156$	$88 \pm 4$	4.8	-0.2	$19 \pm 5$	$6990 \pm 893$	0.061	$6 \pm 2$	$0.105 \pm 0.044$
FBQS J145958.4+333701	$4389 \pm 209$	$89 \pm 20$	41.7	1.9	$15 \pm 5$	$7978 \pm 1051$	0.155	$8 \pm 4$	$0.081 \pm 0.056$
FIRST J154348.6+401324	$5227 \pm 391$	$29 \pm 2$	-53.0	3.9	$13 \pm 5$	$8394 \pm 848$	-0.332	$5 \pm 2$	$0.042 \pm 0.016$
SDSS J154833.03+442226.0	$3893 \pm 343$	$23 \pm 1$	-6.6	2.6	$14 \pm 5$	$11143 \pm 1427$	-0.017	$8 \pm 3$	$0.021 \pm 0.009$
FBQS J155147.4+330007	$2744 \pm 221$	$32 \pm 3$	12.0	6.4	$12 \pm 5$	$6663 \pm 1149$	0.011	$3 \pm 2$	$0.070 \pm 0.039$

Note –  $\text{FWHM}_{\text{H}\beta}$  and  $v_{eq}$  are in  $\text{km s}^{-1}$

$L_{5100}$  is given in  $10^{43} \text{ erg s}^{-1}$

$h_3$  and  $h_4$  are in units of  $10^{-7}$

$i$  is expressed in degrees

$M_{BH}$  is given in  $10^8 M_{\odot}$

Table 6.2: Extension of Measurements to the Thermodynamical Sample

Object Name	$h_3$	$h_4$	$i$	$v_{eq}$	$K_3$	$M_{BH}$	$L_{bol}/L_{Edd}$
LBQS 0010+0035	35.4	2.4	$14 \pm 5$	$3977 \pm 437$	0.112	$78 \pm 8$	$0.124 \pm 0.013$
2MASX J00133540-0951213	-91.1	602.6	$5 \pm 2$	$1509 \pm 339$	-0.006	$2 \pm 1$	$0.150 \pm 0.024$
2MASS J00372354+0008122	50.4	19.0	$7 \pm 2$	$5127 \pm 489$	0.039	$192 \pm 20$	$0.110 \pm 0.013$
2MASX J00423686-1049222	-35.2	38.2	$5 \pm 2$	$3636 \pm 501$	-0.018	$11 \pm 1$	$0.026 \pm 0.003$
SDSS J010712.03+140844.9	-76.7	40.3	$5 \pm 2$	$2981 \pm 434$	-0.036	$29 \pm 3$	$0.147 \pm 0.019$
2MASX J01100897-1008434	80.4	7.2	$12 \pm 5$	$3514 \pm 448$	0.078	$39 \pm 4$	$0.102 \pm 0.011$
2MASSI J0112549+000313	193.0	18.2	$8 \pm 2$	$3447 \pm 290$	0.092	$11 \pm 1$	$0.030 \pm 0.003$
SDSS J011703.58+000027.4	128.8	13.8	$9 \pm 2$	$2701 \pm 464$	0.096	$18 \pm 2$	$0.138 \pm 0.022$
QSO B0119-013	-12.6	2.7	$14 \pm 5$	$2950 \pm 248$	-0.019	$80 \pm 8$	$0.417 \pm 0.043$
2MASX J01352783-0044477	6.2	0.5	$17 \pm 5$	$4774 \pm 1089$	0.047	$290 \pm 30$	$0.221 \pm 0.026$
QSO B0137-010	210.6	8.1	$11 \pm 5$	$3359 \pm 285$	0.166	$24 \pm 2$	$0.074 \pm 0.009$
2MASX J01423843+0005145	897.3	249.1	$5 \pm 2$	$2346 \pm 246$	0.057	$3 \pm 1$	$0.041 \pm 0.007$
2MASX J01424828-1008402	-32.5	1.3	$15 \pm 5$	$4301 \pm 333$	-0.110	$36 \pm 4$	$0.042 \pm 0.005$
SDSS J015046.68+132359.9	2.0	3.2	$14 \pm 5$	$5240 \pm 782$	0.010	$36 \pm 4$	$0.019 \pm 0.002$
2MASX J01591007+0105148	48.8	6.6	$12 \pm 5$	$3796 \pm 436$	0.062	$39 \pm 4$	$0.073 \pm 0.009$
2MASS J02333539-0107446	132.6	6.8	$12 \pm 5$	$2899 \pm 536$	0.214	$19 \pm 2$	$0.105 \pm 0.013$
2MASS J02500703+0025251	75.7	67.9	$5 \pm 2$	$3302 \pm 237$	0.010	$7 \pm 1$	$0.023 \pm 0.003$
LBQS 0254+0101	-27.8	2.5	$14 \pm 5$	$3270 \pm 257$	-0.052	$12 \pm 1$	$0.042 \pm 0.006$
2MASX J03041778+0028274	100.0	2.7	$14 \pm 5$	$3446 \pm 324$	0.109	$57 \pm 6$	$0.160 \pm 0.019$
2MASX J03063958+0003426	192.4	34.8	$5 \pm 2$	$3553 \pm 609$	0.027	$10 \pm 1$	$0.024 \pm 0.004$
LBQS 0307-0101	41.1	4.8	$13 \pm 5$	$2978 \pm 271$	0.151	$29 \pm 3$	$0.148 \pm 0.018$
2MASS J03221390+0055134	209.0	61.8	$5 \pm 2$	$3404 \pm 431$	0.073	$13 \pm 1$	$0.038 \pm 0.006$

Object Name	$h_3$	$h_4$	$i$	$v_{eq}$	$K_3$	$M_{BH}$	$L_{bol}/L_{Edd}$
2MASS J03233765+00355555	99.9	11.7	$10 \pm 5$	$3516 \pm 344$	0.057	$97 \pm 9$	$0.250 \pm 0.026$
2MASX J03510759-0526370	54.8	8.6	$11 \pm 5$	$2761 \pm 383$	0.040	$19 \pm 2$	$0.128 \pm 0.016$
2MASX J04092918-0429021	43.4	6.0	$12 \pm 5$	$4912 \pm 400$	0.061	$68 \pm 7$	$0.046 \pm 0.005$
RX J0752.8+2617	52.1	51.1	$5 \pm 2$	$4272 \pm 487$	0.018	$20 \pm 2$	$0.024 \pm 0.003$
QSO B0752+393	-188.5	48.9	$5 \pm 2$	$3974 \pm 472$	-0.040	$19 \pm 2$	$0.031 \pm 0.003$
SDSS J083045.36+340532.1	-0.6	0.4	$18 \pm 5$	$3516 \pm 372$	-0.004	$25 \pm 3$	$0.066 \pm 0.009$
SDSS J083202.16+461425.8	14.0	15.3	$9 \pm 2$	$3999 \pm 365$	0.006	$20 \pm 2$	$0.030 \pm 0.004$
2MASX J08394965+4847014	5.7	-0.1	$19 \pm 5$	$2970 \pm 267$	0.042	$11 \pm 1$	$0.055 \pm 0.007$
SDSS J084025.51+033301.7	10.3	0.2	$18 \pm 5$	$3535 \pm 399$	0.034	$12 \pm 1$	$0.030 \pm 0.003$
2MASX J08550420+5252477	27.9	83.1	$5 \pm 2$	$3029 \pm 292$	0.006	$10 \pm 1$	$0.046 \pm 0.007$
2MASX J08573780+0528211	140.6	28.3	$5 \pm 2$	$4359 \pm 555$	0.081	$14 \pm 1$	$0.015 \pm 0.002$
2MASX J09043699+5536025	104.1	16.4	$8 \pm 2$	$3144 \pm 382$	0.070	$5 \pm 1$	$0.018 \pm 0.002$
SDSS J092554.25+533558.2	321.0	38.0	$5 \pm 2$	$3430 \pm 474$	0.050	$12 \pm 1$	$0.034 \pm 0.004$
QSO B0934+013	103.7	17.7	$8 \pm 2$	$4262 \pm 198$	0.052	$30 \pm 3$	$0.036 \pm 0.005$
LBQS 1008+0058	210.3	6.2	$12 \pm 5$	$2722 \pm 253$	0.203	$26 \pm 3$	$0.187 \pm 0.031$
2MASS J10131485-0052338	10.9	1.0	$15 \pm 5$	$6136 \pm 375$	0.152	$297 \pm 30$	$0.083 \pm 0.009$
1WGA J1016.7+4210	37.1	42.1	$5 \pm 2$	$4776 \pm 523$	0.010	$37 \pm 4$	$0.029 \pm 0.004$
Mrk 142	50.8	17.2	$8 \pm 2$	$3223 \pm 466$	0.014	$14 \pm 1$	$0.051 \pm 0.005$
2MASX J10425297+0414413	144.4	15.6	$8 \pm 2$	$3403 \pm 260$	0.057	$14 \pm 1$	$0.041 \pm 0.005$
2MASX J10570691-0041446	111.5	13.4	$9 \pm 2$	$4330 \pm 218$	0.065	$19 \pm 2$	$0.021 \pm 0.003$
2MASS J10593576-0005513	80.9	7.8	$11 \pm 5$	$4080 \pm 415$	0.068	$70 \pm 7$	$0.100 \pm 0.011$
2MASX J11050361+0745313	-11.3	1.7	$15 \pm 5$	$6018 \pm 492$	-0.072	$44 \pm 5$	$0.013 \pm 0.002$
MCG+10-16-111	101.4	7.6	$12 \pm 5$	$3255 \pm 267$	0.308	$23 \pm 3$	$0.082 \pm 0.011$
2MASX J11220940+0117199	-356.6	65.9	$5 \pm 2$	$3215 \pm 538$	-0.056	$10 \pm 1$	$0.037 \pm 0.004$

Object Name	$h_3$	$h_4$	$i$	$v_{eq}$	$K_3$	$M_{BH}$	$L_{bol}/L_{Edd}$
SDSS J112813.02+102308.3	-425.0	150.5	$5 \pm 2$	$2826 \pm 339$	-0.035	$12 \pm 1$	$0.072 \pm 0.009$
2MASX J11390898+5911547	162.9	22.9	$6 \pm 2$	$4058 \pm 461$	0.106	$28 \pm 3$	$0.042 \pm 0.004$
2MASX J11410569+0241173	361.7	37.5	$5 \pm 2$	$4071 \pm 800$	0.149	$13 \pm 1$	$0.019 \pm 0.002$
LBQS 1150+0010	85.7	4.7	$13 \pm 5$	$2662 \pm 231$	0.073	$27 \pm 3$	$0.216 \pm 0.032$
2MASS J11574174+0412506	161.8	114.1	$5 \pm 2$	$2973 \pm 366$	0.025	$15 \pm 2$	$0.075 \pm 0.012$
2MASS J11575874-0022208	-14.9	1.1	$15 \pm 5$	$4353 \pm 396$	-0.119	$98 \pm 10$	$0.109 \pm 0.014$
2MASX J12033294+0229346	5.0	7.4	$12 \pm 5$	$3210 \pm 321$	0.006	$27 \pm 3$	$0.101 \pm 0.011$
Mrk 50	129.4	6.9	$12 \pm 5$	$3901 \pm 268$	0.091	$19 \pm 2$	$0.032 \pm 0.004$
2MASX J12431998+0252562	-146.4	254.5	$5 \pm 2$	$2331 \pm 284$	-0.010	$5 \pm 1$	$0.066 \pm 0.012$
LBQS 1244+0238	14.1	4.5	$13 \pm 5$	$3839 \pm 353$	0.013	$43 \pm 4$	$0.079 \pm 0.008$
Mrk 236	78.7	2.4	$14 \pm 5$	$3388 \pm 422$	0.346	$15 \pm 2$	$0.046 \pm 0.005$
2MASX J13005216+5641056	46.1	24.9	$6 \pm 2$	$3688 \pm 496$	0.019	$22 \pm 2$	$0.048 \pm 0.006$
2MASS J13071325-0036018	148.9	13.6	$9 \pm 2$	$3781 \pm 248$	0.109	$44 \pm 4$	$0.085 \pm 0.009$
2MASS J13075656+0107097	-3.6	0.9	$16 \pm 5$	$5950 \pm 452$	-0.018	$210 \pm 21$	$0.066 \pm 0.008$
1WGA J1331.6+0131	302.9	158.1	$5 \pm 2$	$2526 \pm 305$	0.051	$9 \pm 1$	$0.090 \pm 0.014$
LBQS 1338-0038	117.6	14.5	$9 \pm 2$	$3095 \pm 225$	0.062	$24 \pm 2$	$0.102 \pm 0.013$
2MASX J13421004+5642106	78.3	7.7	$11 \pm 5$	$2854 \pm 334$	0.066	$8 \pm 1$	$0.047 \pm 0.006$
LBQS 1340-0038	-7.8	5.0	$13 \pm 5$	$3293 \pm 305$	-0.027	$23 \pm 2$	$0.078 \pm 0.008$
SDSS J134351.07+000434.8	150.7	34.0	$5 \pm 2$	$4193 \pm 557$	0.043	$38 \pm 4$	$0.049 \pm 0.006$
2MASX J13442643+4416194	254.5	96.1	$5 \pm 2$	$2471 \pm 272$	0.028	$8 \pm 1$	$0.082 \pm 0.010$
SDSS J134452.91+000520.2	4.6	1.1	$15 \pm 5$	$5455 \pm 330$	0.038	$138 \pm 14$	$0.062 \pm 0.008$
LBQS 1342-0000	113.2	17.7	$8 \pm 2$	$3962 \pm 278$	0.045	$38 \pm 4$	$0.061 \pm 0.007$
2MASS J13452470-0259396	17.7	3.4	$14 \pm 5$	$4458 \pm 407$	0.023	$18 \pm 2$	$0.018 \pm 0.002$
2MASX J13495283+0204456	113.7	7.8	$11 \pm 5$	$3110 \pm 131$	0.133	$7 \pm 1$	$0.028 \pm 0.004$

Object Name	$h_3$	$h_4$	$i$	$v_{eq}$	$K_3$	$M_{BH}$	$L_{bol}/L_{Edd}$
SDSS J135542.76+644045.0	238.2	67.5	$5 \pm 2$	$2444 \pm 355$	0.037	$8 \pm 1$	$0.088 \pm 0.013$
LBQS 1434+0020	48.1	19.7	$7 \pm 2$	$4456 \pm 287$	0.025	$75 \pm 7$	$0.075 \pm 0.008$
Mrk 1392	50.1	61.6	$5 \pm 2$	$3213 \pm 448$	0.006	$13 \pm 1$	$0.047 \pm 0.006$
2MASX J15102489+0058438	-45.2	3.7	$14 \pm 5$	$3319 \pm 427$	-0.234	$22 \pm 2$	$0.073 \pm 0.009$
2MASX J15192168+5908239	9.3	85.7	$5 \pm 2$	$3047 \pm 412$	0.001	$11 \pm 1$	$0.053 \pm 0.008$
2MASX J15195659+0016149	-10.6	2.9	$14 \pm 5$	$2630 \pm 288$	-0.039	$30 \pm 3$	$0.250 \pm 0.030$
QSO B1534+580	26.6	6.1	$12 \pm 5$	$2904 \pm 590$	0.066	$13 \pm 1$	$0.072 \pm 0.008$
SDSS J153830.78+444038.5	46.4	3.5	$14 \pm 5$	$3445 \pm 385$	0.069	$10 \pm 1$	$0.028 \pm 0.003$
2MASX J15541741+3238381	20.6	0.5	$17 \pm 5$	$4459 \pm 628$	0.135	$36 \pm 4$	$0.036 \pm 0.004$
MCG+06-36-003	56.5	3.7	$14 \pm 5$	$4324 \pm 427$	0.272	$25 \pm 2$	$0.028 \pm 0.003$
SDSS J161951.31+405847.2	-792.6	37.7	$5 \pm 2$	$2347 \pm 339$	-0.500	$7 \pm 1$	$0.088 \pm 0.011$
Mrk 699	-372.6	43.8	$5 \pm 2$	$3557 \pm 363$	-0.225	$22 \pm 2$	$0.055 \pm 0.007$
2E 1652.4+3930	85.5	17.7	$8 \pm 2$	$3986 \pm 489$	0.238	$13 \pm 1$	$0.021 \pm 0.003$
2MASS J16595894+6202181	14.3	1.8	$15 \pm 5$	$4703 \pm 297$	0.002	$140 \pm 14$	$0.113 \pm 0.013$
QSO B1717+5818	69.8	5.1	$13 \pm 5$	$3689 \pm 358$	0.109	$86 \pm 9$	$0.184 \pm 0.020$
2MASS J17190229+5937159	-16.0	0.6	$17 \pm 5$	$8625 \pm 404$	-0.086	$382 \pm 43$	$0.027 \pm 0.004$
2MASS J17202672+5540243	87.2	6.0	$12 \pm 5$	$4584 \pm 566$	0.159	$41 \pm 4$	$0.037 \pm 0.004$
SDSS J205822.14-065004.3	262.8	20.8	$7 \pm 2$	$3801 \pm 308$	0.100	$13 \pm 1$	$0.024 \pm 0.003$
2MASS J23493277-0036458	112.7	3.4	$14 \pm 5$	$4541 \pm 206$	0.102	$13 \pm 2$	$0.012 \pm 0.002$
SDSS J235156.12-010913.3	139.5	3.5	$14 \pm 5$	$3420 \pm 312$	0.175	$41 \pm 4$	$0.119 \pm 0.012$

Note –  $h_3$  and  $h_4$  are in units of  $10^{-7}$

$i$  is expressed in degrees

$M_{BH}$  is given in  $10^6 M_\odot$

# Chapter 7

## Conclusions

The main purpose of this work was to collect several flux and profile measurements of the broad emission line components in the Balmer series of a large number of AGN spectra and to use the results in the investigation of the BLR kinematical and thermodynamical properties. While we spent a great effort in performing as carefully as possible our direct measurements on the broad emission lines, the size of our sample and the limited spectral coverage forced us to calculate the continuum source properties by means of some simplified assumptions and empirical relations, which, in some cases, are still matter of debate.

Using the BP method, we explored the relation among the temperature parameter  $A$  and the broad line profiles. The values inferred in those objects where the technique achieved the best results would correspond to a temperature range running from  $8 \cdot 10^3$  K to  $21 \cdot 10^3$  K, with cold gas being usually associated with broad line emitters. However, a clear distinction among the intrinsic BLR thermodynamical properties and the effect of radiation traveling across an absorbing layer is not straightforward. In order to understand the physical processes which drive the relations among the gas ionization conditions and the BLR kinematics, we investigated the dynamical influence of the central engine. With the help of an advanced technique of line profile analysis, that places some constraints on the geometrical properties of the

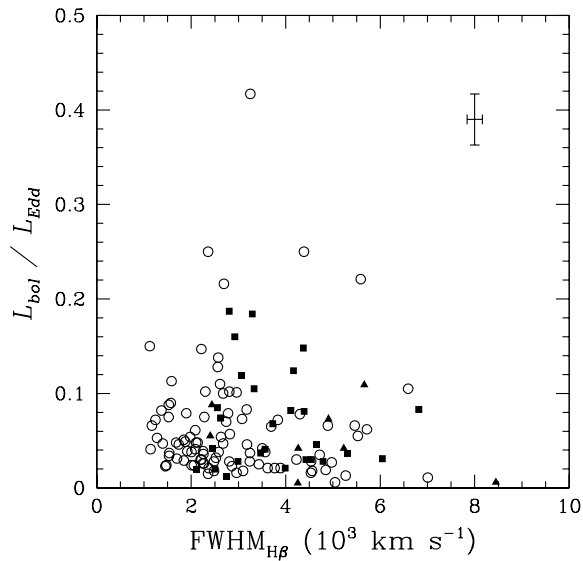


Figure 7.1: SMBH accretion rates vs.  $\text{FWHM}_{\text{H}\beta}$ , using the same symbology as in Fig. 6.6. The cross in the upper right corner of the diagram is the median uncertainty of measurements. We do not detect either very high accretion rates or systematic trends associated to the line profile widths. Our estimates do not appear to be dramatically affected by the presence of asymmetric profile components.

BLR, we applied a two-component kinematical model to the sources, therefore calculating the masses and accretion rates of their SMBH. As a result of this modification, we do not observe the strong dependence of the accretion rate on  $\text{FWHM}_{\text{H}\beta}$ , that commonly results from the SMBH mass estimates, if they are based only on the line profile widths. Instead, we are left with a much more complex situation, where, though a slight trend to measure lower accretion rates in broad line emitting sources is still present, it is not a general condition. The situation is summarized in Fig. 7.1, in which we marked the objects with high degrees of asymmetry, where the application of our models could be more problematic. Comparing their distribution with

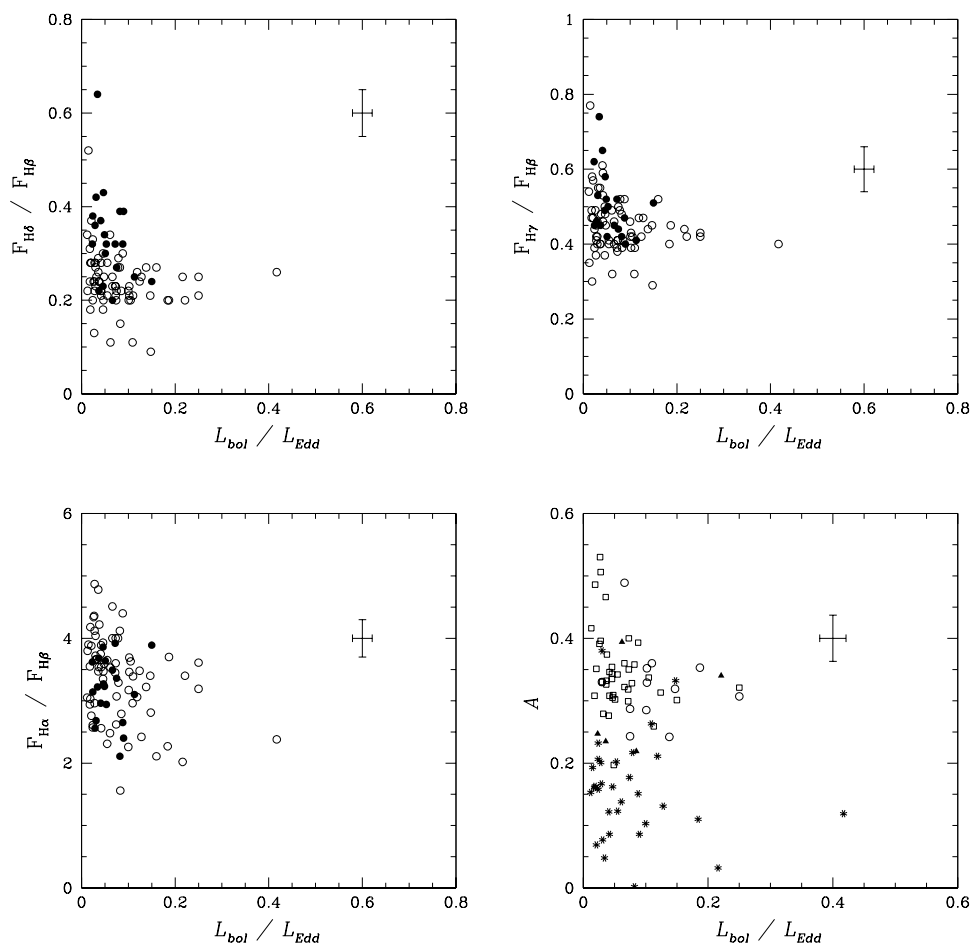


Figure 7.2: In the upper left, upper right, and lower left panels we plot the Balmer line flux ratios as a function of the inferred accretion rates (filled circles for NLS1 galaxies), while, in the lower right panel, the temperature parameter  $A$  is compared with the accretion rate, in objects with different BP classification (symbols as in Fig. 5.6).

the other sources, however, the existence of a strong asymmetric component in the broad line profiles does not appear to introduce systematic differences. In particular, we do not observe dramatic excesses in the accretion rate of our sources, whose estimates are well below the corresponding Eddington limits.

Comparing the Balmer line flux ratios and the corresponding temperature parameters with the accretion rates inferred in our sample, as it is shown in Fig. 7.2, we find that the gas ionization appears to be sensitive to the effects of accretion. Although there are quite large uncertainties and scatter among data, the ratio of the high order emission lines with respect to  $H\beta$  shows a weak decreasing trend, with, perhaps, a flattening towards the atomic values as soon as the accretion rate becomes larger. A more pronounced decrease is found in the case of  $H\alpha / H\beta$ . The combination of large or small ratios of both high order lines and  $H\alpha$ , with respect to  $H\beta$ , in the same objects indicates an irregular Balmer decrement, characteristic of sources which are far from PLTE and do not fit in the BP assumptions. As an average result, on the other hand, the Balmer decrement is more pronounced in low accretion rate sources, where we also detect most of the objects, whose line flux ratios give raise to fairly good BP. The temperature parameters of these objects suggest that gas heating is more effective at high accretion rates, though a difference in the gas column density along our line of sight may also be an important parameter, contributing to the observed scatter.

Taking into account the results of our analysis and the limits of the involved assumptions, we can summarize our conclusions as follows:

- the Balmer line flux ratios show a weak degree of correlation with the line profile width, in the sense that more pronounced Balmer decrements are observed in broader line emitting objects;
- the optical continuum luminosity of AGN correlates with the emission line intensities, supporting its role as an indicator of the ionizing continuum strength and giving raise to a global Baldwin Effect in [O III], which, instead, is not detected in the broad Balmer emission lines;
- the shape of the Balmer decrement, studied with the Boltzmann Plot technique, is related to the line profile widths and we observe that larger slopes and better straight line fits can be achieved in objects with broader lines, where a BLR component being described by the

assumptions of this method might be present;

- studying the broad emission line profiles as a whole it is possible to constrain some BLR structural properties, which we need to understand the relations among the gas kinematical and thermodynamical properties, and in particular we find that the line profile kurtosis is consistent with the presence of a flattened component in the BLR, with a typical inclination of  $i \leq 20^\circ$ , although the actual values of  $i$  may depend on the adopted model;
- some of the objects included in the sample have quoted measurements of linear polarization at radio frequencies, which averagely increase as the estimated BLR inclination approaches face-on, according to the model expectations;
- applying a geometrical correction to our SMBH mass and accretion rate estimates, we do not find a strong dependence of these parameters on FWHM, although objects with very broad emission lines typically have quite low Eddington ratios;
- the inferred accretion rates appear to influence the properties of the Balmer decrement, resulting in lower temperature parameters at higher Eddington ratios, which support a stronger heating of gas in these objects.

Although this analysis may represent an advance in the study of the relations among the central engine of AGN and the properties of the BLR, more questions should be answered, concerning how the kinematical components combine in the formation of the observed line profiles and whether they can influence the existence of PLTE in at least some fraction of the BLR gas. A precious contribution in this effort would probably result from the comparison of our techniques with some independent way to estimate the black hole accretion rate and the corresponding radiation field. Recent works suggested that this test could be possible, for example, with X-ray

observations. The ability to constrain the BLR geometrical factor and the ionizing radiation field, then, could be applied to study the relations among the BLR thermodynamical and kinematical properties in much better detail.

# Bibliography

- [1] Abazajian, K. et al. 2005, AJ, 129, 1755
- [2] Adelman-McCarthy, J. K. Agueros, M. A., Allam. S. S., et al. 2008, ApJS, 175, 297
- [3] Antonucci, R. R. J. & Miller, J. S. 1985, ApJ, 297, 621
- [4] Arav, N., Barlow, T. A., Laor, A., & Blandford, R. D. 1997, MNRAS, 288, 1015
- [5] Arav, N., Barlow, T. A., Laor, A., Sargent, W. L. W., & Blandford, R. 1998, MNRAS, 297, 990
- [6] Bahcall, J. N. & Kozlovsky, B. 1969a, ApJ, 155, 1077
- [7] Bahcall, J. N. & Kozlovsky, B. 1969b, ApJ, 158, 529
- [8] Bahcall, J. N., Kozlovsky, B. Z., & Salpeter, E. E. 1972, ApJ, 171, 467
- [9] Baldwin, J. A. 1977, ApJ, 214, 679
- [10] Baldwin, J. A., Wampler, E. J., & Gaskell, G. M. 1989, ApJ, 338, 630
- [11] Barton, E., Kannappan, S. J., Kurtz, M. J., & Geller, M. J. 2000, PASP, 112, 367
- [12] Barvainis, R. 1987, ApJ, 320, 537
- [13] Becker, P. 2008, ISO/IEC, N2798, 08-0308

- [14] Bentz, M. C., Peterson, B. M., Pogge, R. W., Vestergaard, M., & Onken, C. A. 2006, *ApJ*, 644, 133
- [15] Bian, W.-H. 2005, *CJAA*, 5, 21
- [16] Binette, L., Fosbury, R. A., & Parker, D. 1993, *PASP*, 105, 1150
- [17] Blandford, R. D. & McKee, C. F. 1982, *ApJ*, 255, 419
- [18] Boller, T., Brandt, W. N., & Fink, H. 1996, *A&A*, 305, 53
- [19] Bon, E., Popović, L. Č., Ilić, D., & Mediavilla, E. 2006, *NewAR*, 50, 716
- [20] Boroson, T. A. & Green, R. F. 1992, *ApJS*, 80, 109
- [21] Boroson, T. A. 2003, *ApJ*, 585, 647
- [22] Botte, V., Ciroi, S., Rafanelli, P., & Di Mille, F. 2004, *AJ*, 127, 3168
- [23] Burbidge, G. & Burbidge, M. 1967, *Quasi-Stellar Objects* (W. H. Freeman: San Francisco)
- [24] Capriotti, E., Foltz, C., & Byard, P. 1980, *ApJ*, 241, 903
- [25] Capriotti, E., Foltz, C., & Byard, P. 1981, *ApJ*, 245, 396
- [26] Cardelli, J. A., Clayton, G. C., & Mathis, J. S. 1989, *ApJ*, 345, 245
- [27] Carroll, T. J. 1985, *MNRAS*, 214, 321
- [28] Carroll, T. J. & Kwan, J. 1985, *ApJ*, 288, 73
- [29] Chen, K. & Halpern, J. P. 1989, *ApJ*, 344, 115
- [30] Chen, K., Halpern, J. P., & Filippenko, A. V. 1989, *ApJ*, 339, 742
- [31] Chen, H., Wang, J.-M., Ho, L. C., Chen, Y.-M., Bian, W.-H., & Xue, S.-J. 2008, *ApJL*, 683, 115
- [32] Clavel, J., Wamsteker, W., & Glass, I. 1989, *ApJ*, 337, 236

- [33] Collin, S., Boisson, C., Mouchet, M., Dumont, A.-M., Coupé, S., Pourquet, D., & Rokaki, E. 2002, *MNRAS*, 388, 771
- [34] Collin, S. & Kawaguchi, T. 2004, *MNRAS*, 426, 797
- [35] Collin, S., Kawaguchi, T., Peterson, B. M., & Vestergaard, M. 2006, *A&A*, 456, 75
- [36] Collin-Souffrin, S., Hameury, J. M., & Joly, M. 1988a, *A&A*, 205, 19
- [37] Collin-Souffrin, S., Dyson, J. E., McDowell, J. C., & Perry, J. J. 1988b, *MNRAS*, 232, 539
- [38] Collin-Souffrin, S. & Dumont, A. M. 1990, *MNRAS*, 229, 292
- [39] Condon, J. J., Cotton, W. D., Greisen, E. W., Yin, Q. F., Perley, R. A., Taylor, G. B., & Broderick, J. J. 1998, *AJ*, 115, 1693
- [40] Connolly, A. J., Szalay, A. S., Bershady, M. A., Kinney, A. L., & Calzetti, D. 1995, *AJ*, 110, 1071
- [41] Cota, S. A. & Ferland, G. J. 1988, *ApJ*, 326, 889
- [42] Davidson, K. 1972, *ApJ*, 171, 213
- [43] Decarli, R., Dotti, M., Fontana, M., Haardt, F. 2008a, *MNRAS*, 386, 15
- [44] Decarli, R., Labita, M., Treves, A., Falomo R. 2008b, *MNRAS*, in press
- [45] Dumont, A. M. & Collin-Souffrin, S. 1990, *A&A*, 229, 302
- [46] Edelson, R. A. & Krolik, J. H. 1989, *ApJ*, 333, 646
- [47] Edelson, R. A., Krolik, J. H., & Pike, G. F. 1990, *ApJ*, 359, 86
- [48] Elvis, M., Faasnacht, C., Wilson, A. S., & Briel, U. 1990, *ApJ*, 361, 459
- [49] Elvis, M., Wilkes, B. J., McDowell, J. C., Green, R. F., Bechtold, J., Willner, S. P., Oey, M. S., Polowski, E., & Cutri, R. 1994, *ApJS*, 95, 1

- [50] Emmering, R. T., Blandford, R. D., & Shlosman, I. 1992, *ApJ*, 385, 460
- [51] Fabian, A. C., Guilbert, P. W., Arnud, K. Shafer, R. A., Tennant, A. F., & Ward, M. J. 1986, *MNRAS*, 218, 457
- [52] Fath, E. A. 1908, *LicOB*, 5, 71
- [53] Ferland, G. J. & Netzer, H. 1979, *ApJ*, 229, 274
- [54] Ferland, G. J. & Persson, S. E. 1989, *ApJ*, 347, 656
- [55] Ferland, G. J., Peterson, B. M., Horne, K., Welsh, W. F., & Nahar, S. N. 1992, *ApJ*, 387, 95
- [56] Ferrarese, L. & Merritt, D. 2000, *ApJL*, 539, 9
- [57] Ferrarese, L., Côté, P., Dalla Bontà, E., Peng, E. W., Merritt, D., Jordán, A., Blakeslee, J. P., Hasegan, M., Mei, S., Piatek, S., Tonry, J. L., & West, M. J. 2006, *ApJ*, 644, 21
- [58] Frank, J., King, A., & Raine, D. J. 2002, "Accretion Power in Astrophysics" (3<sup>rd</sup> ed.; Cambridge: Cambridge University Press)
- [59] Garrington, S. T., Leahy, J. P., Conway, R. G., & Laing, R. A. 1988, *Nature*, 331, 147
- [60] Gaskell, C. M. & Sparke, L. S. 1986, *ApJ*, 305, 175
- [61] Gaskell, M. & Peterson, B. M. 1987, *ApJS*, 65, 1
- [62] Gilbert, K. M. & Peterson, B. M. 2003, *ApJ*, 587, 123
- [63] Goad, M. R., Korista, K. T., & Knigge, C. 2004, *MNRAS*, 325, 277
- [64] Griem, H. R. 1997, *Principles of Plasma Spectroscopy* (Cambridge: Cambridge University Press)

- [65] Gunn, J. E., Carr, M., Rockosi, C., Sekiguchi, M., Berry, K., Elms, B., de Haas, E., Ivezić, Ž., Knapp, G., Lupton, R., Pauls, G., Simcoe, R., Hirsch, R., Sanford, D., Wang, S., York, D., Harris, F., Annis, J., Bartozek, L., Boroski, W., Bakken, J., Haldeman, M., Kent, S., Holm, S., Holmgren, D., Petravick, D., Prosapio, A., Rechenmacher, R., Doi, M., Fukugita, M., Shimasaku, K., Okada, N., Hull, C., Siegmund, W., Mannery, E., Blouke, M., Heidtman, D., Schneider, D., Lucinio, R., & Brinkman, J. 1998, *AJ*, 116, 3040
- [66] Haardt, F. & Maraschi, L. 1993, *ApJ*, 413, 507
- [67] Hicks, E. K. S. & Malkan, M. A. 2008, *ApJS*, 174, 31
- [68] Ilić, D., Popović, L. Č., Bon, E., Mediavilla, E. G., & Chavushyan, V. H. 2006, *MNRAS*, 371, 1610
- [69] Jackson, N, Penston, M. V., & Pérez, E. 1991, *MNRAS*, 249, 577
- [70] Jarvis, M. J. & McLure, R. J. 2006, *MNRAS*, 369, 182
- [71] Joly, M. 1987, *A&A*, 184, 33
- [72] Kallman, T. & Mushotzky, R. 1985, *ApJ*, 292, 49
- [73] Kaspi, S. & Netzer, H. 1999, in *ASP Conference Series 162, Quasars and Cosmology*, ed. Gary Ferland and Jack Baldwin (San Francisco: ASP), 223
- [74] Kaspi, S., Smith, P. S., Netzer, H., Maoz, D., Jannuzi, B. T., & Giveon, U. 2000, *ApJ*, 533, 631
- [75] Kaspi, S., Maoz, D., Netzer, H., Peterson, B. M., Vestergaard, M., & Jannuzi, B. T. 2005, *ApJ*, 629, 61
- [76] Kaspi, S., Brandt, W. N., Maoz, D., Netzer, H., Schneider, D. P., Shemmer, O. 2007, *ApJ*, 659, 997
- [77] Kazanas, D. 1989, *ApJ*, 347, 74

- [78] Kellerman, K. I., Sramek, R., Schmidt, M., Shaffer, D. B., & Green, R. 1989, *AJ*, 98, 1195
- [79] Kellermann, K. I., Vermeulen, R. C., Zensus, J. A., Cohen, M. H. 1998, *AJ*, 115, 1295
- [80] Kelly, B. C. & Bechtold, J. 2007, *ApJS*, 168, 1
- [81] Kelly, B. C., Bechtold, J., Trump, J. R., Vestergaard, M., & Siemiginowska, A. 2008, *ApJ*, in press
- [82] Kinney, A. L., Rivolo, A. R., & Koratkar, A. P. 1990, *ApJ*, 357, 338
- [83] Kinney, A. L. 1994, in *ASP Conf. Ser. 54, The First Stromlo Symposium : The Physics of Active Galaxies*, ed. B. V. Bicknell, M. A. Dopita, & P. J. Quinn, 61
- [84] Kollatschny, W. & Fricke, K. J. 1985, *A&AL*, 146, 11
- [85] Kollatschny, W. & Dietrich, M. 1996, *A&A*, 314, 43
- [86] Kollatschny, W. & Dietrich, M. 1997, *A&A*, 323, 5
- [87] Kollatschny, W., Bischoff, K., & Dietrich, M. 2000, *A&A*, 361, 901
- [88] Kollatschny, W. & Bischoff, K. 2002, *A&AL*, 386, 19
- [89] Kollatschny, W. 2003, *A&A*, 407, 461
- [90] Komossa, S. 2008, *The Nuclear Region, Host Galaxy and Environment of Active Galaxies*, ed. Benítez E., Cruz-González I., & Krongold Y., *RevMexAA (SC)* Vol. 32, 86
- [91] Kong, M.-Z., Wu, X.-B., Wang, R., Liu, F. K., & Han, J. L. 2006, *A&A*, 456, 473
- [92] Koniević, N. 1999, *Phys. Rep.*, 316, 339
- [93] Koratkar, A. P. & Gaskell, C. M. 1991, *ApJS*, 75 719

- [94] Korista, K. T. & Goad, M. R. 2004, *ApJ*, 606, 749
- [95] Korista, K. T. & Goad, M. R. 2005, *ApJ*, 627, 577, an erratum
- [96] Krolik, J. H., McKee, C. F., & Tarter, C. B. 1981, 249, 422
- [97] Krolik, J. H. 1988, *ApJ*, 325, 148
- [98] Krolik, J. H. & Kallman, T. A. 1988, *ApJ*, 324, 714
- [99] Krolik, J. H. 1999, *Active Galactic Nuclei: from the central black hole to the galactic environment* (Princeton: Princeton University Press)
- [100] Kuehn, C. A., Baldwin, J. A., Peterson, B. M., & Korista, K. T. 2008, *ApJ*, 673, 69
- [101] Kuraszkiewicz, J., Wilkes, B. J., Brandt, W. N., & Vestergaard, M. 2000, *ApJ*, 542, 631
- [102] Kwan, J. & Carroll, T. J. 1982, *ApJ*, 261, 25
- [103] Labita, M., Treves, A., Falomo, R., & Uslenghi, M. 2006, *MNRAS*, 373, 551
- [104] Laing, R. A. 1988, *Nature*, 331, 149
- [105] La Mura, G., Popović, L. Č., Ciroi, S., Rafanelli, P., & Ilić, D. 2007, *ApJ*, 671, 104
- [106] Laor, A., Barth, A. J., Ho, L. C., & Filippenko, A. V. 2006, *ApJ*, 636, 83
- [107] Laor, A. 2007, in *ASP Conf. Ser. 373, The Central Engine of Active Galactic Nuclei*, ed. L. C. Ho & J.-W. Wang (San Francisco: ASP), 384
- [108] Lepp, S., McRay, R., Shull, J. M., Woods, D., T., & Kallman, T. 1985, *ApJ*, 288, 58
- [109] Lynden-Bell, D. 1969, *Nature*, 223, 690

- [110] Lynds, C. R., Stockton, A. N., & Livingston, W. C. 1965, *ApJ*, 142, 1667
- [111] MacAlpine, G. 1972, *ApJ*, 175, 11
- [112] Marconi, A., Axon, D. J., Maiolino, R., Nagao, T., Pastorini, G., Pietrini, P., Robinson, A., Torricelli, G. 2008, *ApJ*, 678, 693
- [113] Martin, P. G. & Ferland, G. J. 1980, *ApJL*, 235, 125
- [114] Maoz, D. & Netzer, H. 1989, *MNRAS*, 236, 21
- [115] Maoz, D., Netzer, H., Mazeh, T., Beck, S., Almoznino, E., Leibowitz, E., Brosch, N., Mendelson, H., & Laor, A. 1991, *ApJ*, 367, 493
- [116] Marziani, P., Sulentic, J. W., Dultzin-Hacyan, D., Calvani, M., & Moles, M. 1996, *ApJS*, 104, 37
- [117] Marziani, P., Sulentic, J. W., Zwitter, T., Dultzin-Hacyan, D., & Calvani, M. 2001, *ApJ*, 558, 553
- [118] Marziani, P., Zamanov, R. K., Sulentic, J. W., & Calvani, M. 2003, *MNRAS*, 345, 1133
- [119] Marziani, P., Dultzin-Hacyan, D., Sulentic, J. W. 2006, *New Development in Black Hole Research* (New York: Nova Science Publishers)
- [120] Mathews, W. G & Ferland, G. J. 1987, *ApJ*, 323, 456
- [121] Mathur, S., Kuraszekiewicz, J., & Czerny, B. 2001, *NewA*, 6, 321
- [122] Matsuoka, Y., Kawara, K., & Oyabu, S. 2008, *ApJ*, 673, 62
- [123] McGill, K. L., Woo, J.-H., Treu, T., Malkan, M. A. 2008, *ApJ*, 673, 703
- [124] McLure, R. J. & Dunlop, J. S. 2002, *MNRAS*, 331, 795
- [125] McLure, R. J. & Jarvis, M. J. 2002, *MNRAS*, 337, 109

- [126] Melnikov, A. V. & Shevchenko, I. I. 2008, *MNRAS*, 389, 478
- [127] Miller, J. S., Goodrich, R. W., & Mathews, W. G. 1991, *ApJ*, 378, 47
- [128] Mullaney, J. R. & Ward, M. J. 2008, *MNRAS*, 385, 53
- [129] Murdoch, H. S. 1983, *MNRAS*, 202, 987
- [130] Murray, N. & Chiang, J. 1997, *ApJ*, 474, 91
- [131] Mushotzky, R. F. & Ferland, G. J. 1984, *ApJ*, 278, 558
- [132] Netzer, H. & Wills, B.J. 1983, *ApJ*, 275, 445
- [133] Netzer, H. 1985, *MNRAS*, 216, 63
- [134] Netzer, H. 1990, "AGN Emission Lines", published in "Active Galactic Nuclei", eds. R. D. Blandford, H. Netzer, and L. Woltjer
- [135] Netzer, H., Laor, A., & Gondhalekar, P. M. 1992, *MNRAS*, 254, 15
- [136] Nicastro, F. 2000, *ApJL*, 530, L65
- [137] Nikolajuk, M., Czerny, B., & Ziolkowsky, J. 2005 in *AIP Conf. Proc.* 801, *Astrophysical Sources of High Energy Particles and Radiation*, ed. T. Bulik, B. Rudak, & G. Madejski (Melville: AIP), 220
- [138] Onken, A. C., Ferrarese, L., Merritt, D., Peterson, B. M., Pogge, R. W., Vestergaard, M., & Wandel, A. 2004, *ApJ*, 615, 645
- [139] Osmer, P. S. & Smith, M. G. 1980, *ApJS*, 42, 333
- [140] Osmer, P. S. & Shields, J. C. 1999, *ASPCS*, 162, 235
- [141] Osterbrock, D. E. 1981, *ApJ*, 249, 462
- [142] Osterbrock, D. E. & Pogge, R. W. 1985, *ApJ*, 297, 166
- [143] Osterbrock, D. E. 1989, "Astrophysics of Gaseous Nebulae and Active Galactic Nuclei" (1<sup>st</sup> ed.; Sausalito: University Science Books)

- [144] Penston, M. V. 1987, MNRAS, 229, 1
- [145] Penston, M. V. 1988, MNRAS, 233, 601
- [146] Perry, J. J. & Dyson, J. E. 1985, MNRAS, 213, 665
- [147] Peterson B.M. 1987, ApJ, 312, 79
- [148] Peterson, B. M. 1995, "An Introduction to Active Galactic Nuclei"  
(Cambridge: Cambridge University Press)
- [149] Peterson, B. M. & Wandel, A. 1999, ApJ, 521, 95
- [150] Peterson, B. M. & Wandel, A. 2000, ApJL, 540, 13
- [151] Peterson, B. M. 2003, in ASP Conf. Ser. 290, Active Galactic Nuclei:  
From Central Engine to Host Galaxy, ed. Collin, S. and Combes, F. and  
Shlosman, I., 43
- [152] Peterson, B. M., Ferrarese, L., Gilbert, K. M., Kaspi, S., Malkan, M.  
A., Maoz, D., Merrit, D., Netzer, H., Onken, C. A., Pogge, R. W., Vester-  
gaard, M., & Wandel, A. 2004, ApJ, 613, 682
- [153] Popović, L. Č. 2003, ApJ, 599, 140
- [154] Popović, L. Č. 2006, ApJ, 650, 1217 (an Erratum)
- [155] Popović, L. Č., Mediavilla, E., Kubičela, A., & Jovanović, P. 2002,  
A&A, 390, 473
- [156] Popović, L. Č., Mediavilla, E., Bon, E., Stanić, N., & Kubičela, A.  
2003, ApJ, 599, 185
- [157] Popović, L. Č., Mediavilla, E., Bon, E., & Ilić, D. 2004, A&A, 423, 909
- [158] Popović, L. Č., Bon, E., Gavrilović, N. 2008, The Nuclear Region,  
Host Galaxy and Environment of Active Galaxies, ed. Benítez E., Cruz-  
González I., & Krongold Y., RevMexAA (SC) Vol. 32, 99

- [159] Rafanelli, P. 1985, *A&A*, 146, 17
- [160] Rees, M. 1987, *MNRAS*, 228, 47
- [161] Rudy, R. J. & Schmidt, G. D. 1988, *ApJ*, 331, 325
- [162] Sandage, A. 1965, *ApJ*, 141, 1560
- [163] Sanders, D. B., Phinney, E. S., Neugebauer, G., Soifer, B. T., & Matthews, K. 1989, *ApJ*, 347, 29
- [164] Schlegel, D. J., Finkbeiner, D. P., & Davis, M. 1998, *ApJ*, 500, 525
- [165] Scoville, N. & Norman, C. 1988, *ApJ*, 332, 163
- [166] Seyfert, C. 1943, *ApJ*, 97, 28
- [167] Shakura, N. I. & Sunyaev, R. A. 1973, *A&A*, 24, 337
- [168] Shemmer, O., Brandt, W. N., Netzer, H., Maiolino, R., Kaspi, S. 2006, *ApJ*, 646, 29
- [169] Shields, G. A. 1977, *ApL*, 18, 119
- [170] Shields, G. A. 1978, *Nature*, 272, 706
- [171] Shlosman, I., Vitello, P. A., & Shaviv, G. 1985, *ApJ*, 294, 96
- [172] Slipher, V. M. 1917, *LowOB*, 3, 59
- [173] Sluse, D., Claeskens, J.-F., Hutsemékers, D., Surdej, J. 2008, *The Nuclear Region, Host Galaxy and Environment of Active Galaxies*, ed. Benítez E., Cruz-González I., & Krongold Y., *RevMexAA (SC)* Vol. 32, 83
- [174] Smith, M. D. & Raine, D. J. 1985, *MNRAS*, 212, 425
- [175] Smith, J. E., Young, S., Robinson, A., Corbett, E. A., Giannuzzo, M. E., Axon, D. J., & Hough, J. H. 2002, *MNRAS*, 335, 773

- [176] Snedden, S. & Gaskell, C. 2004, in ASP Conf. Ser. 311, AGN Physics with the Sloan Digital Sky Survey, ed. G. T. Richards & P. B. Hall, 197
- [177] Statler, T. S. 1995, *AJ*, 109, 1371
- [178] Steidel, C. C., Sargent, W. L. W. 1991, *ApJ*, 382, 433
- [179] Stirpe G.M., De Bruyn A.G., & van Groningen E. 1988, *A&A*, 200, 9
- [180] Sulentic, J. W., Marziani, P., Dultzin-Hacyan, D., Calvani, M., & Moles, M. 1995, *ApJ*, 445, 86
- [181] Sulentic, J. W., Marziani, P., & Dultzin-Hacyan, D. 2000a, *ARA&A*, 38, 521
- [182] Sulentic, J. W., Zwitter, T., Marziani, P., & Dultzin-Hacyan, D. 2000b, *ApJL*, 536, 5
- [183] Sulentic, J. W., Zamfir, F., Marziani, P., Bachev, R., Calvani, M., & Dultzin-Hacyan, D. 2003, *ApJL*, 597, 17
- [184] Sulentic, J. W., Repetto, P., Stirpe, G. M., Marziani, P., Dultzin-Hacyan, D., & Calvani, M. 2006, *A&A*, 456, 929
- [185] Sulentic, J. W., Bachev, R., Marziani, P., Negrete, C. A., & Dultzin, D. 2007, *ApJ*, 666, 757
- [186] Tonry, J. & Davis, M. 1979, *AJ*, 84, 1511
- [187] Vanden Berk, D. E., Shen, J., Yip, C. W., Schneider, D. P., Connolly, A. J., Burton, R. E., Jester, S., Hall, P. B., Szalay, A. S., & Brinkmann, J. 2006, *AJ*, 131, 84
- [188] Van Der Marel, R. & Franx, M. 1993, *ApJ*, 407, 525
- [189] Véron-Cetty, M.-P., Joly, M., & Véron, P. 2004, *A&A*, 417, 515
- [190] Véron-Cetty, M.-P. & Véron, P. 2006, *A&A*, 455, 773

- [191] Véron-Cetty, M.-P., Joly, M., Véron, P., Boroson, T., Lipari, S., & Ogle, P. 2006, *A&A*, 451, 851
- [192] Vestergaard, M., Wilkes, B. J., & Barthel, P. D. 2000, *ApJL*, 538, 103
- [193] Vestergaard, M. 2002, *ApJ*, 571, 733
- [194] Vestergaard, M. 2004, *ApJ*, 601, 676
- [195] Vestergaard, M. & Peterson, B. M. 2006, *ApJ*, 641, 689
- [196] Voit, G. M. & Shull, J. M. 1988, *ApJ*, 331, 197
- [197] Wampler, E. J., Gaskell, C. M., Burk, W. L., & Baldwin, J. A. 1984, *ApJ*, 276, 403
- [198] Wamsteker, W. & Collina, L., 1986, *ApJ*, 311, 617
- [199] Wandel, A. 1999, *ApJ*, 519, 39
- [200] Wandel, A., Peterson, B. M., & Malkan, M. A. 1999, *ApJ*, 526, 579
- [201] Wills, B. J., Netzer, H., & Wills, D. 1985, *ApJ*, 288, 94
- [202] Wilkes, B. J. & Elvis, M. 1987, *ApJ*, 323, 243
- [203] Wills, B. J. & Browne, I. W. 1986, *ApJ*, 302, 56
- [204] Wilson, A. S., Elvis, M., Lawrence, A., & Bland-Hawthorn, J. 1992, *ApJL*, 391, 75
- [205] Wilson, A. S. & Colbert, E. J. M. 1995, *ApJ*, 438, 62
- [206] Woo, J.-H. & Urry, C. M. 2002, *ApJ*, 579, 530
- [207] Wu, X.-B., Wang, R., Kong, M. Z., Liu, F. K., & Han, J. L. 2004, *A&A*, 424, 793
- [208] Yee, H. K. C. 1980, *ApJ*, 241, 849

- [209] Yip, C. W., Connolly, A. J., Szalay, A. S., Budavári, T., SubbaRao, M., Frieman, J. A., Nichol, R. C., Hopkins, A. M., York, D. G., Okamura, S., Brinkmann, J., Csabai, I., Thakar, A. R., Fukugita, M., & Ivezić Ž. 2004a, AJ, 128, 585
- [210] Yip, C. W., Connolly, A. J., Vanden Berk, D. E., Ma, Z., Frieman, J. A., SubbaRao, M., Szalay, A. S., , Richards, G. T., Hall, P. B., Schneider, D. P., Hopkins, A. M., Trump, J., & Brinkmann, J. 2004b, AJ, 128, 2603
- [211] York, D. G. et al. (The SDSS Collaboration) 2000, AJ, 120, 1579
- [212] Zheng W., P. E., Grandi S.A., & Penston M. V. 1995, AJ, 109, 2355